On the Accuracy of Fiber Tractography

by

Sebastiano Barbieri

A Thesis submitted in partial fulfillment
of the requirements for the degree of

Doctor of Philosophy
in Computer Science

Approved Dissertation Committee

Prof. Dr. Horst K. Hahn

Prof. Dr. Andreas Nüchter

Dr. Anna Vilanova i Bartrolí

Date of Defense: September 24th, 2012

School of Engineering and Science

Statutory Declaration

I, Sebastiano Barbieri, hereby declare that I have written this PhD thesis independently, unless where clearly stated otherwise. I have used only the sources, the data and the support that I have clearly mentioned. This PhD thesis has not been submitted for conferral of degree elsewhere.

Saarbrücken, November 18, 2012

To my grandfather Heinz W. Reuschel,
who inspired my interest in mathematics and computer science.

Acknowledgements

I would like to thank all my colleagues in Bremen for making Fraunhofer MEVIS such an enjoyable working environment during the years I worked on this thesis. Especially Dr. Jan Klein, with his knowledgeable feedback and his eye for detail, has contributed significantly to its success, while David Black made sure that not too many English mistakes found their way into my publications. My gratitude goes to the reviewers of this thesis, Prof. Dr. Horst Hahn, Prof. Dr. Andreas Nüchter, and Dr. Anna Vilanova i Bartrolí, for their help and the many inspiring discussions. I would like to acknowledge Prof. Dr. Terwey, Prof. Dr. Hildebrandt, and Florian Weiler for providing the datasets used in Figures 3.9 and 3.14. This project was made possible thanks to funding by the German Research Society (DFG PE199/21-1 & DFG NI568/3-1).

Finally, I would like to thank my parents, Giuseppe and Richarda, and Kristina for their love and unconditional support.

Abstract

Invasive neurosurgical interventions bear the risk of damaging indispensable fiber pathways. Current fiber reconstruction techniques based on diffusion tensor imaging (DTI) do not determine the spatial extent of a fiber bundle in an accurate and reliable manner, due to errors and imprecisions in both the imaging and the algorithmic pipeline. In this thesis, we start by quantifying the errors of current fiber tracking algorithms by means of novel software phantoms which provide a realistic model of neural fiber bundles. This knowledge is used to locally analyze the quality of a patient's diffusion tensor dataset and to construct individual confidence hulls around the tracked fibers. In the following chapter, these ideas are developed further and we suggest an accurate approach to the segmentation of a patient's diffusion tensor image which combines connectivity and tensor clustering information. We then focus our attention on the sensitivity of streamline tractography to user-defined regions of interest. In order to reduce this sensitivity, we demonstrate the feasibility of mapping a fiber bundle from a fiber atlas onto the DTI dataset of a patient. In the last chapter of this thesis, we consider several alternatives to visualize fiber-tracking related uncertainties by means of color-coded streamlines and confidence hulls.

Contents

Contents **v**

1 Introduction **1**

1.1 Diffusion Magnetic Resonance 3

1.2 Diffusion Tensor Imaging 8

1.3 Fiber Tracking 13

1.4 Outline of the Thesis 17

2 Segmentation of Fiber Tracts Based on an Accuracy Analysis on Diffusion Tensor Software Phantoms **20**

2.1 Abstract 20

2.2 Introduction 21

2.3 Generating and Analyzing Fiber-Tracking Error on a Torus-Shaped DTI Phantom 23

2.3.1 DTI Model Framework 23

2.3.1.1 The Torus-Shaped Phantom 25

2.3.2 Measuring Fiber-Tracking Error 25

2.3.2.1 The Fiber-Tracking Algorithm 26

2.3.2.2 The Safety Radius 26

2.3.3 Experimental Results Obtained by Means of the Torus-Shaped Phantom 27

2.4 Generating and Analyzing Fiber-Tracking Error on a Realistic DTI Phantom of Neural Fiber Bundles 30

2.4.1 Generating the BrainWeb-Based Phantom 31

2.4.2 Modeling White Matter Pathways 33

2.4.2.1 Minimizing the Point to Spline Distance 35
2.4.2.2 Mapping the Distance Function to Alternative Kernels 36
2.4.3 Experimental Results Obtained by Means of the BrainWeb-Based Phantom 37
2.5 Estimating the Extent of Fiber Bundles 41
2.5.1 Review of Computing the Covariance Matrix of the Main Diffusion Direction 41
2.5.2 A New Plausibility Measure for a Voxel to Be Part of the Tracked Bundle 43
2.5.3 Experimental Results 44
2.6 Discussion 46
2.7 Conclusions 50

3 DTI Segmentation via the Combined Analysis of Connectivity Maps and Tensor Distances 52
3.1 Abstract 52
3.2 Introduction 53
3.2.1 Related Work 54
3.2.2 Contributions 56
3.3 Methods 57
3.3.1 Algorithm 57
3.3.1.1 Notation and Computation of the Connectivity Map 58
3.3.1.2 The Connectivity Factor 58
3.3.1.3 The Clustering Factor 59
3.3.1.4 Updating the Membership Function and Regularization 60
3.3.1.5 Partial-Volume Correction 61
3.3.1.6 Overview of the Algorithm 62
3.3.2 Software Phantom 64
3.4 Results 65
3.4.1 Accuracy Analysis 66
3.4.2 Reproducibility Analysis 68

3.4.3 Efficiency Analysis 70
3.5 Discussion and Conclusion 72

4 Atlas-Based Fiber Reconstruction from Diffusion Tensor MRI Data 79
4.1 Abstract 79
4.2 Introduction 80
4.3 Methods 81
4.3.1 Fiber Representation 81
4.3.2 Fiber Atlas 82
4.3.3 Energy Functional 82
4.3.4 Simulated Annealing 83
4.3.4.1 Candidate Generation 84
4.3.4.2 Cooling Schedule and Acceptance Probabilities . 85
4.3.5 Optional Transformation Restrictions 87
4.4 Results 89
4.5 Discussion 90

5 Simulating Tumor Growth and Visualizing Fiber Tracking Uncertainty 98
5.1 Abstract 98
5.2 Introduction 99
5.2.1 Related Work 100
5.2.2 Contributions 101
5.3 Methods 101
5.3.1 Tumor Growth Model 102
5.3.2 PDE Coupling and Discretization 103
5.3.3 Summary of the Tumor Growth Algorithm 106
5.3.4 Uncertainty Visualization by Color-Coding Streamlines . . 107
5.3.5 Confidence Hulls 108
5.4 Results 111
5.5 Discussion and Conclusions 114

6 Conclusions **122**

6.1 Summary 122

6.2 Perspective 126

Publications by Sebastiano Barbieri **129**

References **132**

Chapter 1

Introduction

Let us begin with a brief overview on diffusion magnetic resonance, diffusion tensor imaging, and fiber tracking, followed by an outline of the topics discussed in this thesis. Diffusion is a mass transfer process driven by a concentration gradient. It results in molecular mixing without requiring bulk motion. The process is illustrated in Fig. 1.1 where a drop of ink is introduced into two flasks filled with water at different temperatures. The ink spreads over time with an approximately spherically symmetric profile. It is noticeable how a higher temperature of the medium corresponds to a faster diffusion process.

The diffusion process is described by Fick's first law (Fick [1855a,b]), which states that the diffusion flux vector J points from regions of high particle concentration to regions of low particle concentration:

$$J = -D \nabla C \tag{1.1}$$

where C indicates the particle concentration and D is a proportionality constant called the "diffusion coefficient". D is determined by the size of the diffusing molecules and by the viscosity and temperature (see Fig. 1.1) of the medium.

On the molecular level the diffusion process arises due to the Brownian motion of particles which persists also after a state of equilibrium has been reached and the net diffusion flux has vanished. Within biological tissue, molecular motion is restricted by microstructural factors as for example cell membranes and cytoskeleton (Tanner and Stejskal [1968]). At the voxel length scale (a few millimeters)

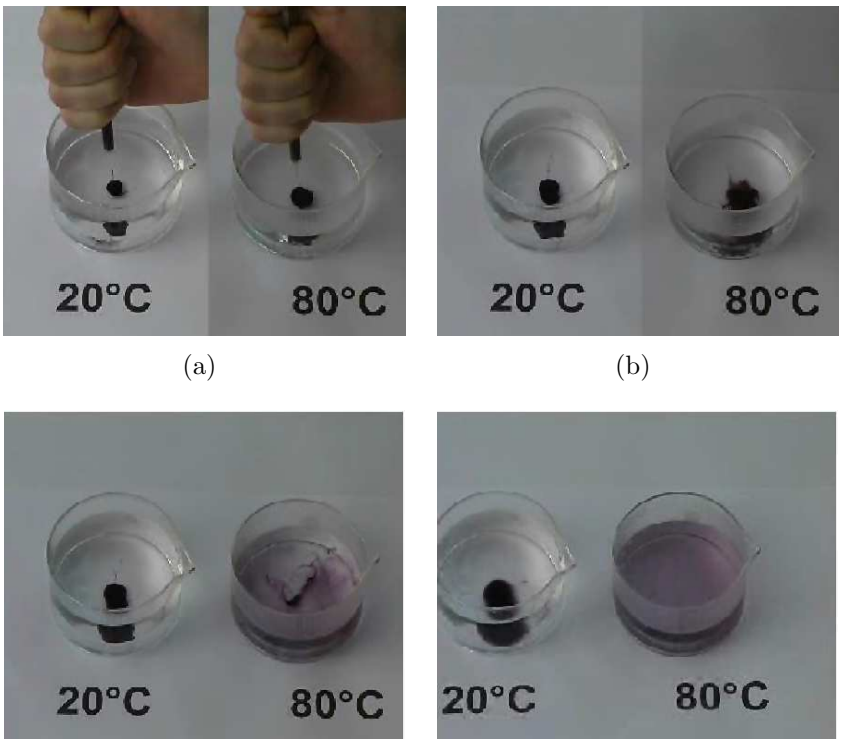

(a) (b)

(c) (d)

Figure 1.1: (a) A drop of ink is introduced into two flasks filled with water at temperatures of 20°C (left) and 80°C (right). Figs.(b),(c), and (d) show the evolution of the diffusion process over time. (*Video courtesy of Würzburg University*).

diffusion may be isotropic or anisotropic, depending on whether it correlates with the orientation of the considered tissue. For example, within the brain's gray matter diffusion is isotropic and may be characterized by a single (scalar) apparent diffusion coefficient. On the contrary, within white matter diffusion is anisotropic: water molecules diffuse more freely along the direction of neuronal fibers (Henkelman et al. [1994]; Moseley et al. [1990a, 1991]). In white matter water diffusion may therefore be characterized by a symmetric diffusion tensor D. A schematic representation of the difference of the diffusion process in gray and white matter is presented in Fig. 1.2.

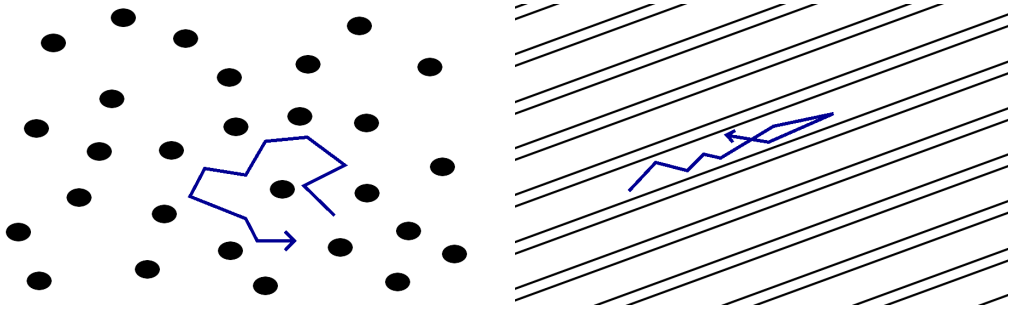

(a) (b)

Figure 1.2: (a) The extracellular Brownian motion of water molecules in gray matter is hindered mainly by neural cell bodies. Diffusion at voxel scale is isotropic. (b) In white matter the extracellular Brownian motion of water molecules is hindered mainly by myelinated axon tracts. Diffusion is anisotropic.

1.1 Diffusion Magnetic Resonance

Nuclear magnetic resonance (NMR) imaging allows the non invasive, *in-vivo* imaging of the diffusion characteristics of human tissue. A typical NMR scan starts by placing the specimen into a constant magnetic field B. A 90 degree radiofrequency (rf) pulse then tilts the magnetization vectors of the considered nuclei (e.g. hydrogen) into the plane perpendicular to B. This causes the spins of the considered nuclei to start precessing around the magnetic field with an angular frequency ω given by

$$\omega = \gamma B \tag{1.2}$$

where γ is the gyromagnetic ratio - a constant property of the considered nuclei. Hydrogen for example has a gyromagnetic ratio of approximately $2.68 \cdot 10^8$ rad/s/Tesla. With time the initially coherent spins dephase due to factors such as dipolar interactions and magnetic field inhomogeneities caused by differences in magnetic susceptibility between different biological tissues. This causes a decay in the voltage (signal) induced in the receiver of the magnetic resonance scanner.

As proposed by Edwin Hahn (Hahn [1950]) the dephasing due to magnetic field inhomogeneities can be reversed through the subsequent application of a 180 degree rf pulse, leading to the formation of an "echo signal". The time between the 90 degree rf pulse and the peak of the echo signal is called the time of echo (TE) and corresponds to twice the time between the two rf pulses. The generated

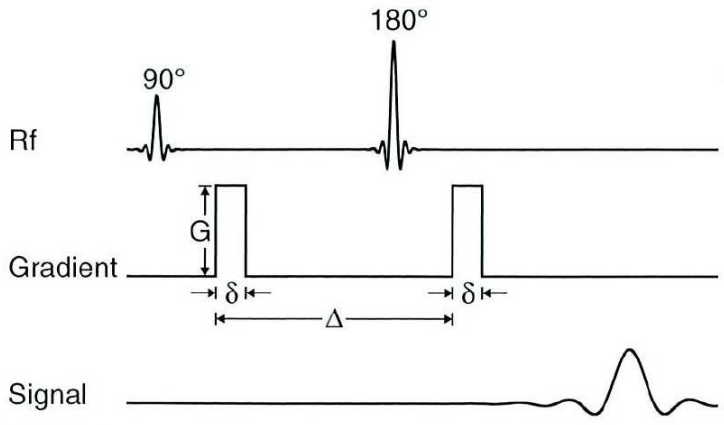

Figure 1.3: A schematic of the pulsed field gradient spin-echo MR technique introduced by Stejskal and Tanner. (*Source: Johansen-Berg and Behrens [2009]*).

echo is detected by the receiver (MR coil) of the scanner and used to generate the output image. A schematic representation of the two applied rf pulses is presented at the top of Fig. 1.3. Let us note that the time that exists between successive pulse sequences applied to the same slice will be denoted in the following by time of repetition (TR).

In order to measure molecular diffusion, Carr and Purcell (Carr and Purcell [1954]) proposed to activate a constant magnetic field gradient throughout the entire Hahn spin-echo experiment. The idea is that because of the magnetic field gradient, spins at different locations experience different magnetic fields and therefore precess with different angular frequencies, according to Eq. 1.2. Due to random molecular diffusion, spins acquire different phase shifts, so that phase coherence after the application of the 180 degree rf pulse is decreased and so is the echo magnitude. A stronger gradient leads to a larger phase change and thus to a higher sensitivity on diffusion of the employed MR sequence. In clinical applications the strength of the gradient is often indicated by means of the "*b*-value", which is proportional to the square of the gradient strength.

Modern diffusion sensitive MR sequences are generally based upon the pulsed field spin-echo technique introduced by Stejskal and Tanner (Stejskal and Tanner [1965]). The great innovation of this sequence is that Carr and Purcell's constant magnetic field gradient is replaced by two short duration gradient pulses, see

Fig. 1.3. Hence, there is a clear distinction between the encoding time (pulse duration, δ) and the diffusion time (time between the application of the two gradient pulses, Δ). Let us recall that the angular frequency corresponds to the rate of change of the phase:

$$\frac{d\phi}{dt} = \omega \ . \tag{1.3}$$

If we consider the pulse duration δ to be small and neglect the diffusion taking place during pulse application, the net phase change ϕ_1 induced by the first gradient to a particle at position x_1 can be written as

$$\begin{aligned} \phi_1(x_1) &= -\omega(x_1)\delta \\ &= -\gamma(Gx_1)\delta =: -qx_1 \end{aligned} \tag{1.4}$$

where $q = \gamma\delta G$ combines the experimental parameters, with G being the magnitude of the gradient pulse. In Eq. 1.4 we ignore the phase change due to the magnetic field B_0 which is constant for all spins in the ensemble. The minus sign in the equation is necessary for protons whose precession is in the clockwise direction on the plane perpendicular to the magnetic field. After the diffusion time Δ the particle will be located at position x_2 with an inverted direction of precession because of the 180 degree rf pulse. The net phase change ϕ_2 induced by the second gradient corresponds to

$$\phi_2(x_2) = qx_2 \ . \tag{1.5}$$

Finally, the aggregate phase change of the particle is

$$\begin{aligned} \phi_1(x_1) + \phi_2(x_2) &= -qx_1 + qx_2 \\ &= q(x_2 - x_1) \ . \end{aligned} \tag{1.6}$$

If particles remain stationary the aggregate phase change is 0. In the presence of random molecular spreading ϕ_1 and ϕ_2 generally do not cancel out, leading to phase dispersion or to a spreading of phases within the excited volume. Therefore the overall signal, given by the sum of the magnetic moments of all spins, is attenuated due to the incoherence in the orientations of individual magnetic

moments.

Let us now consider the MR signal attenuation $E(q)$, given by the diffusion-weighted signal $S(q)$ divided by the signal in the absence of any gradient $S(0) = S_0$:

$$E(q) = \frac{S(q)}{S_0} \ . \tag{1.7}$$

Relaxation-related signal attenuation in the diffusion-weighted signal is approximately independent of the applied gradient and is canceled out by the division. Therefore $E(q)$ measures the signal attenuation which can be attributed solely to diffusion. Assuming a constant spin density throughout the volume to be imaged, the MR signal attenuation may be written as

$$E(q) = \int\int P(x_1, x_2, \Delta)\, e^{-iq(x_2 - x_1)}\, dx_2\, dx_1 \tag{1.8}$$

where P is the diffusion propagator: a probability density function (PDF) which corresponds to the likelihood that a particle initially located at x_1 is located at x_2 after a diffusion time Δ. The exponential factor in Eq. 1.8 can be considered as a "Fourier kernel" which transforms the displacement-dependent function $P(x_1, x_2, \Delta)$ into a function of q: $E(q)$. A sum over all possible displacements $x_2 - x_1$ is carried out by means of the double integral. For example we may assume the diffusion propagator to be a three dimensional normal PDF given by

$$P(x_1, x_2, \Delta) = \frac{1}{(2\pi)^{\frac{3}{2}} \sqrt{2\left(\Delta - \frac{\delta}{3}\right)|D|}}\, e^{-\frac{1}{2}\frac{1}{2\left(\Delta - \frac{\delta}{3}\right)}(x_1 - x_2)^T D^{-1} (x_1 - x_2)} \tag{1.9}$$

with mean x_2 and variance $2\left(\Delta - \frac{\delta}{3}\right) D$, where D is the diffusion tensor - a 3×3 matrix which will be discussed more in detail later in this chapter. This assumption provides the foundation for diffusion tensor imaging (DTI). The resulting MR signal attenuation is then given by

$$\begin{aligned} E(q) &= e^{-\frac{1}{2} 2\left(\Delta - \frac{\delta}{3}\right) q^T D q} \\ &= e^{-\left(\Delta - \frac{\delta}{3}\right) q^T D q} \ . \end{aligned} \tag{1.10}$$

where $q = \gamma\delta G$ and G is now a three dimensional vector the magnitude and

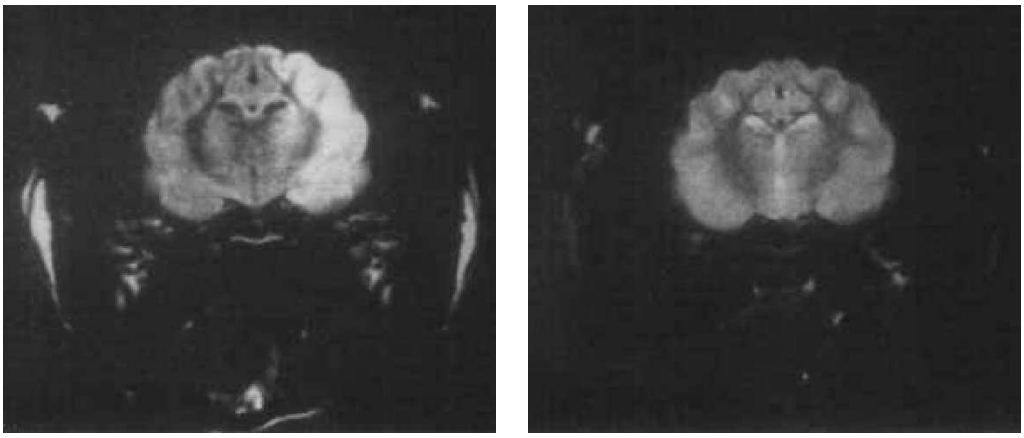

(a) (b)

Figure 1.4: (a) A diffusion-weighted, spin-echo image of a cat's brain taken 45 minutes after the right middle cerebral artery has been occluded. (b) The corresponding T2-weighted, spin-echo image taken 65 minutes postocclusion. A significant hyperintensity in the ischemic hemisphere can be observed in the diffusion-weighted image but not in the T2-weighted image. (*Source: Moseley et al. [1990b]*).

direction of which correspond to the strength and the axis of the applied diffusion gradient, respectively. The b-value discussed above is computed as

$$b = |q|^2 \left(\Delta - \frac{\delta}{3} \right) \quad . \tag{1.11}$$

In one dimension $P(x_1, x_2, \Delta)$ and $E(q)$ simplify accordingly. From a clinical perspective, one of the first successful applications of diffusion-weighted imaging (using one dimensional apparent diffusion coefficients) has been the early detection and control of ischemic strokes (Moseley et al. [1990b]). These brain lesions are associated with reduced water diffusion and can be detected as bright areas of signal hyperintensity in the diffusion-weighted images, see Fig. 1.4 for an example.

Common artifacts that need to be considered during the pre-processing stage of diffusion-weighted images include susceptibility effects, eddy current induced distortions, and subject motion (Jones and Cercignani [2010]). The different magnetic susceptibility characteristics varying between tissues (white and gray matter, air, bone) locally alter the magnetic field B_0, which causes not only

signal loss but also geometric distortions and discontinuities at tissue interfaces. By means of an additional image acquisition with different TE, the B_0 field can be measured directly and a voxel-by-voxel relocation and intensity correction can be achieved (a technique known as "unwarping", see e.g. Jezzard and Balaban [1995], Reber et al. [1998] for details). Eddy currents are electric currents induced in a conductor exposed to a changing magnetic field such as, for example, a diffusion-encoding gradient. They generate local magnetic field gradients that will either add or subtract from the gradients that are used for spatial encoding. Eddy current induced distortions can typically be recognized by a rim of high anisotropy along the direction of the phase-encoding gradient. However, all voxels are corrupted by eddy currents, and need to be corrected. This can be achieved through a slice-by-slice registration of the diffusion-weighted image to the baseline image. At the same time, registration corrects for subject motion, although care has to be taken in contemporarily re-orienting the diffusion-encoding gradients.

1.2 Diffusion Tensor Imaging

We mentioned before that diffusion in gray matter occurs along axonal tracts and is therefore anisotropic. Conversely, knowledge about local diffusion characteristics within the brain provides insights into cell structure and neural pathways. Assuming, as in Eq. 1.9, that the diffusion propagator within an image voxel can be described as a Gaussian distribution, Basser and Le Bihan [1992] noted that the diffusion tensor D can be estimated by means of a series of diffusion-weighted signals. For simplicity, we shall assume in the following that the b-value is kept constant between successive measurements.

The diffusion tensor D is a 3×3 symmetric positive-definite matrix:

$$D = \begin{pmatrix} D_{xx} & D_{xy} & D_{xz} \\ D_{xy} & D_{yy} & D_{yz} \\ D_{xz} & D_{yz} & D_{zz} \end{pmatrix} \tag{1.12}$$

where the entries D_{xx}, D_{yy}, and D_{zz} correspond to the apparent diffusion coefficients in x, y, and z directions (the three axes of the scanner measurement frame),

respectively. The mixed entries D_{xy}, D_{xz}, and D_{yz} correspond to the covariance between displacements along those orthogonal axes. We may rewrite D as a six-dimensional vector

$$\vec{D} = [D_{xx}, D_{xy}, D_{xz}, D_{yy}, D_{yz}, D_{zz}]^T \ . \tag{1.13}$$

Given the six unknown entries of $\vec{D}$ we need at least six diffusion-weighted images to reconstruct D, in addition to one baseline image S_0. Usually more than six measurements are acquired in order to increase robustness to image noise. Combining equations 1.7 and 1.10 the diffusion-related signal attenuation for the n-th gradient q_n is given by

$$\begin{aligned} E(q_n) =& \frac{S(q_n)}{S_0} \\ =& e^{-\left(\Delta - \frac{\delta}{3}\right) q_n^T D q_n} \\ =& e^{-b \hat{q}_n^T D \hat{q}_n} \end{aligned} \tag{1.14}$$

where $\hat{q}_n$ equals to $q_n/|q_n|$. The above expression is equivalent to

$$\begin{aligned} \underbrace{\ln\left(\frac{S(\hat{q}_n)}{S_0}\right)/(-b)}_{:=a_n} =& \hat{q}_n^T D \hat{q}_n & \Leftrightarrow \\ a_n =& \underbrace{\hat{q}_{n_1}^2}_{:=c_{n_1}} D_{xx} + \underbrace{\hat{q}_{n_2}^2}_{:=c_{n_2}} D_{yy} + \underbrace{\hat{q}_{n_3}^2}_{:=c_{n_3}} D_{zz} \\ &+ \underbrace{2\hat{q}_{n_1}\hat{q}_{n_2}}_{:=c_{n_4}} D_{xy} + \underbrace{2\hat{q}_{n_1}\hat{q}_{n_3}}_{:=c_{n_5}} D_{xz} + \underbrace{2\hat{q}_{n_2}\hat{q}_{n_3}}_{:=c_{n_6}} D_{yz} & \Leftrightarrow \\ a_n =& c_{n_1} D_{xx} + c_{n_2} D_{yy} + c_{n_3} D_{zz} + c_{n_4} D_{xy} + c_{n_5} D_{xz} + c_{n_6} D_{yz} \end{aligned} \tag{1.15}$$

For n gradient directions we obtain a system of n linear equations:

$$\begin{aligned} a_1 =& c_{1_1} D_{xx} + c_{1_2} D_{yy} + c_{1_3} D_{zz} + c_{1_4} D_{xy} + c_{1_5} D_{xz} + c_{1_6} D_{yz} \\ &\vdots \\ a_n =& c_{n_1} D_{xx} + c_{n_2} D_{yy} + c_{n_3} D_{zz} + c_{n_4} D_{xy} + c_{n_5} D_{xz} + c_{n_6} D_{yz} \end{aligned} \tag{1.16}$$

which can be rewritten in vector-matrix notation as

$$A = C\vec{D} \ . \tag{1.17}$$

Since there are more equations than unknowns, the system is generally solved via "ordinary least squares", by computing the pseudoinverse of C:

$$\vec{D} = (C^T C)^{-1} C^T A \ . \tag{1.18}$$

It becomes clear that, in order for Eq. 1.18 to have a unique solution, at least six gradient directions must be linearly independent. There are alternative approaches based on "weighted linear least squares" or "non-linear least squares" (Koay et al. [2006]) which lead to a more precise estimate of D, at the cost of computation time.

The diffusion tensor is often visualized by means of the corresponding ellipsoid, i.e. the set of points $x \in \mathbb{R}^3$ satisfying

$$x^T D^{-1} x = 1 \ . \tag{1.19}$$

The eigenvectors of D correspond to the principal axes of the of the ellipsoid, the length of which is scaled according to the square root of the eigenvalues of D. A schematic representation is presented in Fig. 1.5.

The direction of the eigenvector corresponding to the largest eigenvalue is often referred to as the "main diffusion direction", since the probability of particles at the center of the ellipsoid to diffuse in this direction is the highest. Pajevic and Pierpaoli [1999] suggested to color-code the diffusion tensor ellipsoids by mapping the components of the main diffusion direction vector to red, green, and blue (RGB) values, a scheme that has since become commonly used. In Fig. 1.6 we present examples of diffusion tensor matrices together with the corresponding color-coded ellipsoids.

Important parameters derived from the diffusion tensor include its trace and anisotropy indices. The trace of a diffusion tensor D is given by the sum of its

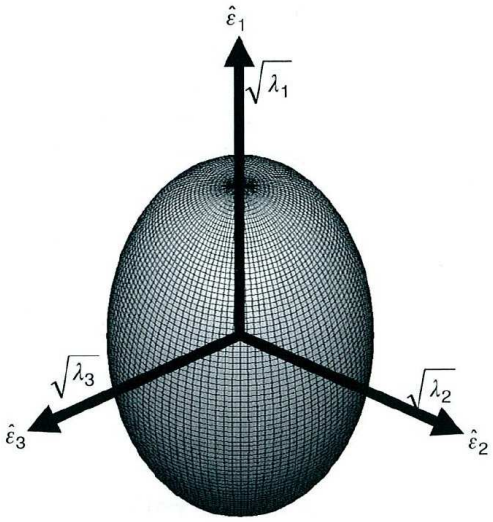

Figure 1.5: Schematic representation of the diffusion tensor ellipsoid. The principal axes $\hat{\varepsilon}_1, \hat{\varepsilon}_2$ and $\hat{\varepsilon}_3$ correspond to the eigenvectors of D and are scaled according to the square root of the eigenvalues λ_1, λ_2 and λ_3. (*Source: Johansen-Berg and Behrens [2009]*).

diagonal elements, which is also equal to the sum of its eigenvalues:

$$\mathrm{Tr}(D) = D_{xx} + D_{yy} + D_{zz} = \lambda_1 + \lambda_2 + \lambda_3 \ . \tag{1.20}$$

The average eigenvalue $\langle\lambda\rangle := \mathrm{Tr}(D)/3$ can be considered as a mean diffusivity measure which is independent of the main diffusion direction. Notably for b-values smaller than 1500 s/mm^2 the mean diffusivity in white and gray matter is similar (Pierpaoli et al. [1996]). Thanks to this property mean diffusivity maps allow to promptly recognize diffusion abnormalities without the confounding effects due to anisotropic diffusion. The two most popular anisotropy indices in literature are fractional anisotropy (FA) and relative anisotropy (RA), computed as

$$FA = \sqrt{\frac{3}{2}} \frac{\sqrt{(\lambda_1 - \langle\lambda\rangle)^2 + (\lambda_2 - \langle\lambda\rangle)^2 + (\lambda_3 - \langle\lambda\rangle)^2}}{\sqrt{\lambda_1^2 + \lambda_2^2 + \lambda_3^2}} \tag{1.21}$$

$$RA = \sqrt{\frac{1}{3}} \frac{\sqrt{(\lambda_1 - \langle\lambda\rangle)^2 + (\lambda_2 - \langle\lambda\rangle)^2 + (\lambda_3 - \langle\lambda\rangle)^2}}{\langle\lambda\rangle} \ . \tag{1.22}$$

These indices are independent with respect to the main diffusion direction of the

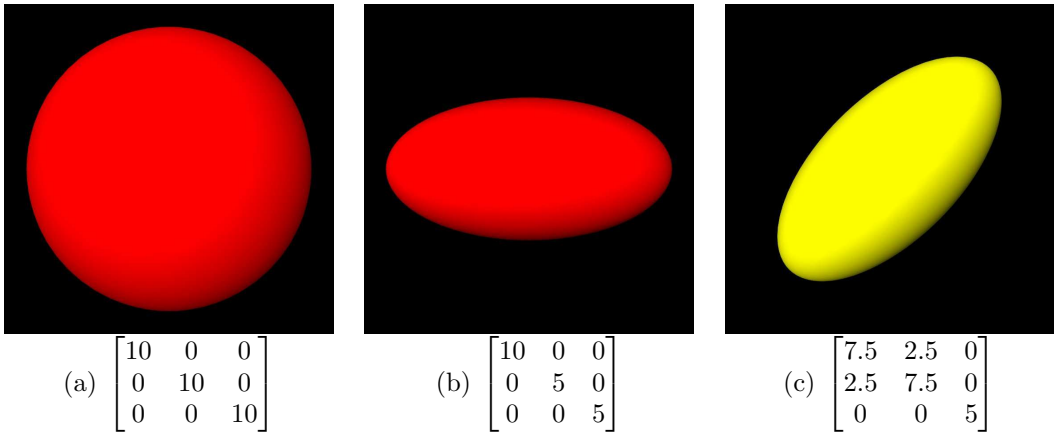

(a) $\begin{bmatrix} 10 & 0 & 0 \\ 0 & 10 & 0 \\ 0 & 0 & 10 \end{bmatrix}$ (b) $\begin{bmatrix} 10 & 0 & 0 \\ 0 & 5 & 0 \\ 0 & 0 & 5 \end{bmatrix}$ (c) $\begin{bmatrix} 7.5 & 2.5 & 0 \\ 2.5 & 7.5 & 0 \\ 0 & 0 & 5 \end{bmatrix}$

(d) $\begin{bmatrix} 5 & 0 & 0 \\ 0 & 10 & 0 \\ 0 & 0 & 5 \end{bmatrix}$ (e) $\begin{bmatrix} 1 & 0 & 0 \\ 0 & 10 & 0 \\ 0 & 0 & 1 \end{bmatrix}$ (f) Color-coding Sphere

Figure 1.6: Examples of diffusion tensor matrices together with the corresponding color-coded ellipsoids. The eigenvectors of (a),(b),(d),(e) are aligned with the axes of the measurement frame, therefore the off diagonal elements are 0. In (a) D_{xx}, D_{yy}, and D_{zz} are equal and therefore diffusion is isotropic. The other tensors correspond to anisotropic diffusion. Tensors (c) and (d) result from a rotation of (b) about the z-axis by an angle of 45 and 90 degrees, respectively. Notice how in (c) D_{xy} is not 0, reflecting the correlation of diffusion along the x-axis and the y-axis. Tensor (e) presents the highest magnitude difference between eigenvalues. (f) illustrates the employed ellipsoid color-coding which is based on the main diffusion direction.

tensor and do not require the sorting of eigenvalues according to their magnitude in order to be computed. Both FA and RA characterize anisotropy by computing the variance of the three eigenvalues, which is then normalized to account for local differences in diffusivity magnitude. FA normalizes the variance by the Frobenius norm of D while RA normalizes the variance by the mean diffusivity $\langle\lambda\rangle$. The leading constant factors cause FA and RA to take values between 0 and 1. The

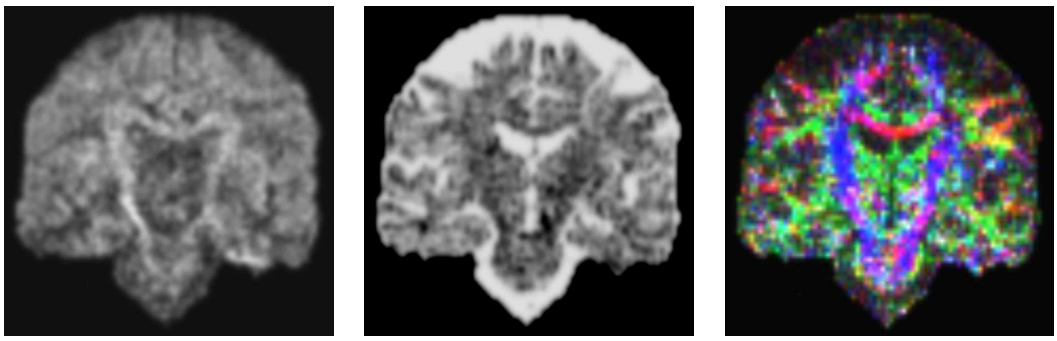

(a) (b) (c)

Figure 1.7: (a) Example of a diffusion-weighted image with gradient direction $(0.32, -0.94, 0.095)^T$. The acquisition parameters are as follows: resolution = $1.80 \times 1.80 \times 1.98$ mm^3, b-value = 1000 s/mm^2, TR/TE = 12000/84 ms, two repetitions with one b=0 image and 30 gradient directions each. (b) The corresponding mean diffusivity map. (c) The corresponding color-coded FA map. The color coding depends on the main diffusion direction as illustrated in Fig. 1.6(f). The superior-inferior corticospinal tracts (in blue) and the left-right corpus callosum (in red) are clearly discernible.

user should be aware that for b-values smaller than 1500 s/mm^2, as the signal to noise ratio is lowered, FA and RA are increasingly overestimated (Pierpaoli and Basser [1996]). However, for b-values greater than 3000 s/mm^2, anisotropy indices are generally underestimated (Jones and Basser [2004]). Great care should therefore be taken when comparing anisotropy indices in images with different acquisition parameters. Fig. 1.7 shows examples of a diffusion-weighted image, a mean diffusivity map, and a color-coded FA map.

1.3 Fiber Tracking

Once a diffusion tensor image has been computed based on the acquired diffusion-weighted images, fiber tractography allows the non-invasive and *in vivo* reconstruction of neural fiber bundles. The most intuitive and commonly used fiber-tracking algorithm is streamline tractography. A streamline is a line l through a vector field ε_1, the tangent of which is always parallel to the vector field. Starting with a diffusion tensor image the vector field is given by the main diffusion directions. Assuming that l is parametrized by means of a variable $s \in [a, b] \subset \mathbb{R}$,

the streamline property can be expressed mathematically as (Basser et al. [2000])

$$\frac{\mathrm{d}l(s)}{\mathrm{d}s} = \varepsilon_1(l(s)) \ . \tag{1.23}$$

This is an ordinary differential equation which, given a starting point $l(a) = x_0$ can be solved for example by means of the Euler method. With this method the derivative is approximated by a forward difference, giving the iterative scheme

$$\begin{aligned} \frac{l_{i+1} - l_i}{h} &= \varepsilon_1(l_i) \qquad \Leftrightarrow \\ l_{i+1} &= l_i + h \cdot \varepsilon_1(l_i) \end{aligned} \tag{1.24}$$

where h is the step size. A drawback of this method is that errors in the estimation of the main diffusion direction lead to errors in the computed streamline which accumulate and increase the further away the streamline is from the starting point x_0. Another important question is how to determine the vector at position $\varepsilon_1(l_i)$, given that the vector field is defined only on the discrete image grid. The FACT algorithm proposed by Mori et al. [1999] (see Fig. 1.8 for a schematic example) considers the main diffusion direction valid for the entire voxel while later approaches (e.g. Pajevic et al. [2002]) interpolate information from neighboring voxels in order to increase the streamline's accuracy. The tracking is typically stopped when the FA value of a voxel is below a predefined threshold (because the information about the main diffusion direction becomes unreliable, e.g. in regions of crossing fibers) or when the angle between successive line segments is above a predefined threshold (because the result would be unrealistic from an anatomical point of view).

A typical procedure to reconstruct neural fiber bundles involves defining a seed region of interest, which determines the voxels from where the streamlines start, and subsequently eliminating streamlines that are not in accordance with *a priori* anatomical knowledge. Alternatively the user may seed the fiber tracking algorithm in every voxel in the brain and only select the streamlines that pass through one or several regions of interest (Stieltjes et al. [2001], Catani et al. [2002]). Several examples of reconstructed fiber bundles are displayed in Fig. 1.9.

Possible clinical fiber-tracking applications include the comparison of quan-

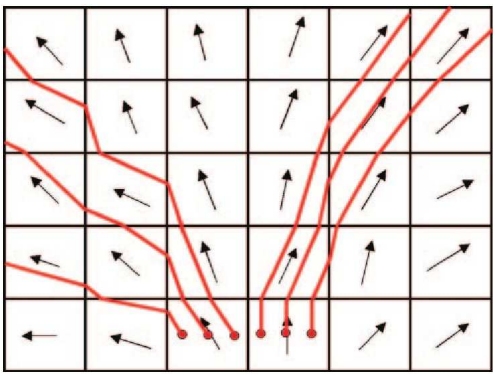

Figure 1.8: Schematic of the FACT algorithm (Mori et al. [1999]). (*Source: Mukherjee et al. [2008]*).

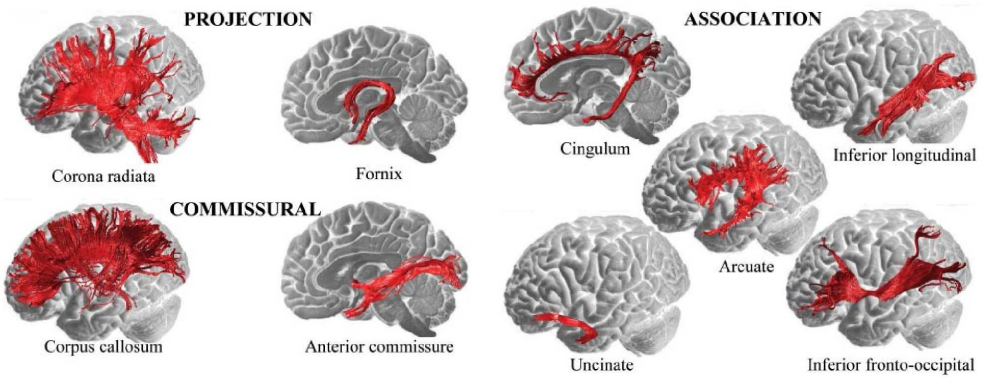

Figure 1.9: Several examples of reconstructed fiber bundles. (*Source: Catani and ffytche [2005]*).

titative measures (e.g. FA) across subjects as well as pre- and intra-operative neurosurgical planning (see Fig. 1.10 for an example). Neurosurgical intervention is exceptionally challenging in the presence of tumors such as anaplastic astrocytomas or glioblastomas multiforme, which are highly infiltrating and often surrounded by perifocal edema. Because of this, the borders of the tumor are difficult to distinguish even with the help of a surgical microscope and the anisotropy of diffusion within tissue surrounding the tumor is significantly decreased. This makes it particularly difficult to reconstruct fiber bundles bordering the tumor, and thus to reach the goal of a maximum resection volume without incurring in postoperative neurosurgical deficits (Keles et al. [2006]; Pope et al. [2005]; Sanai and Berger [2008]). Additionally, the different steps of the fiber reconstruction

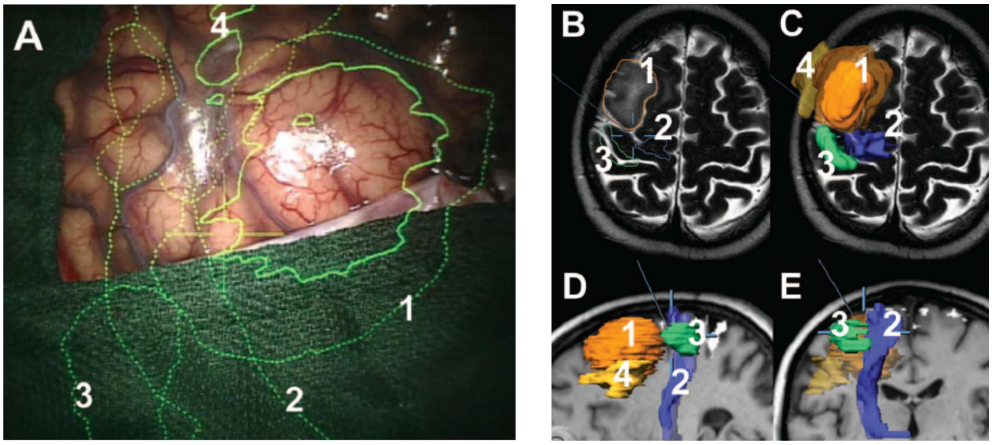

Figure 1.10: Intraoperative view (53 years old women with WHO II Oligoastrocytoma). (A) microscope view after opening of the dura, the four contours show: 1 - the segmented tumor, 2 - the corticospinal tract, 3 - motor fMRI activity, 4 - speech fMRI activity. (B,C) T2-weighted axial view in which the structures are displayed as contours in the plane (B) or as 3D renderings (C). (D,E) T1-weighted coronal and sagittal view. (*Image courtesy of Ch. Nimsky*).

pipeline (image acquisition, choice of the diffusion model, choice of the fiber tracking algorithm, regions of interest, and parameters) are all prone to error and need validation. For example, the current resolution of diffusion-weighted images in the clinical setting is of approximately $2 \times 2 \times 2 \times \text{mm}^3$, therefore images are often corrupted by partial-volume artifacts and structures smaller than the size of a voxel cannot be resolved.

Consequently, it is essential to assess the limits of diffusion tensor imaging and fiber-tracking algorithms. Possible non-invasive options include synthetic software and hardware phantoms with a known ground truth. Software phantoms are generally coarse approximations of the neural fiber bundles and the magnetic resonance sequence they intend to simulate. Their advantage is that they can be easily manipulated to reproduce different fiber paths and scanner parameters. Several software phantoms with a varying degree of realism have been proposed over the years. In early work on the topic Tournier et al. [2002] model a torus shaped bundle and incorporate partial-volume effects into the model (Fig. 1.11(a)). Lori et al. [2002] and similarly Gössl et al. [2002] model helical fiber pathways (Figs. 1.11(b) and 1.11(d)). In the latter work also crossing fibers are modeled. In Leemans

et al. [2005] a fiber system with pathways having random curvatures is proposed (Fig 1.11(e)) and fiber bundles have smoothly varying diffusion properties along their cross section (Fig. 1.11(c)). These phantoms have been used to compare different fiber tracking algorithms, to test their robustness to bending, crossing, or kissing pathways, and to fine tune their parameters.

Compared to software phantoms, physical (hardware) phantoms are often limited by a relatively simple geometry of the fiber paths but include the true noise and artifacts of the employed imaging sequence. The first synthetic hardware phantoms in a diffusion MRI study were polytetrafluoroethylene (PTFE) capillaries filled with water (Von dem Hagen and Henkelman [2002]). A similarly constructed phantom has been employed by Lin et al. [2003] to investigate diffusion at fiber crossings. Yanasak and Allison [2006] chose to build a phantom made of glass capillaries, with a range of diameters much smaller than the ones of previous PTFE phantoms and similar to those found in neuronal tissue (23,48, and 82 μm). Recent work (see e.g. Perrin et al. [2005b], Fieremans et al. [2008]) has introduced phantoms made of synthetic fibers such as nylon, rayon, or ultra-high molecular weight polyethylene fibers wrapped into cylindrical tubes and permeated with water. Unlike capillary-based phantoms these phantoms do not present artificial central cavities in which the water flows, increasing the applicability of the respective studies to the clinical setting.

1.4 Outline of the Thesis

This work is structured as follows. In **Chapter 2** we analyze the error magnitude of streamline fiber-tracking. To do this, we generate realistic software phantoms of neural fiber bundles for which we systematically vary the imaging and tracking parameters. The value of a novel error measure for fiber reconstructions is determined for each set of parameters. Based on our findings, we propose a fuzzy segmentation algorithm for diffusion tensor images which allows a better estimate of the spatial extent of tracked bundles and conveys to the user the noise-related uncertainties in the estimated main diffusion directions.

In **Chapter 3** we further develop our ideas to increase the accuracy of fiber bundle reconstruction when compared to streamline tractography. We present a

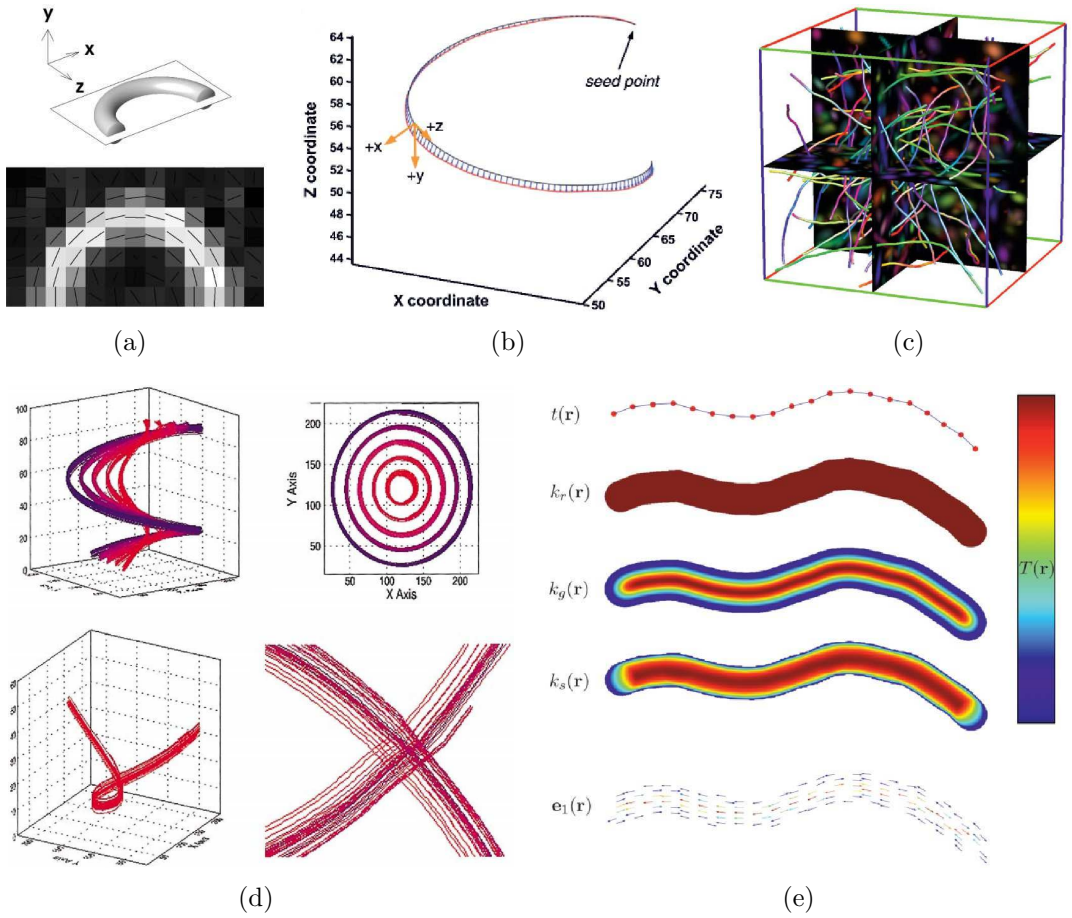

Figure 1.11: (a) Torus shaped bundle (*Tournier et al. [2002]*). (b) Helical fiber pathway (*Lori et al. [2002]*). (c) Fiber system with pathways having random curvatures (*Leemans et al. [2005]*). (d) Helical fiber pathway (top) and crossing fibers (bottom) (*Gössl et al. [2002]*). (e) Smoothly varying diffusion properties along the cross section of the fiber bundles (*Leemans et al. [2005]*).

hybrid approach which combines the higher spatial accuracy of tensor clustering methods with the ability of probabilistic tractography to reconstruct pathways that do not follow the main tensor diffusion directions. We are careful about keeping the user interaction simple, so that the algorithm may be readily integrated into clinical routine.

Chapter 4 addresses the sensitivity of streamline fiber-tracking to seed- and exclude-regions of interest delineated by the user. This is done by applying a non-rigid transformation to a fiber bundle from a fiber atlas so that the transformed

bundle "best fits" the diffusion tensor data of the patient. The transformation is determined by means of a multi-scale simulated annealing method. The applicability of this proof-of-concept algorithm is demonstrated on fiber bundles which are cut or considerably displaced by lesions.

In **Chapter 5** we focus on how uncertainty-related information can be visualized by color-coding the reconstructed fiber bundles and by means of individual "confidence hulls". More in detail, we simulate the growth of a glioblastoma multiforme adjacent to the tracked corticospinal tract and employ a specific color-coding to make the user aware of changes in the volume of the tumor over time. Additional color-codings are suggested to convey information about the image data quality and about the confidence in the accuracy of the traced streamlines. The size of the computed confidence hulls depends on the local similarity between tensors, on the image acquisition parameters, and on the level of image noise.

A summary of the main results together with a concluding discussion is presented in **Chapter 6**.

Acknowledgments

This chapter of the thesis is based in part on Johansen-Berg and Behrens [2009][Chapters 1,3,15 and 16].

Chapter 2

Segmentation of Fiber Tracts Based on an Accuracy Analysis on Diffusion Tensor Software Phantoms

This chapter of the thesis is based on the publication Barbieri et al. [2011b] with minor typographical corrections.

2.1 Abstract

Due to its unique sensitivity to tissue microstructure, one of the primary applications of diffusion-weighted magnetic resonance imaging is the reconstruction of neural fiber pathways by means of fiber-tracking algorithms. In this work, we make use of realistic diffusion-tensor software phantoms in order to carry out an analysis of the precision of streamline tractography by systematically varying certain properties of the simulated image data (noise, tensor anisotropy, and image resolution) as well as certain fiber-tracking parameters (number of seed points and step length). Building upon the gained knowledge about the precision of the analyzed fiber-tracking algorithm, we proceed by suggesting a fuzzy segmentation algorithm for diffusion tensor images which better estimates the precise

spatial extent of a tracked fiber bundle. The presented segmentation algorithm utilizes information given by the estimated main diffusion direction in a voxel and the respective uncertainty, and its validity is confirmed by both qualitative and quantitative analyses.

2.2 Introduction

Diffusion tensor imaging (DTI) is a magnetic resonance imaging method which allows measuring the anisotropic diffusion of water molecules in in-vivo biological tissue, such as white matter (WM) in the brain (Basser et al. [1994b]; Neil et al. [1998]; Pierpaoli and Basser [1996]). An important application of DTI is fiber tractography, which assumes that the principal diffusion direction matches the orientation of the corresponding underlying fiber system and thus allows the reconstruction of the 3D architecture of WM fiber pathways (Basser [1998]; Mori et al. [1999]; Parker et al. [2002]). In recent years, fiber tractography has become well established in the research environment, with first clinical uses being reported. Hardware or software phantoms, which constitute a model with a known fiber network, are one of the primary tools for investigating the validity and precision of fiber-tracking algorithms (Fieremans et al. [2008]; Gössl et al. [2002]; Lori et al. [2002]). Software phantoms have the advantage that they can be easily modified to account for different scanner parameters, image noise, or artifacts.

In this contribution, we analyze the extent to which different properties of the image data and tracking parameters influence the precision with which a fiber bundle is reconstructed. We choose to focus on the analysis of streamline tractography versus alternative probabilistic approaches (for an overview on different tractography algorithms, see Behrens and Jbabdi [2009]), because of its widespread clinical use and quick computation times. We start by considering a software phantom of relatively simple geometry shaped as a torus segment. This phantom allows us to fully control the spatial extent and diffusion properties of the fiber bundle and the diffusion properties of the adjacent tissue. As far as the image data is concerned, we test how different levels of image noise influence the reconstruction of the tract. We are particularly interested in the distance between the tracked streamlines and the true border of the bundle. Furthermore,

we test how high the anisotropy of tensors belonging to the bundle needs to be in order to guarantee a reasonably precise reconstruction of the tract. Specifically, due to partial-volume effects with the fixed background tensors, different anisotropy values affect the main diffusion directions estimated at the border of the bundle. This analysis may, for example, be interesting when delimiting regions of fiber crossings where streamline tractography is unreliable. Finally, we would like to analyze the effect of image resolution on tracking results by varying the diameter of the fiber bundle; varying the diameter of the fiber bundle while keeping the voxel size constant corresponds to analyzing tracking results for a fiber bundle of constant width and different image resolutions. Regarding the fiber-tracking algorithm, we analyze the influence of a different number of seed points and different step lengths on the precision of the tract reconstruction.

Next, we repeat an analogous analysis of the precision of streamline tractography on anatomically realistic models of specific neural fiber bundles. The spatial extent of the modeled bundles is determined by using a white matter atlas and the anisotropy of the tensors is set to values reported in the literature. Specifically, we generate models of the corticospinal tract and arcuate fasciculus. We are able to simulate image noise and partial-volume effects caused by the possible simultaneous presence of different white matter pathways, grey matter, and cerebrospinal fluid in one voxel.

In the last section of this article, we suggest an efficient algorithm to generate a fuzzy segmentation of the tracked fiber bundle. The algorithm may be used to better grasp the true spatial extent of a tracked bundle. For examples of both crisp and fuzzy, parametric and nonparametric DTI segmentation algorithms, see Awate et al. [2007]; Wiegell et al. [2003]; Ziyan et al. [2006]. Our approach accounts for not only the direction of the major eigenvectors of the underlying tensor field, but also the respective covariance matrices. Whereas several authors have analyzed tract dispersion via perturbation methods (Anderson [2001]; Basser [1997]; Chang et al. [2007]; Hext [1963]), we make use of nonlinear least-squares methods for tensor reconstruction and the explicit formulation of the covariance matrix of the main diffusion vector given in Koay et al. [2006, 2007, 2008]. The estimated border is visualized as a semi-transparent hull around the tracked fiber bundle. We test the algorithm both on the generated DTI phantoms and on a

real magnetic resonance dataset.

2.3 Generating and Analyzing Fiber-Tracking Error on a Torus-Shaped DTI Phantom

In this section, we introduce the methodology used to generate our diffusion tensor software phantoms. We compute fiber-tracking results upon a model shaped as a torus segment, where we systematically vary the underlying image data and fiber-tracking parameters. In order to perform a quantitative analysis of the precision of the bundle reconstruction, we suggest a novel error measure for tracking results. Although it is intuitively clear that there is a greater streamline density at the center of a tracked bundle than on its border, we analyze the spatial distribution of the tracked fibers and quantify this disparity.

2.3.1 DTI Model Framework

In order to generate a synthetic diffusion tensor image, we start by computing a set a of diffusion-weighted images (one image for each corresponding gradient direction). The diffusion-weighted signal is obtained according to a multitensor model with a cylindrical symmetry constraint. The model was inspired by the hindered extra-axonal compartment of the CHARMED model proposed in Assaf and Basser [2005]; Assaf et al. [2004], which gives rise to an effective diffusion tensor and primarily explains the Gaussian signal attenuation observed at low b values. Given that the average eigenvalues of the diffusion tensors reconstructed in regions of white matter, grey matter, or cerebrospinal fluid have been measured and reported (Bhagat and Beaulieu [2004]; Partridge et al. [2004]; Pierpaoli et al. [1996]), this restriction allows us to realistically model the diffusion properties of different tissues as well as partial-volume effects in the diffusion-weighted images.

Let us denote the pulse separation by Δ and set

$$\mathbf{q} = \frac{\gamma \mathbf{g} \delta}{2\pi} \, .$$

Here γ is the proton gyromagnetic ratio, $\mathbf{g}$ is the vector whose magnitude is the

strength of the applied diffusion gradient and whose direction is along the axis of the applied diffusion gradient, and δ is the width of the diffusion pulse gradient. In this case, the net signal attenuation is given by

$$E(\mathbf{q}, \Delta) = \sum_{i=1}^{M} f_h^i \cdot E_h^i(\mathbf{q}, \Delta) \tag{2.1}$$

where the f_h^i are the T_2 weighted volume fractions of the hindered compartments and $E_h^i(\mathbf{q}, \Delta)$ is the normalized MR echo signal from the i-th hindered compartment in a voxel. We assume a cylindrically symmetric tensor model ($\lambda_1 \neq \lambda_2 = \lambda_3$) and denote the diffusion coefficients parallel and perpendicular to the axon's fiber by $\lambda_\parallel$ and $\lambda_\perp$, respectively. In a similar manner, $\mathbf{q}$ may be written as $\mathbf{q} = \mathbf{q}_\parallel + \mathbf{q}_\perp$. For details on the computation of $\mathbf{q}_\parallel$ and $\mathbf{q}_\perp$ see [Assaf et al., 2004, Appendix B]. Then $E_h^i(\mathbf{q}, \Delta)$ is given by

$$E_h^i(\mathbf{q}, \Delta) = e^{-4\pi^2(\Delta-(\delta/3))|q_\parallel|^2\lambda_\parallel} + e^{-4\pi^2(\Delta-(\delta/3))|q_\perp|^2\lambda_\perp} .$$

It is known (Gudbjartsson and Patz [1995]) that noise in magnitude magnetic resonance data is Rician distributed. As suggested in Hahn et al. [2006], such noise distribution may be simulated in the image by computing $|E(\mathbf{q}, \Delta) + \tilde{N}(0, \sigma^2)|$, where $\tilde{N}(0, \sigma^2)$ is a Gaussian-distributed complex variable with mean 0 and variance σ^2. For completeness, let us mention that the noise variance may be computed, as illustrated in Parker and Gullberg [1990], by

$$\sigma^2 = K \frac{N_x \, N_y \, \langle V^2 \rangle}{N_{av} \, \mathrm{FOV}_x^2 \, \mathrm{FOV}_y^2 \, \Delta_t}$$

where N_x,N_y are the number of samples in x and y direction, $\langle V^2 \rangle$ is the thermal noise power, N_{av} is the number of averages, FOV_x, FOV_y are the fields of view in x and y directions, Δ_t is the sampling interval, and K is a scanner-dependent factor. We refer readers interested in the exact relation between the variance of the Gaussian signal in the two quadrature channels and the variance of the Rician-distributed magnitude MR signal to Koay and Basser [2006].

We model partial-volume effects by sampling the image at $0.1 \times 0.1 \times 0.1$ mm^3

and then linearly resampling it at 1 mm^3. Using standard fitting procedures, we use the diffusion-weighted images to compute the tensor-valued image.

2.3.1.1 The Torus-Shaped Phantom

In our first experiments, the fiber bundle model is given by the segment of a torus of radius R and cross section of radius r. If the center of a voxel lies inside the torus, we set $\lambda_{\parallel}$ and $\lambda_{\perp}$ to values that are compatible with eigenvalues of tensors encountered in white matter, based on reports from Bhagat and Beaulieu [2004]; Pierpaoli et al. [1996]. The direction of a tensor's main eigenvector is set perpendicular to the line segment connecting the voxel to the center of the torus. For the background, we use isotropic tensors. The seed region of interest (ROI) used for fiber-tracking is set as a circle with radius r located on a plane perpendicular to the fiber bundle. The location of the seed ROI and some example diffusion-weighted images are shown in Fig. 2.1.

(a) (b) (c)

Figure 2.1: (a): b_0 image of the torus-shaped fiber bundle. The seed ROI used for fiber-tracking is superimposed in yellow. (b): Diffusion-weighted image of the torus-shaped fiber bundle, gradient pointing in x direction. (c): Diffusion-weighted image of the torus-shaped fiber bundle, gradient pointing in xy direction.

2.3.2 Measuring Fiber-Tracking Error

In this section, we start by briefly summarizing the fiber-tracking algorithm used throughout this work. Thereafter, we introduce a measure for the fiber-tracking error.

2.3.2.1 The Fiber-Tracking Algorithm

For fiber-tracking, we use the advection-diffusion based algorithm presented in Schlüter et al. [2005]. For a given tracking position r^t and step length Δs, the next position r^{t+1} is given by

$$r^{t+1} = r^t + \mathbf{d}^t\,\Delta s + \frac{1}{2}\mathbf{k}^t\,\Delta s^2\,.$$

$\mathbf{d}^t$ is computed by using the previous tracking direction $\mathbf{d}^{t-1}$

$$\mathbf{d}' = \left[\alpha\mathbf{v}\mathbf{v}^t + (1-\alpha)\frac{\mathbf{D}}{\lambda_{\max}}\right]\mathbf{d}^{t-1}\,, \qquad \mathbf{d}^t = \frac{\mathbf{d}'}{\|\mathbf{d}'\|}$$

Here, $\mathbf{D}$ is the tensor at $\mathbf{r}^t$ with largest eigenvalue $\lambda_{\max}$ and corresponding eigenvector $\mathbf{v}$; the weight $\alpha \in [0,1]$ interpolates between streamline ($\alpha = 1$) and deflection ($\alpha = 0$) based tracking. Further, $\mathbf{k}^t$ is a curvature term given by

$$\mathbf{k}^t = \frac{\mathbf{d}^t - \mathbf{d}^{t-1}}{\Delta s}$$

which helps improve fiber-tracking accuracy. Although we employ this specific fiber-tracking algorithm (with $\alpha = 0.7$) in this work, the presented analysis and related conclusions can be generalized to other streamline tractography algorithms.

2.3.2.2 The Safety Radius

To evaluate our fiber-tracking results, we determine a safety radius r_s. Given a cross section of the tracked fiber bundle, the safety radius is defined as the minimal radius that is needed so that if a circle with radius r_s were placed around each fiber tracked inside the bundle, the aggregate of these circles would form a topological cover of the cross section of the modeled fiber bundle. In order to find r_s, we first compute the Voronoi diagram of the points inside the cross section of the fiber bundle; r_s is then given by the maximal distance between one such point and the borders of the corresponding cell (see Fig. 2.2). From a clinical point of view, the safety radius may be used to compare different tractography algorithms and also to verify the validity of the diffusion model fitted to the diffusion-weighted data. Moreover, the safety radius indicates to which extent a fiber-tracking algorithm underestimates the true size of a fiber bundle.

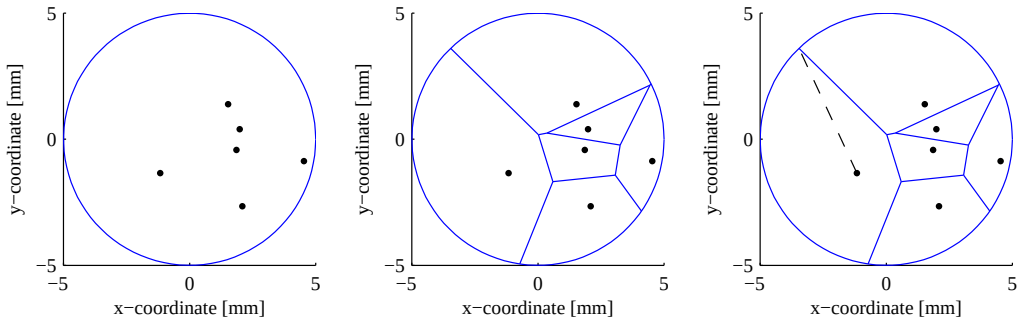

Figure 2.2: (a): Cross section of the modeled fiber bundle. The location of the tracked fibers is shown as dots. (b): The Voronoi diagram of the tracked fibers inside the cross section of the modeled fiber bundle. (c): The computed safety radius r_s corresponds to the dashed line. The set of circles with radius r_s centered at the tracked fibers covers the cross section of the modeled fiber bundle.

2.3.3 Experimental Results Obtained by Means of the Torus-Shaped Phantom

We would now like to analyze how the safety radius changes with respect to both the parameters used to create the torus-shaped phantom and the parameters used for fiber-tracking. As defaults, we use the parameters listed in Table 2.1. After we have tracked the fiber bundle, we compute the safety radius every 10 mm of arc length, advancing counterclockwise from 180° until 200 mm of arc length. We then take the maximum safety radius found.

We perform five separate experiments in which we independently vary one of the phantom or fiber-tracking parameters as specified in Table 2.2. For each set of parameters, we add noise to the image, perform the tracking, and compute the safety radius 100 times. Figs. 2.3(a) to 2.3(e) show boxplots for the safety radius vs. the variable changing in each experiment.

	Default value
radius of the torus	80 mm
diameter of the cross section	10 mm
T_2 for the bundle	70 ms
T_2 for the background	83 ms
$\lambda_{\parallel}$ for the bundle	$11.3 \cdot 10^{-4}$ mm^2/s
$\lambda_{\perp}$ for the bundle	$5.15 \cdot 10^{-4}$ mm^2/s
$\lambda_{\parallel}$ for the background	$9.9 \cdot 10^{-4}$ mm^2/s
$\lambda_{\perp}$ for the background	$9.9 \cdot 10^{-4}$ mm^2/s
voxel size	$1 \times 1 \times 1$ mm^3
number of gradients	6
gradient strength	20 mT/m
pulse separation	40 ms
pulse width	35 ms
noise standard deviation	1.5
number of seed points	50
fiber-tracking step length	1 mm

Table 2.1: Default parameters for the torus-shaped phantom.

	start value	**step**	**end value**	
diameter of the cross section	5	1	15	mm
$\lambda_{\perp}$ for the bundle	8.55	0.2	11.35	$\cdot 10^{-4}$ mm^2/s
noise standard deviation	0	0.2	6	
number of seed points	10	20	230	
fiber-tracking step length	0.2, then 1	1	20	mm

Table 2.2: Parameter variation for the different experiments.

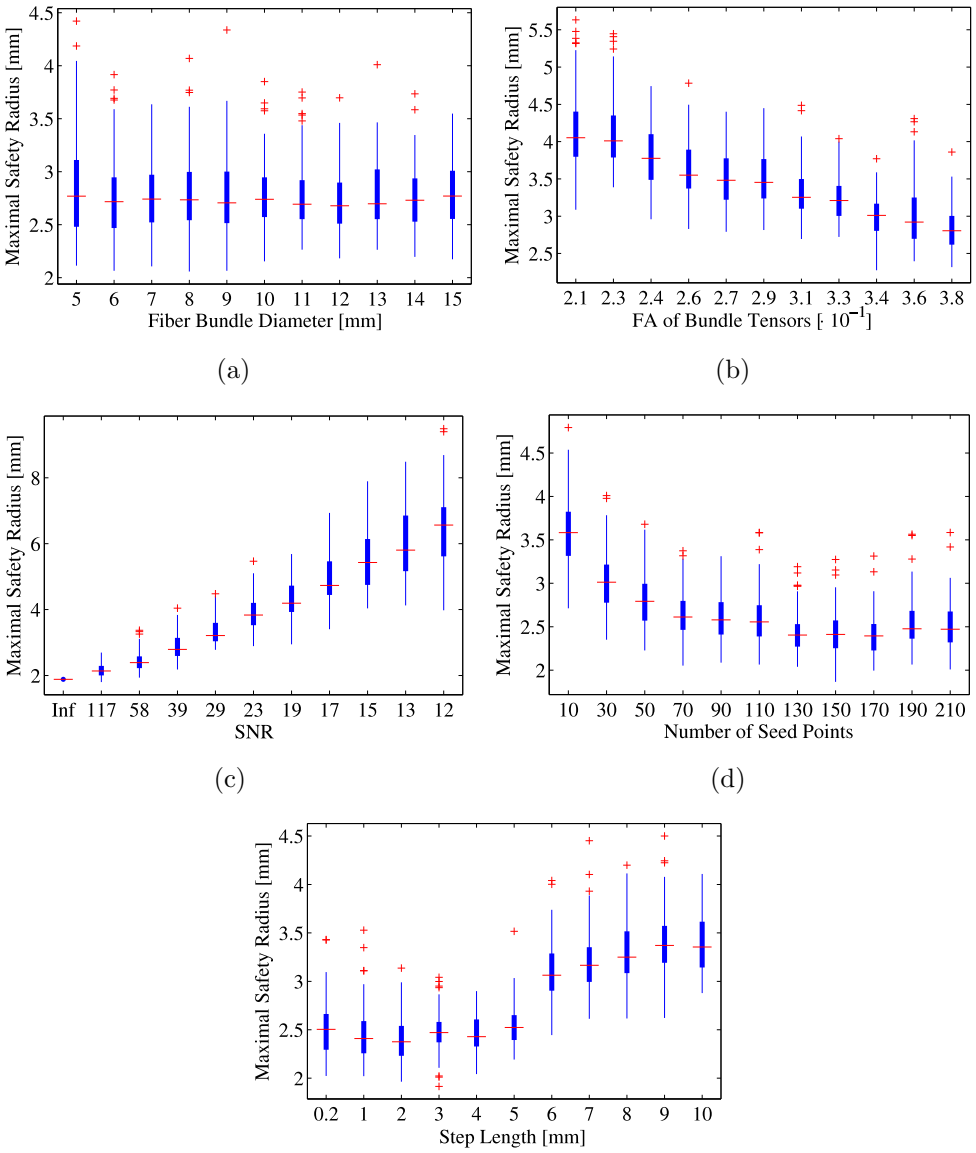

Figure 2.3: Torus-shaped phantom. (a): safety radius vs. diameter of the cross section of the torus. (b): safety radius vs. fractional anisotropy of the modeled bundle. In particular, this affects the main diffusion directions estimated at the border of the bundle. (c): safety radius vs. signal-to-noise ratio (SNR). The SNR is defined as the T_2 for the bundle divided by the standard deviation of the noise. (d): safety radius vs. number of seed points. (e): safety radius vs. fiber-tracking step length. The other parameters used for these analyses are listed in Table 2.1.

In order to analyze the spatial distribution of the tracked fibers, we again sample the modeled fiber bundle every 10 mm of arc length. We partition the cross section into six semi-annuli of equal area as shown in Fig. 2.4(a). At each cross section, we count how many fibers lie in each part. Fig. 2.4(b) shows the averaged number of fibers in the different plane parts for all experiments in which we vary the standard deviation of the thermal noise.

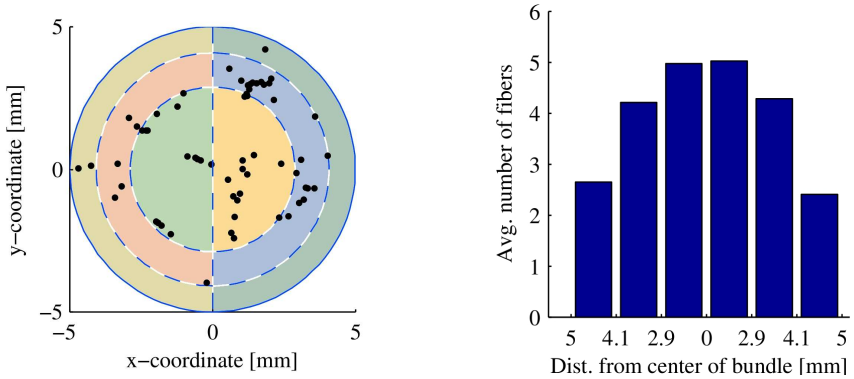

(a) (b)

Figure 2.4: (a): Partitioned cross section of the tracked fiber bundle. Fibers with positive x-coordinate are on the interior of the circular fiber path. (b): Overall averaged number of fibers in the different plane parts. Bars on the left correspond to fibers on the exterior of the circular fiber path and bars on the right correspond to fibers on the interior.

2.4 Generating and Analyzing Fiber-Tracking Error on a Realistic DTI Phantom of Neural Fiber Bundles

In this section, we generate realistic phantoms of the corticospinal tract and the arcuate fasciculus. We attempt to simulate both the smooth transition between the actual white matter (WM) pathway and the surrounding tissue and the partial-volume effects caused by the simultaneous presence of white matter, grey matter, and cerebrospinal fluid in one voxel. Similarly to Section 2.3.3, we systematically vary the standard deviation of the noise and fiber-tracking parameters

in order to make a quantitative analysis of the fiber-tracking error.

2.4.1 Generating the BrainWeb-Based Phantom

To create the diffusion-weighted images, we build upon the BrainWeb project (Collins et al. [1998]) at McGill University. The BrainWeb dataset was created from 27 low-noise scans (T_1 weighted gradient echo acquisitions with TR/TE/FA = 18ms/10ms/30°) of the same individual coregistered in stereotaxic space where they were subsampled and the intensities were averaged (Holmes et al. [1998]). By means of a modified minimum-distance classifier, ten volumetric datasets that define the spatial distribution for different tissues were created. In these images, the voxel intensity is proportional to the fraction of tissue within the voxel. In our phantom, we make use of the white matter, grey matter, and cerebrospinal fluid volumes; an example slice of each volume is shown in Figure 2.5. The volumes are defined at a 1 mm isotropic voxel grid with dimensions $181 \times 217 \times 181$ (X×Y×Z).

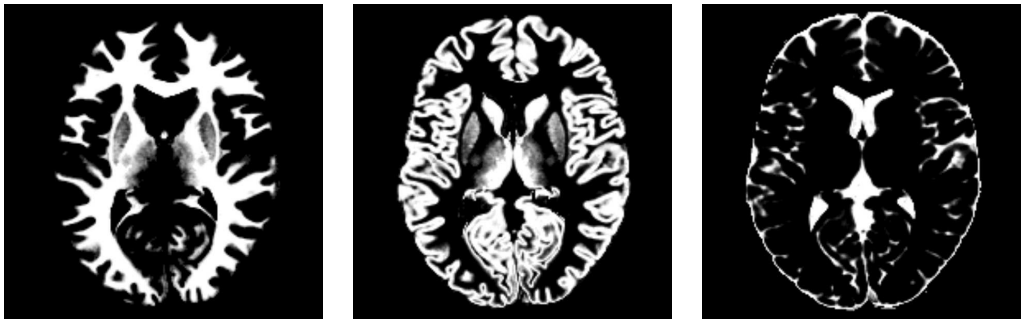

(a) (b) (c)

Figure 2.5: (a): An example slice of the white matter volume. (b): The grey matter volume. (c): The cerebrospinal fluid volume.

We proceed using the same general framework as presented in Section 2.3.1. To each fraction of tissue in a voxel, we assign a main diffusion direction and the eigenvalues of the cylindrically symmetric diffusion tensor. The resulting signal attenuation is then computed according to Equation 2.1. For the above tissues, the average eigenvalues of the diffusion tensors have been measured and reported in Bhagat and Beaulieu [2004]; Partridge et al. [2004]; Pierpaoli et al. [1996], from

which we derive the eigenvalues for our model, reported in Table 2.3. Example

	T_2 (ms)	$\lambda_{\parallel}$ (10^{-4}mm^2/s)	$\lambda_{\perp}$ (10^{-4}mm^2/s)
White Matter	70	11.30±0.7	5.15±0.3
Grey Matter	83	9.90±0.4	7.05±0.3
Cerebrospinal Fluid	329	36.00±2.3	30.36±1.8

Table 2.3: T_2 values and tensor eigenvalues used in the BrainWeb-based phantom for the different tissues.

slices of a modeled $b0$ image, with and without added image noise, are shown in Figs. 2.6(a) and 2.6(b). As far as the main diffusion direction is concerned, we assign a random, uniformly distributed direction to each tissue portion present in a voxel, unless there is one or more modeled fiber bundles going through it. In this case, the main diffusion direction depends on the modeled fiber bundles. When multiple fiber bundles are present in one voxel, we assume that the white matter fraction is divided into portions of equal volume among the different bundles. We describe our method for modeling fiber bundles in the following Section 2.4.2.

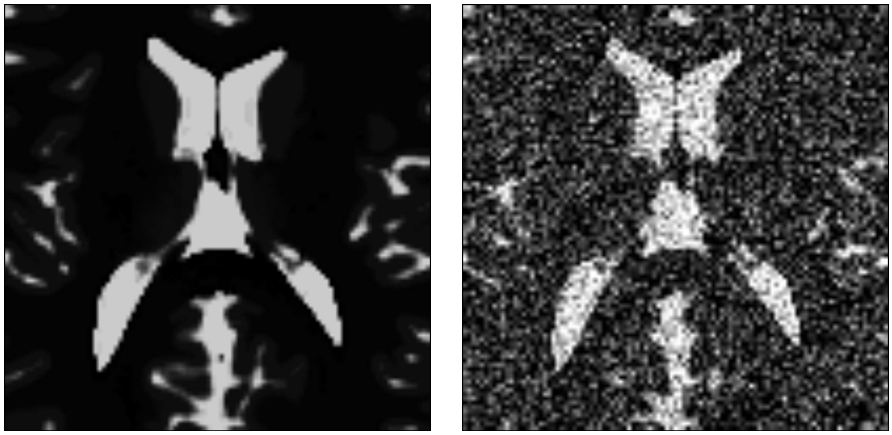

(a) (b)

Figure 2.6: (a): Example slice of a modeled $b0$ image. (b): Complex Gaussian noise with σ=80 added to the image.

2.4.2 Modeling White Matter Pathways

To model a white matter pathway, we make use of the hand-segmented white matter parcellation map provided by the ICBM DTI-81 Atlas. The parcellation map is affinely registered to the BrainWeb volume masks and determines the spatial extent of a fiber bundle. In order to define the diffusion properties of the bundle, we start by computing its centerline. After determining a tuple of n control points $\{P_i\}_{i=1,\dots,n}$ in $\mathbb{R}^3$ along the centerline, these points are interpolated by means of cubic splines. For simplicity, we choose Catmull-Rom splines, which are defined by two points P_i, P_{i+1} and two tangent vectors T_i, T_{i+1}. The tangent vectors are computed by

$$T_j = \frac{1}{2} \cdot (T_{j+1} - T_{j-1}) \,.$$

Thereafter, the evolution of the parametric curve $s_i(t) = (x_i(t), y_i(t), z_i(t))^T$ with $t \in [0,1]$ and connecting P_i and P_{i+1} is given, for example, in the x-dimension by

$$x_i(t) = \begin{pmatrix} t^3 & t^2 & t & 1 \end{pmatrix} \cdot \begin{pmatrix} 2 & -2 & 1 & 1 \\ -3 & 3 & -2 & -1 \\ 0 & 0 & 1 & 0 \\ 1 & 0 & 0 & 0 \end{pmatrix} \cdot \begin{pmatrix} P_{i_x} \\ P_{(i+1)_x} \\ T_{i_x} \\ T_{(i+1)_x} \end{pmatrix}$$

and similarly in the other dimensions. Concatenating the different splines $\{s_i\}$ results in a differential 3D curve s connecting P_1 to P_n. See Fig. 2.7(a) for an example curve.

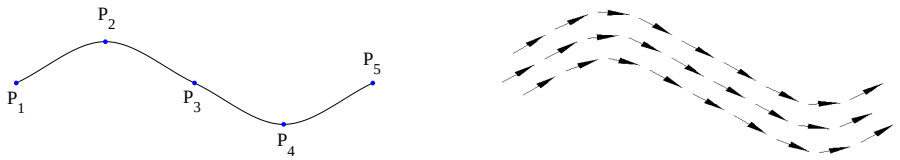

(a) (b)

Figure 2.7: (a): Example curve interpolating the control points $\{P_i\}$ and forming the backbone of the modeled fiber bundle. (b): Schematic representation of the main diffusion directions of the tensors within a tubular fiber bundle.

Consider a voxel with coordinates $V = (x_v, y_v, z_v)^T$ and a white matter frac-

tion belonging to the bundle to be modeled. We compute the minimal distance between V and the bundle backbone s and the minimal distance between V and the border of the bundle. Let us denote these two distances by d_s and d_b, respectively. The distance to the border is easily computed by means of a Euclidean distance transform (see Rosenfeld and J. [1966]; Russ [1995]); details on the how to compute the distance to the centerline are given in section 2.4.2.1. We assign a normalized distance value d_m to V, computed as

$$d_m = \frac{d_b}{d_b + d_s} \tag{2.2}$$

A schematic example of a normalized distance map is given in Fig. 2.8(a). The main diffusion direction e_1 at V is then determined along the isosurface of the normalized distance map as follows: Denote the point on the centerline closest to V by $s(t^*)$ with tangent $s'(t^*)$, and the gradient of the normalized distance map at V by g, then

$$e_1 = s'(t^*) - (s'(t^*) \cdot g)\, g\,. \tag{2.3}$$

See Fig. 2.8(b) for an example of resulting directions.

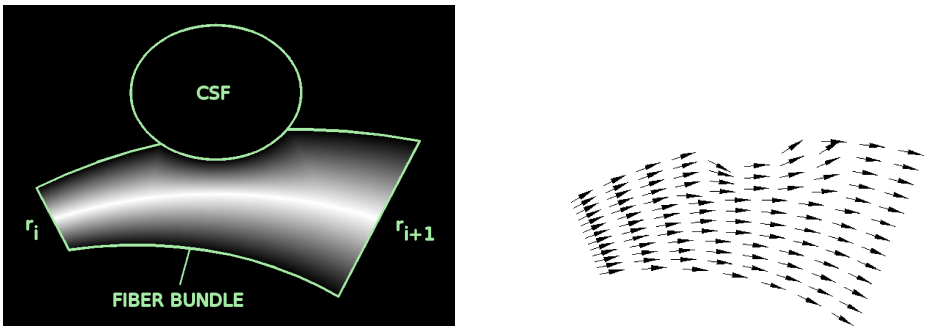

(a) (b)

Figure 2.8: (a): Schematic representation of the normalized distance function when going from a control point P_i with radius r_i to a control point P_{i+1} with radius r_{i+1}. (b): The corresponding main diffusion directions.

2.4.2.1 Minimizing the Point to Spline Distance

This section illustrates how we compute the shortest (squared) distance $D_i(t)$ between V and a spline curve s_i, given by

$$D_i(t) = (x_i(t) - x_v)^2 + (y_i(t) - y_v)^2 + (z_i(t) - z_v)^2 \,. \tag{2.4}$$

The minimization problem gives rise to quintic equations which generally have no analytic solutions. We therefore have to resort to numerical methods. We use the algorithm from Wang et al. [2002]. This algorithm combines quadratic minimization and Newton's method to quickly and accurately find a solution t^*. Quadratic minimization is an iterative algorithm which uses three initial estimates of t^*, which we denote by t_1, t_2, t_3, to fit a parabola to the points $(t_1, D(t_1))$, $(t_2, D(t_2))$, $(t_3, D(t_3))$, the minimum of which has t-coordinate

$$t_{\min} = \frac{1}{2} \cdot \frac{p_{23}D(t_1) + p_{31}D(t_2) + p_{12}D(t_3)}{q_{23}D(t_1) + q_{31}D(t_2) + q_{12}D(t_3)}$$

where $q_{ij} = t_i - t_j$ and $p_{ij} = t_i^2 - t_j^2$. For the next iteration, we use the three coordinates among $t_1, t_2, t_3, t_{\min}$ which correspond to the smallest $D(t)$ values. Although quadratic minimization converges relatively slowly (superlinearly given a sufficiently good set of initial estimates, Luenberger [1984]), it is good at refining coarse estimates. These properties are complemented by Newton's algorithm, which makes use of the iteration formula

$$t^{*,m+1} = t^{*,m} - \frac{D'(t^{*,m})}{D''(t^{*,m})}, \qquad m = 0, 1, 2, \ldots$$

and, for a zero of multiplicity 1, converges quickly (quadratically, Deuflhard [2004]) to the optimal value given a good initial guess. To compute the minimum distance between a voxel V and a spline s_i in our phantom, we iterate quadratic minimization three times with initial estimates of $t_1 = 0$, $t_2 = 0.5$, $t_3 = 1$, the result of which is used as an initial guess for 10 iterations of Newton's algorithm. If this approach converges towards values outside the range $t \in [0, 1]$, we appropriately set t^* to either 0 or 1. At present, we compute the t value, giving the minimum distance between V and s by choosing the t^* value over all $\{s_i\}$

which corresponds to the smallest $D_i(t^*)$. This may be optimized by considering that neighboring voxels will have a similar minimal distance to s.

2.4.2.2 Mapping the Distance Function to Alternative Kernels

In order to generate our BrainWeb-based phantoms, we model partial-voluming effects by subsampling the image as described in Section 2.3.1. A further possible extension has been suggested in Leemans et al. [2005]: Instead of modeling fiber bundles to have constant diffusion properties over their cross sections, one could map the distance d_c between a voxel V and the backbone of a bundle according to various monotonic decreasing functions (for positive x-values). This way, the further away a voxel V is from the backbone, the less influence that fiber bundle will have on the tensor at V. Suggested functions include a Gaussian with mean 0 and standard deviation σ

$$k_g(d) := e^{-d^2/2\sigma^2}$$

or the saturated function

$$k_s(d) := \frac{\text{erf}\left(\frac{\text{w}+2d}{2\sqrt{2}\sigma}\right) + \text{erf}\left(\frac{\text{w}-2d}{2\sqrt{2}\sigma}\right)}{2\text{erf}\left(\frac{\text{w}}{2\sqrt{2}\sigma}\right)}$$

where erf() is the error function and $\text{w} \in \mathbb{R}^+$ controls the width of the bundle. For details on these kernels, we refer the interested reader to the aforementioned paper. According to experimental results presented in Leemans et al. [2005], using a Gaussian or the saturated function to model fiber bundles yields improved similarity between the phantom and real data. However, to the best of our knowledge, it is not yet completely clear why this is the case. Also, from a histological point of view, we do not know whether the density of fibers and directional homogeneity inside specific neural tracts decrease when moving from the center of the fiber bundle to its border. For the time being, we model fiber bundles in our numerical experiments to have constant diffusion properties.

2.4.3 Experimental Results Obtained by Means of the BrainWeb-Based Phantom

By using the white matter parcellation map provided by the ICBM DTI-81 Atlas, we construct phantoms of the corticospinal tract (between the posterior limb of the internal capsule and the brainstem) and of the arcuate fasciculus. In a manner similar to Section 2.3.3, we reconstruct the modeled tract via fiber-tracking and analyze the accuracy of the results. To track the modeled bundles, we use whole-brain fiber-tracking (Conturo et al. [1999]) and select the fibers that go through regions of interest at the beginning and end of the bundles. The whole-brain tracking approach is chosen for its superior reconstruction capabilities, see for example Klein et al. [2010b]. The tracked bundles are shown in Fig. 2.9(b) and 2.9(c).

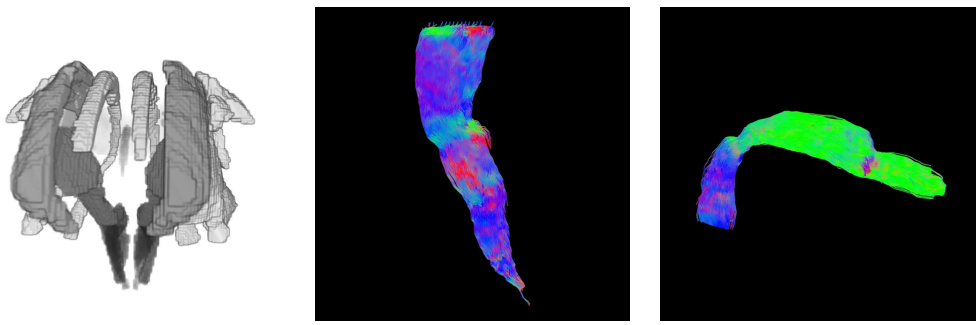

(a) (b) (c)

Figure 2.9: (a): White matter parcellation map provided by the ICBM DTI-81 Atlas. The map determines the spatial extent of the modeled fiber bundles. (b): Streamline tracking of the modeled portion of the right corticospinal tract. (c): Streamline tracking of the modeled right arcuate fasciculus. These bundles will later be used as an initial mask by our fuzzy segmentation algorithm.

There are two fundamental differences between the torus-shaped phantom and the BrainWeb-based phantoms: In the former, the width of the fiber bundle is constant, and we know the exact geometry of its cross section. Because this is not the case in the latter phantom, we need to adapt our measurement of the error of tracked fibers via the safety radius. First, given the variable width of the fiber bundle, we restrict ourselves to an error analysis on one slice, and do not measure the error multiple times along the fiber bundle. For the corticospinal

tract, we analyze a slice at the height of the internal capsule, whereas for the arcuate fasciculus, we analyze a slice parallel to the xz plane which cuts the bundle approximately in the middle. To compute the safety radius, we start by determining the set of points (with a sampling interval of 0.1 mm) that lie on the considered slice on the inside of the fiber bundle and lie in voxels with a grey matter fraction greater than zero. Next, for a tracked fiber bundle, we determine the points with the same characteristics that additionally lie on the tracked fibers. An example cross section and its intersection with the tracked fibers are illustrated in Fig. 2.10(a). The safety radius for this discrete case is then given by the maximum Euclidean distance between a sampled point of the cross section and a point of the tracked fibers, see Fig. 2.10(b).

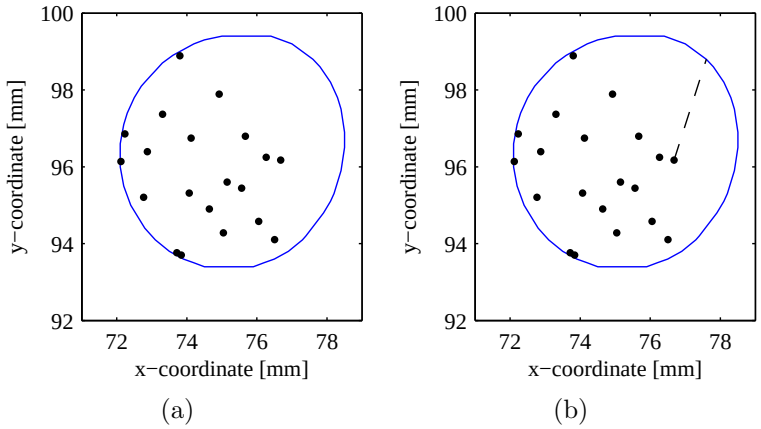

Figure 2.10: (a): Example cross section of a modeled tract. The locations of the tracked fibers are shown as dots. (b): The computed safety radius r_s corresponds to the dashed line. The set of circles with radius r_s centered at the tracked fibers covers the cross section of the modeled fiber bundle.

We perform three separate experiments in which we independently vary the standard deviation of the noise, the number of seed points, and the fiber tracking step length for the two BrainWeb-based phantoms. As defaults, we use the parameters listed in Tables 2.3 and 2.4. Note that in these phantoms, we allow for small variations in the eigenvalues of the tensors which correspond to the different tissues. The other parameters are varied according to Table 2.5. As before, for each set of parameters, we add noise to the image, perform the tracking, and compute of the safety radius 100 times. Figs. 2.11(a) to 2.11(f) show boxplots

	Default value
voxel size	$1\times1\times1$ mm^3
number of gradients	30
gradient strength	20 mT/m
pulse separation	40 ms
pulse width	35 ms
noise standard deviation	3
reciprocal of seed point density	8 mm^3/seed
fiber-tracking step length	1 mm

Table 2.4: Default parameters for the BrainWeb-based phantoms.

	start value	**step**	**end value**	
noise standard deviation	0.5	0.5	5.5	
reciprocal of seed point density	0.5,1, then 2	2	18	mm^3/seed
fiber-tracking step length	0.2, then 1	1	10	mm

Table 2.5: Parameter variation for the different experiments with the BrainWeb-based phantoms.

for the safety radius vs. the variable changing in each experiment, both for the modeled corticospinal tract and arcuate fasciculus. Fig. 2.12 gives an overview of the safety radius computed on different slices along the corticospinal tract.

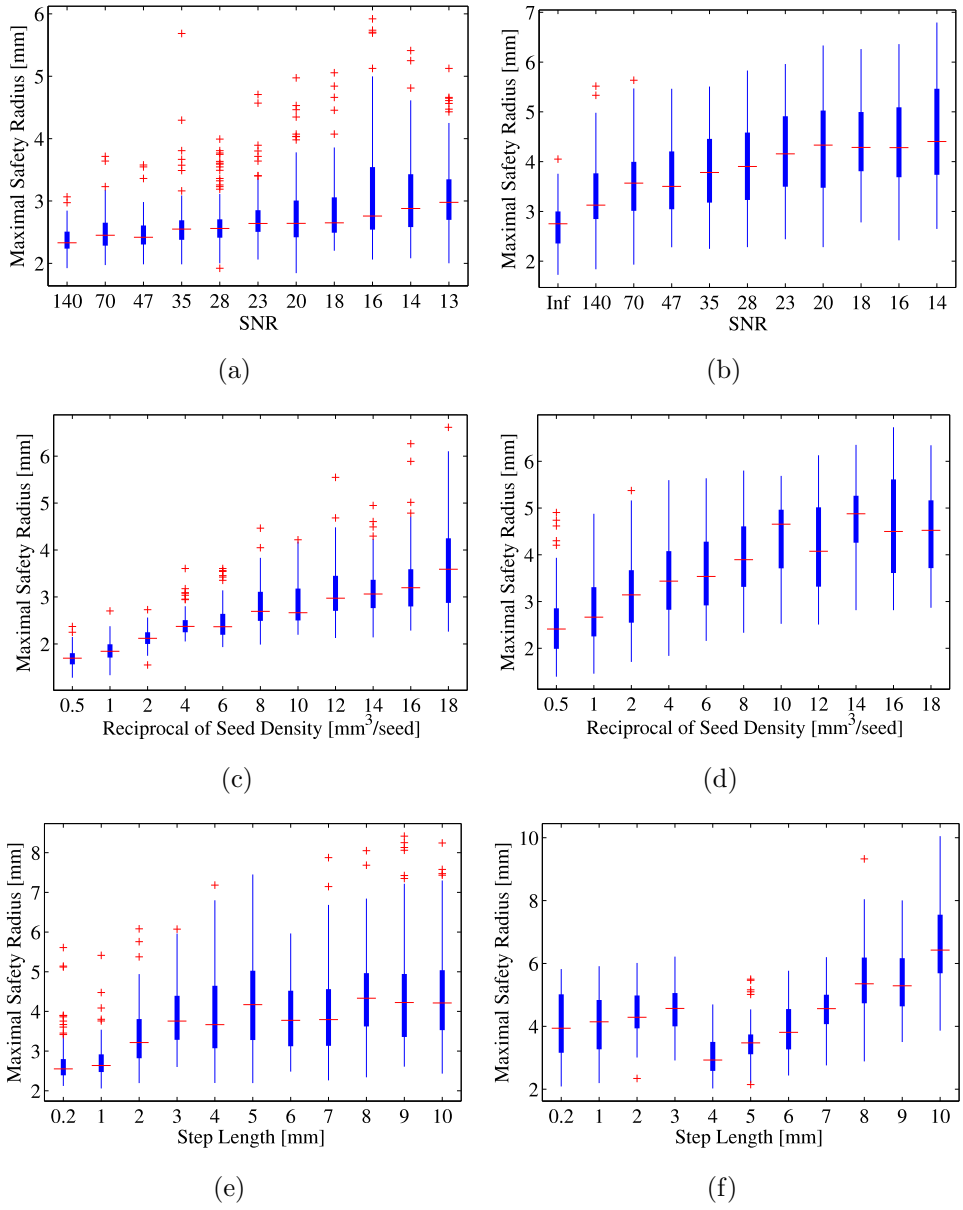

Figure 2.11: BrainWeb-based phantoms. Left column: corticospinal tract results. Right column: arcuate fasciculus results. (a),(b): safety radius vs. signal to noise ratio. (c),(d): safety radius vs. reciprocal of seed point density. (e),(f): safety radius vs. fiber-tracking step length. The other parameters used for these analyses are listed in Table 2.4.

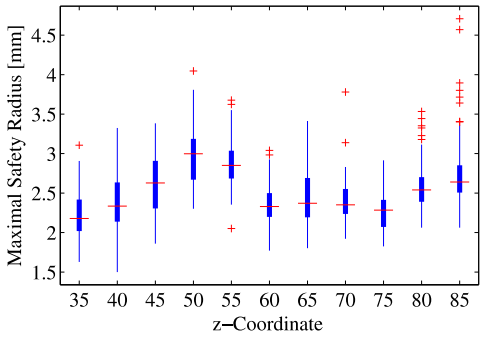

Figure 2.12: Based on the modeled corticospinal tract, we compute the safety radius on several slices with different z-coordinates.

2.5 Estimating the Extent of Fiber Bundles

In Sections 2.3 and 2.4 we generated a multitude of different DT software phantoms and analyzed the tracking error. In order to improve the accuracy with which the extent of fiber bundles is determined, we now suggest an efficient algorithm to generate a fuzzy segmentation of diffusion tensor data. We employ the tracked fibers as an initial segmentation and successively analyze the directions of the principal eigenvectors and the respective covariance matrices of tensors close to the tracked fibers. The resulting data will be visualized by means of confidence hulls around the tracked fibers. We test our algorithm both on the generated DTI phantoms and on a real diffusion tensor magnetic resonance scan of a patient.

2.5.1 Review of Computing the Covariance Matrix of the Main Diffusion Direction

Given a reference signal S_0, diffusion-encoded unitary gradient vectors $\mathbf{g}_i$ with $i = 1, \ldots, n$, measured diffusion-weighted signals with noise s_i, and a design matrix

$$W = \begin{pmatrix} 1 & -b_1 g_{1x}^2 & -b_1 g_{1y}^2 & -b_1 g_{1z}^2 & -b_1 g_{1x} g_{1y} & -b_1 g_{1y} g_{1z} & -b_1 g_{1x} g_{1z} \\ \vdots & \vdots & \vdots & \vdots & \vdots & \vdots & \vdots \\ 1 & -b_1 g_{nx}^2 & -b_1 g_{ny}^2 & -b_1 g_{nz}^2 & -b_1 g_{nx} g_{ny} & -b_1 g_{ny} g_{nz} & -b_1 g_{nx} g_{nz} \end{pmatrix}$$

we start by estimating the diffusion tensor in each voxel, as suggested in Koay et al. [2006], by minimizing the constrained nonlinear least-squares objective function

$$f_{\mathrm{CNLS}}(\gamma(\rho)) = \frac{1}{2}\sum_{i=1}^{n}\left(s_i - \exp\left[\sum_{j=1}^{7} W_{ij}\gamma_i(\rho)\right]\right)^2 . \tag{2.5}$$

In Equation 2.5, $\gamma(\rho)$ is the mapping between the entries of the upper diagonal matrix

$$\mathbf{U}(\rho) = \begin{pmatrix} \rho_2 & \rho_5 & \rho_7 \\ 0 & \rho_3 & \rho_6 \\ 0 & 0 & \rho_4 \end{pmatrix}$$

which gives the Cholesky decomposition of the diffusion tensor $\mathbf{D} = \mathbf{U}^T\mathbf{U}$, and the parameter vector

$$\gamma = [\ln(S_0), \mathbf{D}_{xx}, \mathbf{D}_{yy}, \mathbf{D}_{zz}, \mathbf{D}_{xy}, \mathbf{D}_{yz}, \mathbf{D}_{xz}]\,.$$

$\gamma(\rho)$ is explicitly given by

$$\gamma(\rho) = [\rho_1, \rho_2^2, \rho_3^2 + \rho_5^2, \rho_4^2 + \rho_6^2 + \rho_7^2, \rho_2\rho_5, \rho_3\rho_6 + \rho_5\rho_7, \rho_2\rho_7]$$

with $\rho_1 = \ln(S_0)$. Minimizing f_{CNLS} with respect to $\gamma(\rho)$ ensures the positive definiteness of the estimated tensor $\mathbf{D}$. Specifically, the minimizing vector is found via the modified full Newton's algorithm proposed in [Koay et al., 2006, Appendix D], where it has been shown to offer lower error trace estimates than weighted or unweighted linear least-squares approaches. For a minimizer $\hat{\gamma}$ of Equation 2.5, $\sigma^2_{\mathrm{DW}} := 2f_{\mathrm{CNLS}}(\hat{\gamma}(\rho))/(n-7)$ gives an unbiased estimate of the variance of the diffusion-weighted signal. After defining $\mathbf{S}$ and $\hat{\mathbf{S}}$ as the diagonal matrices whose diagonal elements are the observed and estimated diffusion-weighted signals, respectively, i.e.,

$$\mathbf{S} = \begin{pmatrix} s_1 & & \\ & \ddots & \\ & & s_n \end{pmatrix}, \quad \hat{\mathbf{S}} = \begin{pmatrix} \hat{s}_1 & & \\ & \ddots & \\ & & \hat{s}_n \end{pmatrix}$$

and $\mathbf{R} = \mathbf{S} - \hat{\mathbf{S}}$, the covariance matrix of γ is given by

$$\mathbf{\Sigma}_\gamma = \sigma^2_{\mathrm{DW}}[\mathbf{W}^T(\hat{\mathbf{S}}^2 - \mathbf{R}\hat{\mathbf{S}})\mathbf{W}]^{-1}\,.$$

Let $\mathbf{q}_1, \mathbf{q}_2, \mathbf{q}_3$ be the eigenvectors of $\mathbf{D}$ corresponding to the eigenvalues $\lambda_1 \geq \lambda_2 \geq \lambda_3$. Using the notation introduced in Hext [1963], we write

$$\mathbf{a}(\mathbf{q_i}, \mathbf{q_j})^T \equiv [q_{ix}q_{jx}, q_{iy}q_{jy}, q_{iz}q_{jz}, q_{ix}q_{jy} + q_{iy}q_{jx}, q_{iy}q_{jz} + q_{iz}q_{jy}, q_{ix}q_{jz} + q_{iz}q_{jx}]^T$$

and additionally define $\mathbf{Q} = (\mathbf{q}_1, \mathbf{q}_2, \mathbf{q}_3)$, and

$$\mathbf{T}_1 = \begin{pmatrix} 0 & 0 & 0 & 0 & 0 & 0 & 0 \\ 0 & \frac{1}{(\lambda_1 - \lambda_2)}\mathbf{a}(\mathbf{q_2}, \mathbf{q_1})^T \\ 0 & \frac{1}{(\lambda_1 - \lambda_3)}\mathbf{a}(\mathbf{q_3}, \mathbf{q_1})^T \end{pmatrix}\,.$$

Finally, the covariance matrix of the major eigenvector is given by Koay et al. [2008]:

$$\mathbf{\Sigma}_{\mathbf{q_1}} = (\mathbf{Q}\mathbf{T}_1)\mathbf{\Sigma}_\gamma(\mathbf{Q}\mathbf{T}_1)^T\,.$$

2.5.2 A New Plausibility Measure for a Voxel to Be Part of the Tracked Bundle

Our algorithm for fuzzy DTI segmentation analyzes the voxels in the neighborhood of a tracked fiber. We denote the set of voxels through which a fiber goes by $\{V_i\}$; this set is considered to be certainly part of the tracked fiber bundle. The idea of our algorithm is that a neighboring voxel R is considered to be very likely part of the bundle if the main eigenvector of the tensor at R has, with little uncertainty, similar direction to the direction of a tensor at a voxel $V \in \{V_i\}$. If the angle between the directions of the main eigenvectors at R and V increases, or if there is high uncertainty in the direction of R or V due to noise or isotropic tensors, we consider R to be less likely part of the bundle. Let us denote the main diffusion directions at R and V by $\mathbf{q}_{1R}$ and $\mathbf{q}_{1V}$, with covariance matrices $\mathbf{\Sigma}_{\mathbf{q_{1R}}}$ and $\mathbf{\Sigma}_{\mathbf{q_{1V}}}$, respectively. Mathematically, we compute the distance between R and V as the cosine of the angle between the vectors $\mathbf{q}_{1R}^T$ and $\mathbf{q}_{1V}$, scaled by

the average variance of the average covariance matrix

$$c(R,V) = \frac{\mathbf{q}_{1R}^T \, \mathbf{q}_{1V}}{1 + \frac{1}{3} \cdot \text{trace}\left(\frac{\mathbf{\Sigma_{q_{1R}}} + \mathbf{\Sigma_{q_{1V}}}}{2}\right)}$$

which in the case of covariance matrices $\mathbf{\Sigma_{q_{1R}}}$ and $\mathbf{\Sigma_{q_{1V}}}$ close to 0 simply results in the cosine of the angle between the two diffusion directions. Finally, the plausibility of R being part of the tracked fibers at $\{V_i\}$ is computed as

$$d(R,\{V_i\}) = \max_i \left(1 - \frac{1}{\pi/2} \cdot \text{acos}\left(c(R,V_i)\right)\right)$$

which takes values in the interval $[0,1]$ with higher values corresponding to a higher plausibility of being part of the tracked fiber bundle. The plausibility at voxels $\{V_i\}$ is set to 1.

2.5.3 Experimental Results

We test our border-estimating algorithm on the tracked torus-shaped bundle from Section 2.3 and on the tracked corticospinal tract and arcuate fasciculus from Section 2.4, all generated using 30 different gradient directions. Color-codings of the plausibility of a voxel to belong the modeled corticospinal tract and arcuate fasciculus are shown in Figure 2.13. We also test the algorithm on a real magnetic resonance dataset of a tumor patient (diffusion-weighted images with TR/TE/FA = 10700 ms/84 ms/90°, voxel size is 1.80×1.80×1.98 mm, source: IEEE Visualization Contest 2010). A slice with the color-coded plausibility map is shown in Figure 2.14(a). The voxels with a plausibility above 0.85 are rendered as a semitransparent hull around the tracked fibers in Figure 2.14(b).

Next, using the developed DTI phantoms, we compare different algorithms to extend the tracked fibers to the true border of the fiber bundle. Specifically, we generate the torus and BrainWeb phantoms using 30 gradient directions and add noise with standard deviations of 2,4, and 6. Given the set of voxels $\{V_i\}$ through which the tracked fibers pass, we compare the following approaches which classify a neighboring voxel as part of the bundle if:

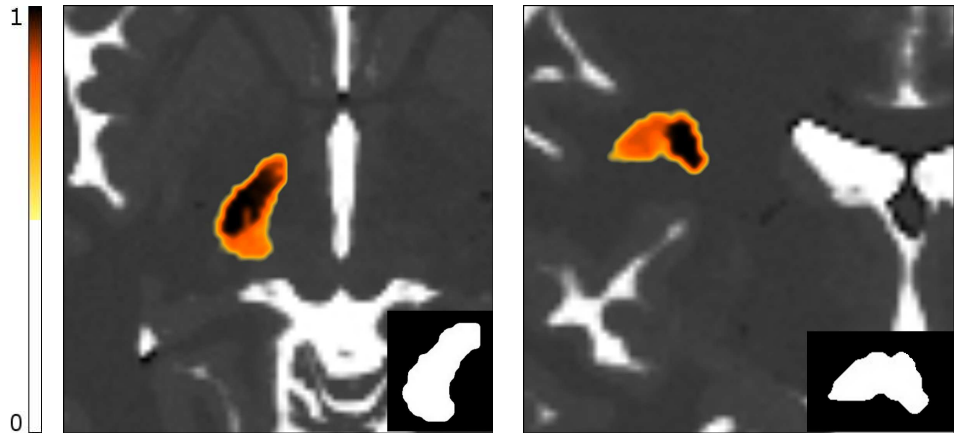

(a) (b)

Figure 2.13: Color coding of the plausibility of voxels in the proximity of tracked fibers (orange regions) of belonging to the tracked fiber bundle (black regions). The modeled ground truth is shown as a mask in the lower right corner. Voxels within 5 mm of the tracked fibers were analyzed. (a): modeled corticospinal tract, axial view. (b): modeled arcuate fasciculus, coronal view.

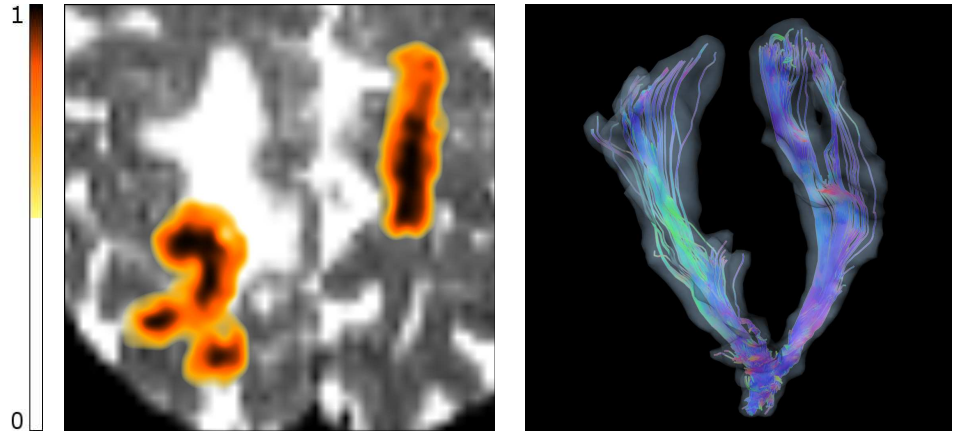

(a) (b)

Figure 2.14: (a): Color coding of the plausibility of voxels in proximity of tracked fibers (orange regions) to belong to the tracked corticospinal tract (black regions) of a patient with intra-cerebral metastasis (hyperintense regions). Voxels within 6 mm from the tracked fibers were analyzed. (b): Voxels with a high plausibility are rendered as a semitransparent hull around the tracked fibers.

- the plausibility, as described in Section 2.5.2, is above a certain threshold
- the plausibility, as described in Section 2.5.2 but without scaling by the

average variance (thus just comparing main diffusion directions), is above a certain threshold

- it is part of the morphological dilation of the set of voxels $\{V_i\}$
- it results from the min-cut-based approach presented in Bauer et al. [2010a]

The generated segmentation results are compared by computing the corresponding Dice similarity coefficient (DSC), introduced by Zou et al. [2004]. Results for the torus-shaped phantom are presented in Table 2.6, and results for the BrainWeb-based phantoms are presented in Tables 2.7 and 2.8.

Noise SD	**2.0**	**4.0**	**6.0**
original mask given by $\{V_i\}$	0.827	0.631	0.515
new plausibility approach	**0.957**	**0.931**	0.870
angle comparison	0.941	0.901	0.794
dilation	0.852	0.780	0.647
min-cut based	0.923	0.918	**0.918**

Table 2.6: Comparison of DSCs for the torus-shaped phantom.

Noise SD	**2.0**	**4.0**	**6.0**
original mask given by $\{V_i\}$	0.651	0.640	0.676
new plausibility approach	**0.832**	**0.805**	**0.776**
angle comparison	0.812	0.801	0.760
dilation	0.649	0.651	0.657
min-cut based	0.731	0.712	0.698

Table 2.7: Comparison of DSCs for the corticospinal tract phantom.

2.6 Discussion

In this work, we started by generating a diffusion tensor software phantom of a fiber bundle shaped as a torus segment. We set up a general framework to generate DTI phantoms and suggested using the so-called "safety radius" as a

Noise SD	**2.0**	**4.0**	**6.0**
original mask given by $\{V_i\}$	0.766	0.787	0.782
new plausibility approach	**0.852**	**0.844**	**0.820**
angle comparison	0.836	0.813	0.798
dilation	0.670	0.690	0.680
min-cut based	0.687	0.673	0.667

Table 2.8: Comparison of DSCs for the arcuate fasciculus phantom.

measure of fiber-tracking accuracy. Compared to the related work of Tournier et al. [2002] in which the deviation of single fibers from the ideal pathway is analyzed, the safety radius is a global measure of the tracked fiber bundle which gives us an indication of how close the tracked fiber bundle approaches the true border of the modeled pathway. Furthermore, in the aforementioned article, partial-volume effects are not explicitly included in the modeling, and the Rician distribution of magnitude MR images is only approximated. We systematically analyzed the influence of changes in the underlying image data and fiber-tracking parameters on the fiber-tracking error. The plot of standard deviation of the noise vs. safety radius (Fig. 2.3(c)) suggests that for the analyzed images in which the standard deviation of the noise is below 2, using a safety margin of 3 to 5 mm is appropriate for bundles of up to 20 cm length. Moreover, we analyzed the spatial distribution of tracked fibers with respect to the cross section of the fiber bundle. Fig. 2.4(b) shows that, on average, there are approximately half as many fibers located on the outer third of the bundle's cross section than on the inner third, given that they are the first to leave the bundle. To address this issue, it may be interesting to consider seed ROIs with larger densities of seed points on their exterior. The plot shows a high symmetry between the number of fibers on the interior portion of the fiber bundle path and on its exterior. From Fig. 2.3(a), we notice that within the considered range, the diameter of the fiber bundle does not seem to overly impact fiber-tracking results. Moreover, Fig. 2.3(d) shows that increasing the number of seed points above a certain density does not significantly improve tracking results. This suggests that multiple fibers which choose a few preferred paths play a major role in causing the size of the fiber bundle to be underestimated. We would like to analyze the performance

of fiber-tracking algorithms when a minimal distance between the tracked fibers is enforced. Fig. 2.3(b) indicates that the deflection-based algorithm works well if the fractional anisotropy of the "white matter" tensors is above 0.25, which should be the case for fiber bundles that do not cross. From Fig. 2.3(e), we notice that the analyzed fiber-tracking algorithm is initially fairly stable with respect to the used step length, and under certain noise conditions, it may be reasonable to use a step size slightly larger than the edge of image voxels. The reason for the difference in tracking precision when going from 5 to 6 mm step length is not clear, although it may be due to systematic error factors in the model, which need to be analyzed further.

Next, we focused on anatomically realistic models of the corticospinal tract and the arcuate fasciculus. To the best of our knowledge, this was the first attempt to create software models of specific neural fiber bundles, with curvatures and thicknesses that vary realistically along the path. In contrast to Leemans et al. [2005], the backbones of our fiber bundles are constructed not by linearly connecting consecutive points, but by applying cubic spline interpolation to far fewer control points. With our phantom, we were able to simulate image noise and to consider the partial-volume effects caused by the possible simultaneous presence of different white matter pathways, grey matter, and cerebrospinal fluid in one voxel. Other tissue volumes provided by the BrainWeb project that might be included in our phantom in later work include fat, skin, glial matter, and connective tissue. Scenarios in which crossing or kissing fibers are modeled have not yet been analyzed, but represent a straightforward extension of our model and shall be the topic of future work. Similarly to Section 2.3, we systematically changed image noise and fiber-tracking parameters and analyzed the change in safety radius. As a general consideration, tracking results produced by means of whole-brain fiber-tracking proved to be highly stable with respect to changing parameters (Fig. 2.11). Computing the safety radius on different slices along the corticospinal tract shows that the safety radius does not change significantly when moving up the corticospinal tract (Fig. 2.12), although some dependence on size, shape, and location of the cross section appears to be present. Figs. 2.11(a) and 2.11(b) indicate that for sufficiently high SNR, using a safety margin of 3 to 4 mm is appropriate for the corticospinal tract, whereas up to 6 mm may be used

for the arcuate fasciculus. Figs. 2.11(d) and 2.11(d) show the considerable effect that the number of seed points has on tracking results. However, when performing whole-brain tracking, a higher number of seed points may significantly increase the computational cost of the tracking, and a lower bound for the safety radius will eventually be reached. It appears that placing seed points on a grid with a spacing of 1 mm may be a good trade-off between precision and computational cost. Figs. 2.11(f) and 2.11(f) show remarkable stability of the safety radius when using different step lengths for the tracking algorithm. The reason for the difference when going from 3 to 4 mm in Fig. 2.11(f) is not yet clear and may also be due to possible nuisance variables in the model, such as for example discretization artifacts in the white matter atlas.

In Section 2.5, we suggested an efficient and easy-to-implement algorithm to generate a fuzzy segmentation of diffusion tensor images which is used to better estimate the precise extent of the tracked fiber bundle. To our knowledge, this is the first DTI segmentation algorithm to consider both the main diffusion direction of neighboring voxels and the respective covariance matrices. Experimental results on our DTI phantoms seem to confirm that when the covariance matrix of the main diffusion direction is taken into account, improved segmentation results may be obtained. In almost all tests, our algorithm performed better than the other considered approaches, although our comparison is not exhaustive, and further tests with different algorithms and images are needed. Fig. 2.13 shows examples in which considerable regions of the modeled corticospinal tract and arcuate fasciculus were not detected by the tracking algorithm but recovered by means of our algorithm. The upper right portion of the bundle in Fig. 2.13(a) is not fully recovered, likely due to a considerably higher amount of grey matter in those voxels compared to white matter, which results in an imprecise estimation of the main diffusion direction. Inclusion of additional knowledge about partial-volume effects may increase segmentation results. Moreover, further improvements may be obtained when incorporating information about the spatial relations among voxels, for example, by adding a weighted distance term as in Raj et al. [2011]; Rousson et al. [2004], or by using spectral clustering as in Ziyan et al. [2006]. Different sensible combinations of the plausibility term with a spatial regularization term need to be carefully examined. Compared to recent fiber clustering

algorithms such as Visser et al. [2011]; Wang et al. [2011], our algorithm is computationally less expensive: Whereas a single-threaded Matlab implementation of our algorithm produces segmentation results in less than 15 minutes on standard PC (Intel(R) Core(TM) i7 Processor), the mentioned algorithms would take hours in the same setting. Parallelization should offer much room for additional speed improvements. Further advantages include a complete analysis of the voxels in the neighborhood of tracked fibers (this may not be the case with fiber clustering algorithms where many fibers are eliminated if they do not satisfy the threshold conditions of the tracking algorithm) and a fuzzy segmentation, which offers some indication about the likelihood of a voxel being part of the bundle of interest. Nevertheless, a careful quantitative comparison between the two approaches is needed. Within our algorithm, we choose to rank voxels with a high variance in the components of the main diffusion direction vector as less likely to be part of the tracked fiber bundle. However, for certain applications in which it is critical not to underestimate the extent of the bundle, it may also be useful to classify all voxels presenting high uncertainty in the main diffusion direction, either because of noise or isotropic tensors, as potentially part of the fiber bundle. Also, the very important analysis of the case of kissing or crossing fibers has not been dealt with yet and will be part of a future systematic analysis. The algorithm was also tested on a real diffusion tensor magnetic resonance dataset, giving convincing results. Based on our experience with DTI phantoms, it seems reasonable to analyze voxels within approximately 5-7 mm of the tracked fibers. Open questions include finding an optimal threshold parameter over the resulting fuzzy segmentation and extending the algorithm to utilize information given by additional tensor-derived quantities, such as trace or fractional anisotropy (and respective uncertainties).

2.7 Conclusions

With this paper, we have gained some insight into the relationship between underlying image data, fiber-tracking parameters, and the capabilities of fiber-tracking. Our analysis was restricted to the precision of a streamline tractography algorithm, but should be extended to other approaches, such as probabilistic ones.

2. SEGMENTATION OF FIBER TRACTS BASED ON AN ACCURACY ANALYSIS ON DIFFUSION TENSOR SOFTWARE PHANTOMS

Even though the "safety radius", which has been used as measure of accuracy, is not directly applicable to real data where the ground truth is unknown, the presented analysis should be useful in assessing the necessary image quality and proper parameters for fiber-tracking. We have introduced new ideas for generating realistic DTI phantoms and would like to build upon them. In order to improve the estimate of the true border of a tracked fiber bundle on both simulated and real MR data, we suggested a fuzzy DTI segmentation algorithm which analyzes the differences in main diffusivities between tensors and the respective uncertainties. Segmentation results were visualized in 2D as color-coded plausibility maps around tracked fibers and in 3D as semi-transparent confidence hulls. We hope this information will be useful to clinicians to better assess the precision and reliability of fiber-tracking results.

Chapter 3

DTI Segmentation via the Combined Analysis of Connectivity Maps and Tensor Distances

This chapter of the thesis is based on the publication Barbieri et al. [2012a].

3.1 Abstract

We describe a novel approach to extract the neural tracts of interest from a diffusion tensor image (DTI). Compared to standard streamline tractography, existing probabilistic methods are able to capture fiber paths that deviate from the main tensor diffusion directions. At the same time, tensor clustering methods are able to more precisely delimit the border of the bundle. To the best of our knowledge, we propose the first algorithm which combines the advantages supplied by probabilistic and tensor clustering approaches. The algorithm includes a post-processing step to limit partial-volume related segmentation errors. We extensively test the accuracy of our algorithm on different configurations of a DTI software phantom for which we systematically vary the image noise, the number of gradients, the geometry of the fiber paths and the angle between adjacent and

crossing fiber bundles. The reproducibility of the algorithm is supported by the segmentation of the corticospinal tract of nine patients. Additional segmentations of the corticospinal tract, the arcuate fasciculus, and the optic radiations are in accordance with anatomical knowledge. The required user interaction is comparable to that of streamline tractography, which allows for an uncomplicated integration of the algorithm into the clinical routine.

3.2 Introduction

Diffusion tensor imaging (DTI) is a magnetic resonance imaging method which, at each voxel, models the three-dimensional motion of protons in water molecules by a normal distribution of 0-mean and the covariance matrix of which is proportional to the diffusion tensor (Basser et al. [1994b], Pierpaoli and Basser [1996]). Assuming that in white matter (WM) regions, where diffusion is highly anisotropic, the principal diffusion direction matches the orientation of the corresponding underlying fiber system, the 3D architecture of WM fiber pathways may be reconstructed *in-vivo*. This can be accomplished by fiber tracking (FT) algorithms (see Basser [1998], Mori et al. [1999]), which may, however, under- or overestimate the spatial extent of fiber bundles, as demonstrated by Huang et al. [2004] and Kinoshita et al. [2005]. For an overview of current tractography techniques, see Johansen-Berg and Behrens [2009]. While deterministic FT algorithms generally output a set of streamlines which describe the course of the tracked fiber bundle, probabilistic approaches generate a connectivity map (also called a tractogram) which describes the probability of a connection existing between an image voxel and a given region of interest (ROI). Direct segmentation of the tensor field, for example via tensor clustering, represents an alternative possibility to extract fiber bundles which allows for the exploitation of the coherence that exists (at least locally) between tensors belonging to a specific structure. Several examples of probabilistic FT techniques, DTI segmentation algorithms as well as the contributions of our approach are discussed in the following sections.

In order to illustrate the aim of this study, Fig. 3.1 shows schematic tract extraction results based on different techniques. In Fig. 3.1(a) a tensor clustering approach is employed which is not able to determine that isotropic tensors in

the region of crossing fibers are part of the bundle. In Fig. 3.1(b) we display a connectivity map: it is very difficult to determine the exact border of the fiber tract based solely on this tractogram. In Fig. 3.1(c) the segmentation result is generated using the hereby proposed method, which combines the complementary information obtained via tensor clustering and the connectivity map.

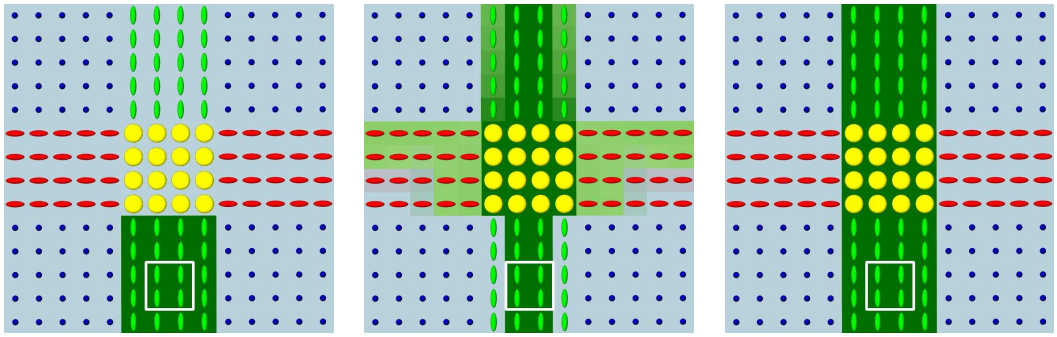

(a) (b) (c)

Figure 3.1: (a) Example segmentation of the fiber bundle running in the y direction based solely on tensor clustering. The white square delimits the seed ROI. The segmented region is displayed in green. (b) Example connectivity map associated with the ROI delimited by the white square. (c) Example correct segmentation computed using the proposed algorithm which combines the information given by the computed distances between tensors and the information given by the connectivity map.

To investigate the validity and precision of reconstructed white matter pathways, hardware or software phantoms, which constitute a model with a known fiber network, may be used (compare Gössl et al. [2002], Lori et al. [2002], Fieremans et al. [2008], Fillard et al. [2011]). In this work, we employ software phantoms to validate our segmentation approach because they can be easily modified to account for different scanner parameters, image noise, and angles between crossing bundles, and can be used to model additional fiber bundles surrounding the tract of interest.

3.2.1 Related Work

We now present a brief overview on publications dealing with the segmentation of DTI data. In early work on the topic, Zhukov et al. [2003] use level-set evolution to segment cerebral structures based on tensor anisotropy. Wiegell et al.

[2003] use the Frobenius norm as a distance measure between tensors and k-means clustering to segment thalamic nuclei. Similarly using the Euclidean distance between tensors, Wang and Vemuri [2004b] and Rousson et al. [2004] extend the geodesic active contours model to DTI data. The works of Wang and Vemuri [2004a] and Lenglet et al. [2004b] aim to minimize the relative entropy of the region to be segmented. A shortcoming of the Euclidean metric is that averaging leads to artificial *tensor swelling*, which is overcome by the introduction of affine-invariant Riemannian metrics by Pennec et al. [2006], also employed in this paper. Lenglet et al. [2005] employ the affine-invariant Riemannian distance in a Bayesian framework for DTI segmentation, although they represent each class by a single Gaussian distribution on the tensor manifold. Awate et al. [2007] employ Log-Euclidean metrics, non-parametric kernel density estimation, and an information-theoretic formulation to achieve a fuzzy segmentation of the tensor field. In their approach, each class is characterized by a fixed number of tensor parameters which are iteratively updated and relies on an initialization which captures the variety of tensors belonging to the fiber bundle. Moreover, in case the algorithm is used to achieve a crisp segmentation, voxels presenting partial-volume artifacts are simply considered part of the most likely region.

At the same time, research on determining quantitative tractography indices of "connectivity" from a given ROI to other brain regions has advanced. Recent approaches provide high robustness to noise, partial-volume artifacts, and are able to deal with fiber crossings. A first type of algorithm based on Bayesian models includes work by Behrens et al. [2003] and Friman et al. [2006], who introduce stochastic tractography algorithms by modeling the local uncertainty in fiber orientation. Parker et al. [2003] likewise infer directional uncertainty based on the fractional anisotropy of diffusion tensors. An extension that takes into account global information, such as priors on connections among brain regions, has been presented by Jbabdi et al. [2007]. A drawback of these methods is the long computation time due to the use of Markov chain Monte Carlo methods or the extensive sampling of probability density functions. Front-propagation methods make use of level sets (O'Donnell et al. [2002], Lenglet et al. [2004a]), fast marching methods (Parker et al. [2002], Prados et al. [2006], Jbabdi et al. [2008]), or iterative sweeping techniques (Jackowsky et al. [2005]) to evolve a

front at the seed ROI based on the information about diffusion strength and direction given by the tensor field. A limitation of this class of algorithms is that it is often difficult to integrate prior knowledge into the algorithm, such as the explicit exclusion of a connection between two brain regions. Graph-based techniques such as those by Iturria-Medina et al. [2008] and Sotiropoulos et al. [2010] represent image voxels as graph nodes; neighboring voxels are connected by edges weighted according to both structural and diffusivity features. The properties of the network are studied in order to determine the probability of two voxels being linked by a fiber pathway. In general, although connectivity maps provide a good indication of the likelihood of a link between two brain regions, determining a threshold value to precisely extract the connecting fiber bundle remains an open problem.

3.2.2 Contributions

The main contributions of this paper may be summarized as follows:

- We propose a DTI segmentation algorithm which combines connectivity information with local tensor clustering to extract a tract of interest.
- The problem of voxels being misclassified because of partial-volume artifacts is explicitly addressed by the algorithm.
- The accuracy of the algorithm is tested on a DTI software phantom for which we systematically vary the image noise, the number of gradients, the fiber paths, and the angle between adjacent and crossing fiber bundles.
- The accuracy of the algorithm is analyzed in terms of differences in both volume and surface distances between segmentation result and ground truth.
- The reproducibility of the algorithm is supported by the segmentation of the corticospinal tract of nine patients.
- We examine specific clinical issues such as the behavior of the algorithm in the vicinity of tumors or lesions.

- The segmentation algorithm does not require additional user interaction compared to standard streamline tractography. The implementation described in this paper requires under half an hour to compute the connectivity map and segment the tract of interest. These considerations should make the algorithm viable for clinical use.

3.3 Methods

In this section, we describe the proposed segmentation approach and the software phantom used to validate it.

3.3.1 Algorithm

Let us begin by summarizing the individual steps of our algorithm, which will later be explained in detail. First we compute a connectivity map of the tract of interest. Although in this paper we employ a specific algorithm to generate the tractogram, in principle it should be possible to employ any other probabilistic FT technique. The tractogram is also used as an initial fuzzy segmentation mask by our segmentation algorithm. The segmentation mask is then iteratively updated according to two criteria: the connectivity information given by the tractogram and local tensor clustering. Because the optimal threshold value on the connectivity map used for the separation of the tract of interest from the surrounding structures is unknown, we estimate the distribution of connectivity values associated with the tract via nonparametric probability density function (PDF) estimation. This technique was pioneered by Rosenblatt [1956] and Parzen [1962] and employed in image segmentation by Mory et al. [2007]. At the same time, we analyze the Log-Euclidean distance from a tensor to the local mean of tensors belonging to the tract and to the local mean of tensors belonging to surrounding structures. We update the segmentation map at each voxel to either a higher value if these two clues indicate that the voxel belongs to the tract of interest or to a lower value otherwise. As a regularization step, we make use of subsequent morphological closing and opening of the segmentation mask. The process is iterated until the algorithm converges. In a final post-processing step,

tensors bordering the segmented tract are checked for partial-volume artifacts.

3.3.1.1 Notation and Computation of the Connectivity Map

Let us denote the diffusion tensor image by I. Furthermore, we define a fuzzy membership function m over the domain Ω of I, which assumes values between 1 for voxels certainly belonging to the tract of interest and 0 for voxels certainly belonging to surrounding structures.

The method used to compute the connectivity map $\mathcal{C}$ associated with the tract to be segmented is based on the variational noise FT algorithm presented by Klein et al. [2010a]. This probabilistic approach has been shown to produce qualitatively similar results to the Bayesian FT presented by Friman et al. [2006], albeit in a shorter time, making it appealing for clinical applications. Specifically, the variational noise FT algorithm repeatedly adds complex Gaussian noise to the magnitude diffusion-weighted images (see Hahn et al. [2006] for details) and computes a deterministic FT. In this work, for each deterministic FT result we compute a binary mask which is 1 at voxels pierced by tracked fibers and 0 elsewhere. The tractogram $\mathcal{C}$ is given by the average of these binary masks. The employed deterministic FT is based on the deflection-based approach by Weinstein et al. [1999], which is able to achieve good reconstruction results at fiber crossings by considering the full tensor information. A detailed description of our deterministic FT algorithm can be found in Barbieri et al. [2011b].

3.3.1.2 The Connectivity Factor

The first value used to update the membership function m at a voxel x is derived from the connectivity measure $\mathcal{C}(x)$. The PDFs associated to distributions of connectivity values for voxels belonging to the tract of interest and to the surrounding structures are computed via continuous Parzen-Rosenblatt windows as

$$\begin{aligned} p_{\text{TRACT}}(\mathcal{C}(x)) &= \frac{\int_\Omega m(y)\, K(\|\mathcal{C}(x)-\mathcal{C}(y)\|,\sigma)\, dy}{\int_\Omega m(y)\, dy} \\ p_{\text{NOT TRACT}}(\mathcal{C}(x)) &= \frac{\int_\Omega (1-m(y))\, K(\|\mathcal{C}(x)-\mathcal{C}(y)\|,\sigma)\, dy}{\int_\Omega (1-m(y))\, dy} \end{aligned} \tag{3.1}$$

where the kernel $K(\cdot, \sigma)$ is a Gaussian function. Popular approaches for the selection of an appropriate bandwidth parameter σ include methods based on cross-validation, such as Chow et al. [1983], and plug-in methods such as Raykar and Duraiswami [2005, 2006]. The latter is employed in this work because of the quick computation times of this method. The basic idea underlying plug-in methods is that the bias of an estimate PDF $\hat{f}$ is written in terms of the unknown PDF f, after which a pilot estimate of f is "plugged-in" the equation to derive an estimate of the mean integrated squared error. The "optimal" bandwidth σ minimizes this measure of fit. As an example, hypothetical resulting PDFs are displayed in Fig. 3.2.

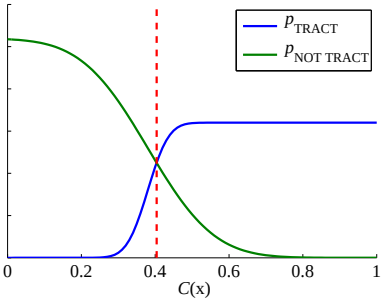

Figure 3.2: Hypothetical resulting PDFs $p_{\text{TRACT}}(\mathcal{C}(x))$ and $p_{\text{NOT TRACT}}(\mathcal{C}(x))$. We would expect voxels with a connectivity value higher than 0.4 to be part of the tract of interest.

A connectivity factor $f_{\text{CONNECTIVITY}}(x)$ is computed as the logarithm (to reduce the dynamic range) of the ratio between the two probabilities:

$$f_{\text{CONNECTIVITY}}(x) = \log\left(\frac{p_{\text{TRACT}}(\mathcal{C}(x))}{p_{\text{NOT TRACT}}(\mathcal{C}(x))}\right). \tag{3.2}$$

A high value for the connectivity factor at voxel x corresponds to a high confidence that the voxel is part of the tract of interest.

3.3.1.3 The Clustering Factor

A second ingredient used to update the membership function m is the result of a local fuzzy c-means clustering algorithm, a technique first introduced by Bezdek [1981]. Arsigny et al. [2006] showed that the matrix logarithm describes a map-

ping from the six-dimensional Riemannian manifold $S^+(3,\mathbb{R})$ of 3×3 real symmetric positive-definite matrices to a Riemannian manifold with zero curvature which is diffeomorphic and isometric to the associated Euclidean vector space. Given a candidate voxel x with neighborhood $\mathcal{N}(x)$, the mean tensors that represent the centers of the two possible clusters (the fiber tract of interest and the surrounding tensors) may be computed as

$$\begin{aligned} M_{\text{TRACT}}(x) &= \exp\left(\int_{\mathcal{N}(x)} m(y)\log(I(y))\,dy\right) \\ M_{\text{NOT TRACT}}(x) &= \exp\left(\int_{\mathcal{N}(x)} (1-m(y))\log(I(y))\,dy\right). \end{aligned} \tag{3.3}$$

Distances from the tensor at voxel x to the centers are computed as

$$\begin{aligned} d_{\text{TRACT}}(x) &= \|\log(M_{\text{TRACT}}(x)) - \log(I(x))\|_F \\ d_{\text{NOT TRACT}}(x) &= \|\log(M_{\text{NOT TRACT}}(x)) - \log(I(x))\|_F \end{aligned} \tag{3.4}$$

where $\|\cdot\|_F$ is the Frobenius norm. A schematic representation of the process is presented in Fig. 3.3.

A clustering factor $f_{\text{CLUSTERING}}(x)$ is computed as the logarithm (to reduce the dynamic range) of the ratio between the two distances:

$$f_{\text{CLUSTERING}}(x) = \log\left(\frac{d_{\text{NOT TRACT}}(x)}{d_{\text{TRACT}}(x)}\right). \tag{3.5}$$

A high value for the clustering factor at voxel x corresponds to a high confidence that the voxel is part of the tract of interest.

3.3.1.4 Updating the Membership Function and Regularization

For the sake of efficiency, we do not need to update the membership function at each image voxel, but may restrict ourselves to voxels that are likely part of the tract of interest or at the outer border, i.e., voxels for which the membership function m dilated with a structuring element B (mathematically: $m \oplus B$) is greater than 0.5. For the resulting set of voxels, the membership function is

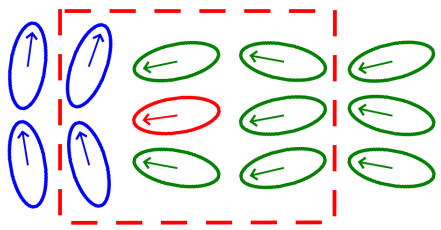

(a)

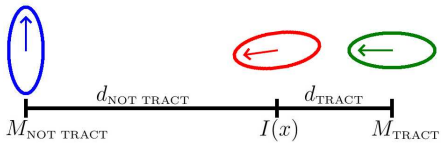

(b)

Figure 3.3: (a) Suppose we want to classify the red tensor $I(x)$ according to c-means clustering. The blue tensors have previously been classified as not being part of the tract and the green tensors have been classified as being part of the tract. The dashed red line represents the considered neighborhood $\mathcal{N}(x)$ of the red tensor. (b) A schematic representation of the computed cluster means and their distances to the tensor $I(x)$. With $I(x)$ being closer to the mean of the tract tensors, we expect it to be part of the tract.

updated according to

$$m(x) \leftarrow m(x) + \mu \cdot f_{\text{CONNECTIVITY}}(x) + \omega \cdot f_{\text{CLUSTERING}}(x) \tag{3.6}$$

where $\mu, \omega \in \mathbb{R}$ are weights for the connectivity and clustering factors respectively. As a regularization step, we apply a subsequent (grayscale) morphological closing and opening with a 3×3×3 cross-shaped structuring element to the membership function m. The process is repeated until the total change in m is smaller than a predefined threshold.

3.3.1.5 Partial-Volume Correction

With this post-processing step, we correct for partial-volume related errors in the segmentation. We define the outer border of the segmented object as the set of voxels for which the membership function is smaller than 0.5, but for which the dilated membership function $m(x) \oplus B$ is greater than 0.5. For a voxel x out of this set, we consider the 27-neighborhood of the tensor $I(x)$ and find the N pairs

of tensors $(\Sigma_i, \Omega_i)_{i=1,\ldots,N}$ for which Σ_i has been classified as part of the tract of interest, Ω_i as part of the surrounding structures, and for which Σ_i and Ω_i have opposite coordinates with respect to x. In the Log-Euclidean setting, a geodesic connecting these tensors is given by (Arsigny et al. [2006])

$$\Gamma_i(t) = \exp((1-t)\log(\Sigma_i) + t\log(\Omega_i)) \quad \text{for } t \in [0,1] \tag{3.7}$$

and $\Gamma_i(0.5)$ may be considered the geodesic average between Σ_i and Ω_i, which we assume to be similar to a partial-volume artifact between the two tensors. We can now consider the set of tensors belonging to surrounding structures $\{\Omega_i\}$ and the set of partial-volume tensors $\{\Gamma_i(0.5)\}$ and classify $I(x)$ according to the nearest neighbor criterion:

$$m(x) \leftarrow \begin{cases} m(x) \oplus B & \text{if } \min_i d_g(I(x), \Gamma_i) < \min_i d_g(I(x), \Omega_i) \\ m(x) & \text{otherwise} \end{cases}$$

where d_g is the Log-Euclidean distance between tensors. A schematic representation of the process is presented in Fig. 3.4.

3.3.1.6 Overview of the Algorithm

We now present an overview of how the different steps of the algorithm are combined and how sets of voxels are selected as candidates for classification. For all morphological operations, we use the structuring element B given by a voxel and its 6-voxel neighborhood. We chose this structuring element because of its small impact on the final shape of the object mask. The closing and opening operations are represented by $\bullet$ and $\circ$, respectively.

{**Algorithm Start**}
Compute the connectivity map $\mathcal{C}$ according to Section 3.3.1.1.
Set $m^0 = \mathcal{C}$.
{Main Segmentation Step}
repeat

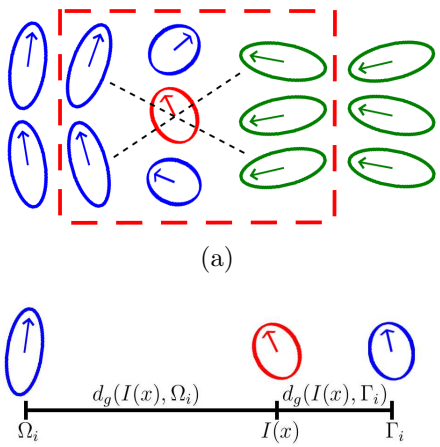

Figure 3.4: (a) Assume the blue and red tensors have been classified as not being part of the tract and the green tensors have been classified as being part of the tract. We want to check that the red tensor $I(x)$ has not been misclassified because of partial-volume artifacts. Neighboring tensors (dashed red line) with opposite coordinates with respect to x (those connected by the dashed black lines) are used to compute a set of partial-volume tensors $\{\Gamma_i\}$. (b) The distances from $I(x)$ to both the partial-volume tensors $\{\Gamma_i\}$ and the not-tract tensors $\{\Omega_i\}$ are computed. Being $I(x)$ closer to a partial-volume tensor Γ_i, we expect it to be part of the tract.

Determine the set of voxels S belonging to the object mask or to the outer border; these are the voxels for which $m^i(x) \oplus B > 0.5$.

for all $x \in S$ **do**

determine the connectivity factor $f_{\text{CONNECTIVITY}}(x)$ according to Section 3.3.1.2.

determine the clustering factor $f_{\text{CLUSTERING}}(x)$ according to Section 3.3.1.3.

update $m^i(x)$ according to Section 3.3.1.4.

end for

Regularize m^i via subsequent morphological closing and opening: $m^{i+1} = m^i \bullet B \circ B$.

until $\|m^{i+1} - m^i\| < \varepsilon$

{Partial-Volume Correction Step}

Determine the set of voxels S belonging to the outer border of the object mask, these are the voxels for which $m^i(x) < 0.5$ and $m^i(x) \oplus B > 0.5$.

for all $x \in S$ **do**

Check for partial-volume artifacts at the border of the tracked bundle and update $m^i(x)$ according to Section 3.3.1.5.

end for

Regularize m^i via subsequent morphological closing and opening: $m^{i+1} = m^i \bullet B \circ B$.

{**Algorithm End**}

3.3.2 Software Phantom

In order to test the accuracy of our algorithm, we generate a set of synthetic diffusion-weighted images of two fiber bundles. The first bundle has the shape of a cylinder and the second bundle has a helical path around the first bundle. This phantom allows us to simulate DTI data corresponding to many different configurations of adjacent fiber bundles; two examples are shown in Figs. 3.5(a) and 3.5(b).

The diffusion-weighted signal is obtained according to the composite hindered and restricted model of diffusion (CHARMED) by Assaf et al. [2004], Assaf and Basser [2005], and the eigenvalues of the diffusion tensors are set according to measurements in white matter reported by Pierpaoli et al. [1996] and Bhagat and Beaulieu [2004]. Partial-volume artifacts are modeled by computing the volume of intersection between a voxel and the cylinder which delimits the first fiber bundle. The signal attenuation produced by the two bundles is then weighted accordingly. It is known from Gudbjartsson and Patz [1995] that noise in magnitude magnetic resonance data is Rician distributed. As suggested by Hahn et al. [2006], such noise distribution may be simulated in the image by computing $|E(\mathbf{q}, \Delta) + \tilde{N}(0, \sigma^2)|$, where $E(\mathbf{q}, \Delta)$ is the diffusion-weighted (DW) signal and $\tilde{N}(0, \sigma^2)$ is a Gaussian-distributed complex variable with mean 0 and variance σ^2. Using standard fitting procedures, we use the diffusion-weighted images to compute the tensor-valued image. Example slices of the generated tensor fields are shown in Figs. 3.5(c) and 3.5(f) together with the user-defined ROIs used for segmentation. In order to simulate crossing (or kissing) fiber tracts a third bundle is added to the phantom.

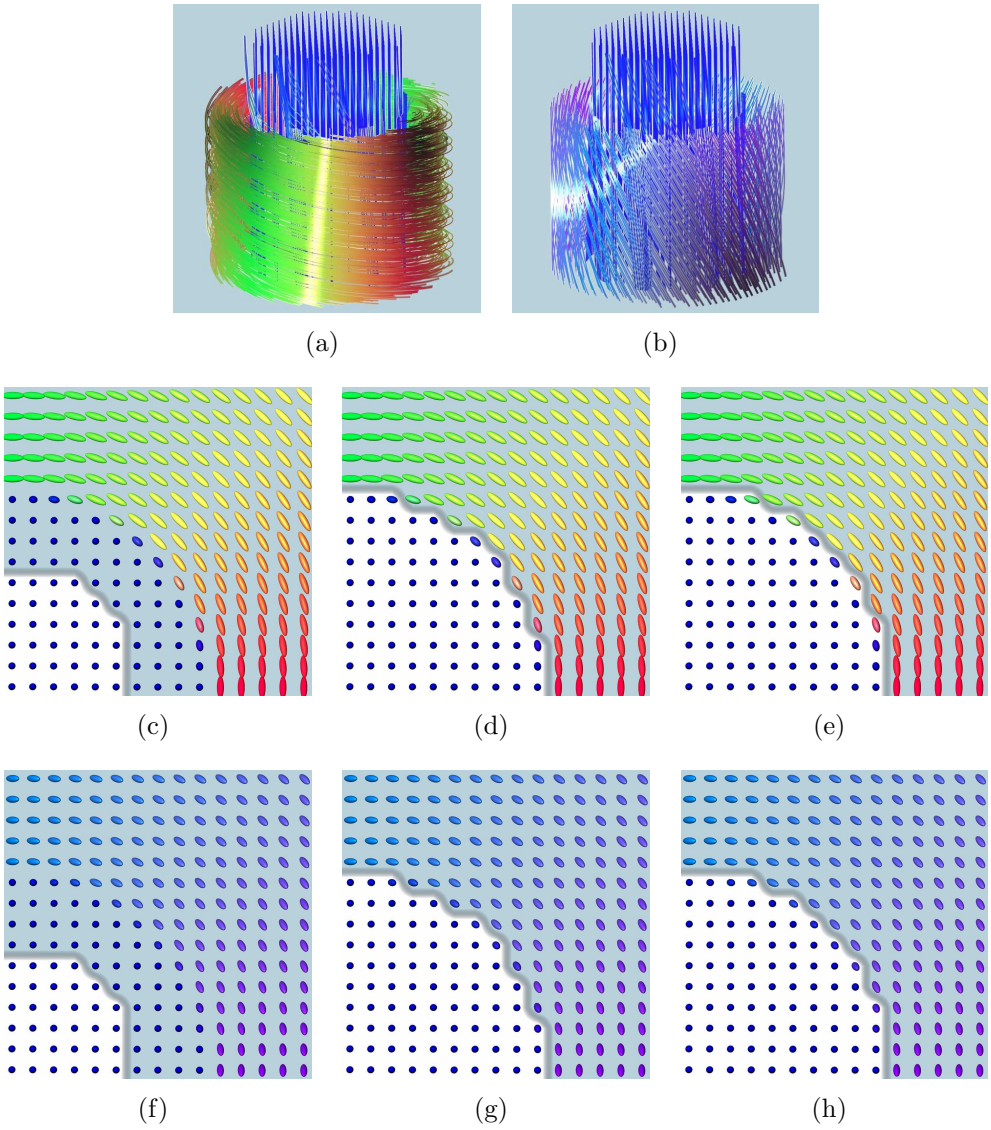

Figure 3.5: (a),(b) Examples of tracked cylindrical and helical fiber bundles. The pitches of the helical paths are set to $0.2 \cdot 2\pi$ mm and $1.8 \cdot 2\pi$ mm, respectively. (c),(f) Details of the DTI software phantoms corresponding to the two helical paths. The user-defined ROIs used to initialize the segmentation are shown in white. (d),(g) The segmentations of the cylindrical fiber bundle obtained without taking into account partial-volume artifacts are shown in white. (e),(h) The final segmentations obtained by means of our algorithm. Tensors presenting considerable partial-volume artifacts are segmented correctly.

3.4 Results

In the following sections, we evaluate our segmentation algorithm in terms of accuracy, reproducibility, and efficiency.

3.4.1 Accuracy Analysis

The default image parameters used to generate the phantom described in Section 3.3.2 are reported in Table 3.1. We perform five experiments in which we independently vary one of the phantom parameters, as specified in Table 3.2, and segment the cylindrical fiber bundle with our algorithm. When varying the number of gradients, we use the first n gradients out of the original 30. When varying the angle between the axis of the cylinder and the z-axis, the axis of the cylinder always lies on the plane for which $x = y$.

	Default value
noise standard deviation	2.5
radius of the cylinder	10 mm
pitch of the helical path	2π mm
number of gradients	30
angle between z-axis and cylinder-axis	0 deg
voxel size	$1\times1\times1$ mm^3
b value	1000 s/mm^2
noise-free $b = 0$ intensity	70

Table 3.1: Default parameters used to generate the DTI software phantom.

	start value	**step**	**end value**	
noise standard deviation	0	0.5	5.5	
radius of the cylinder	5.5	0.5	10	mm
pitch of the helical path	0	0.2	1.8	$\cdot 2\pi$ mm
number of gradients	6	3	30	
angle between z-axis and cylinder-axis	0	10	90	deg

Table 3.2: Parameter variation for the different experiments. The signal to noise ratio (SNR) corresponding to the different noise standard deviation values ranges from approximately 13 to $+\infty$.

For each set of parameters, we add noise to the magnitude images and repeat the experiment 10 times. As the seed ROI used to compute the connectivity map $\mathcal{C}$, we use a circular region perpendicular to the axis of the cylinder and of

two thirds its radius. In our experiments, the membership function m always converges to an approximately binary segmentation mask. If the fiber bundle is reconstructed by means of streamline tractography, and a binary mask is computed based on the tracked fibers, we obtain a Dice similarity coefficient (DSC, see Zou et al. [2004]) between segmentation result and ground truth of approximately 0.66. For a given segmentation result, part of the surface may lie inside the ground truth (the extent of the tract has been underestimated) or outside the ground truth (the extent has been overestimated). Surface points may thus be divided into inner and outer points. We define the maximal inner distance as the maximal distance between an inner point and the ground truth surface. Similarly, the maximal outer distance is defined as the maximal distance between an outer point and the ground truth surface. The average distance between sampled surface points and the ground truth gives the average distance between segmentation result and ground truth. Fig. 3.6 shows boxplots of the DSCs obtained by means of the proposed algorithm and plots of the average distance, the maximal inner distance, and the maximal outer distance. For almost all parameter settings, the average distance between segmentation result and ground truth is below 1 mm (or one voxel). The jumps visible in the cylinder radius vs. DSC boxplots are likely due to different partial-volume artifacts that depend on whether the cylinder border coincides with the voxel border or not.

In Fig. 3.7, segmentation results of fiber bundles crossing (or kissing) with different angles of incidence are presented. In order to generate the software phantom we set the noise standard deviation to 2.5, the b value to 1000 s/mm^2 and make use of 30 gradient directions. The standard deviation σ_{VAR} of the variational noise used to generate the connectivity map is equal to 2.5. In Figs. 3.7(a) the angle of incidence is 45 degrees. When generating the connectivity map, almost all streamlines deviate to the left branch and therefore the segmentation algorithm fails to resolve the central fiber branch. In Figs. 3.7(b), (c), the angle is 70 degrees while in Fig. 3.7(d) it is 90 degrees. In these cases, the central fiber bundle is reconstructed correctly and exclude ROIs may be used to extract different tracts.

In Fig. 3.8, we analyze the effect of varying the ratio μ/ω from 0 (tensor clustering only) to $+\infty$ (threshold on connectivity map only) when extracting

fiber bundles crossing at 45, 70, or 90 degrees. For the purpose of comparison, we increase σ_{VAR} to 10 in order to generate a connectivity map with which the fibers crossing at 45° can be resolved. The plot indicates that for all three angles the best segmentation result is obtained when using a ratio μ/ω of approximately 0.3.

3.4.2 Reproducibility Analysis

The small standard deviation of the boxplots in Fig. 3.6 based upon segmentation results on the DTI software phantom indicates a good reproducibility of the algorithm independent of the specific noise function applied to the image.

To further support the reproducibility of our algorithm independent of the considered patient, we compute the segmentation of the right corticospinal tract of nine subjects affected by multiple sclerosis (MS). For all patients, we place a seed ROI in the internal capsule and two exclude ROIs (to eliminate false positives) in the corpus callosum and the middle cerebral peduncle. The deterministic tracking used to compute the connectivity map is repeated 100 times. Segmentation results are presented in Fig. 3.9. We perform a pairwise manual affine registration of the patient datasets and compute the DSCs corresponding to tracts extracted via streamline FT and via the proposed segmentation approach. Overall, streamline FT yields a DSC of 0.432 ± 0.055 (median 0.423) while the new algorithm yields a DSC of 0.497 ± 0.047 (median 0.499). This result indicates that the reproducibility of the new algorithm is comparable or even better than the one of the employed streamline FT, possibly because the new algorithm is able to discard false positives.

We also test the performance of the algorithm depending on the size of the neighborhood $\mathcal{N}(x)$. As default we employ a cube with edge length 13 mm. We vary the edge length, compute the segmentation results on the MS patient datasets, and compare them with the results obtained when using the default length. A boxplot of the resulting DSCs is presented in Fig. 3.10.

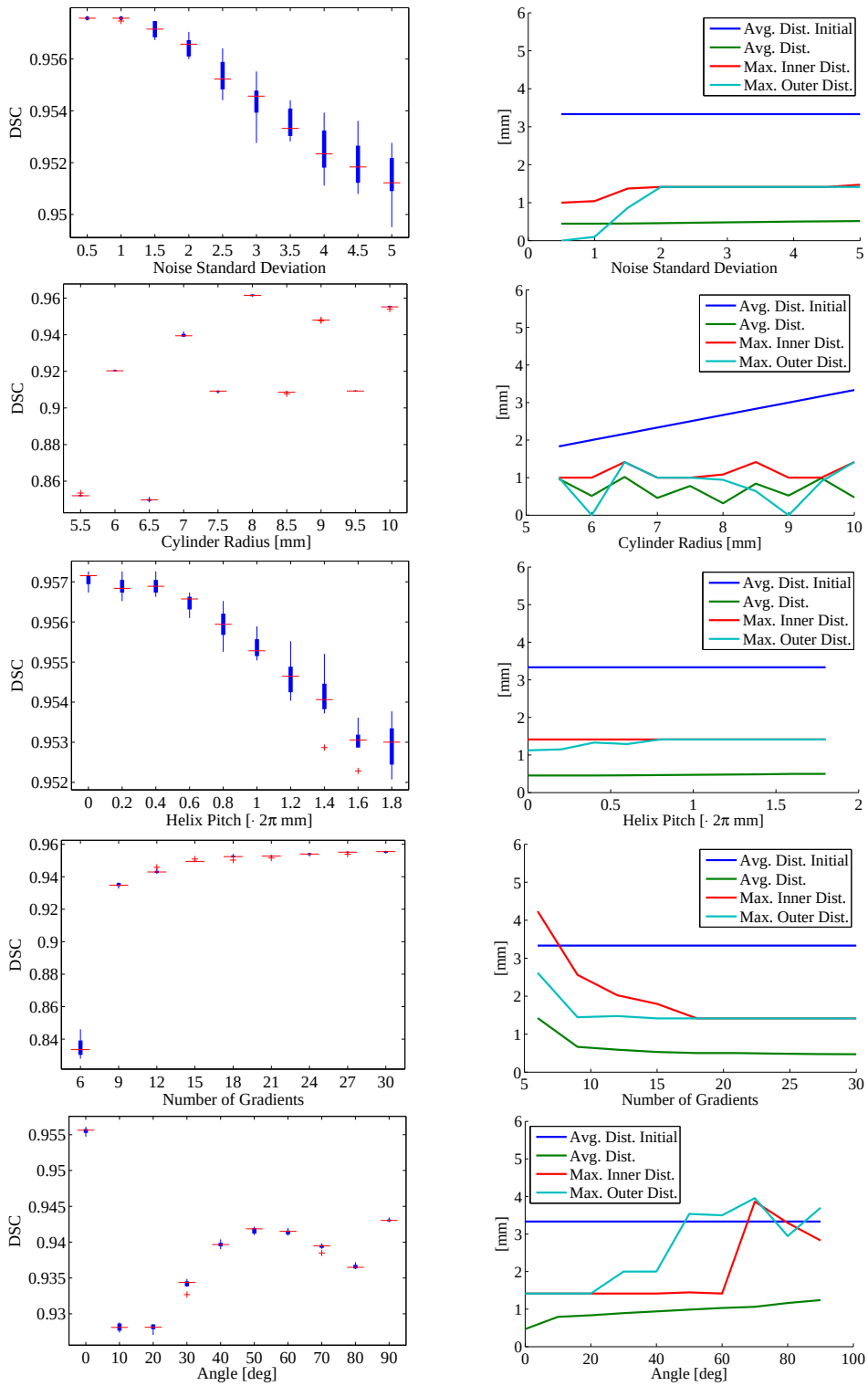

Figure 3.6: Segmentation results on the DTI software phantom. Image parameters are set according to Tables 3.1 and 3.2. The left column shows the computed DSCs and the right column shows the average, maximal inner, and maximal outer distances between segmented fiber bundle and ground truth. The average distance of the initial seed ROI to the border of the bundle is also provided.

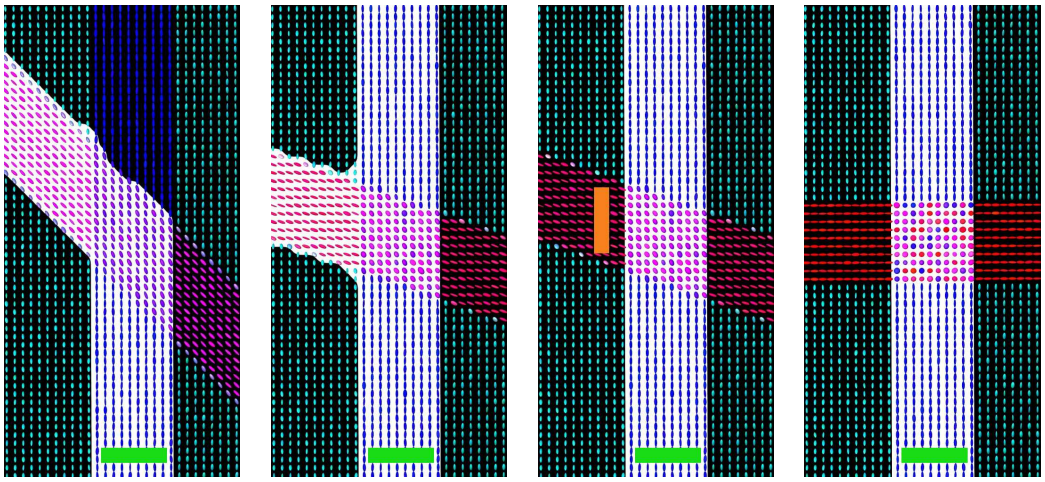

(a) (b) (c) (d)

Figure 3.7: Segmentation (shown in white) of fiber bundles crossing/kissing with different angles of incidence. The position of the initial seed ROI is shown in green. Different segmentation results may be obtained by eliminating streamlines that go through exclude ROIs (shown in orange) when generating the connectivity map.

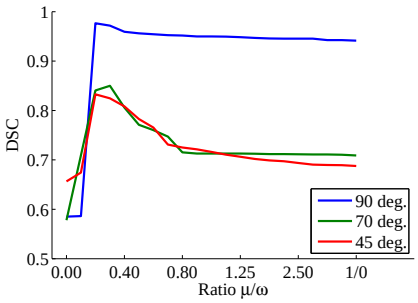

Figure 3.8: DSCs of segmentations of bundles crossing at different angles obtained when varying the ratio μ/ω from 0 (tensor clustering only) to $+\infty$ (threshold on connectivity map only).

3.4.3 Efficiency Analysis

The segmentation algorithm is further tested on additional datasets and used to reconstruct different fiber bundles. Figs. 3.11 and 3.12 show the segmentation of the corticospinal tract of one patient with intracerebral metastases and of one with glioma. These datasets are publicly available from the IEEE Visualization Contest 2010 website. In both cases, a direct analysis of the tensor field presented in Fig. 3.13 suggests that the proposed algorithm may improve the determina-

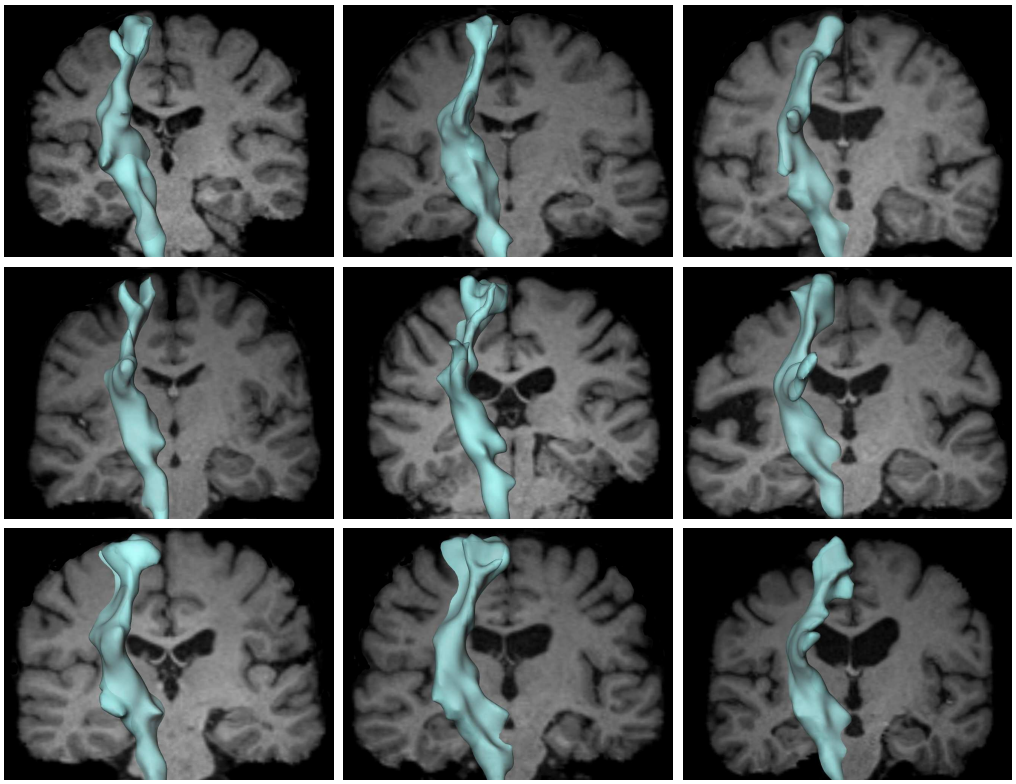

Figure 3.9: Segmentation of the right corticospinal tract of nine subjects affected by multiple sclerosis. The parameters of the DTI acquisition sequence are as follows: resolution = $1.80 \times 1.80 \times 1.98$ mm^3, b value = 1000 s/mm^2, NEX = 2, TR/TE = 10700/84 ms, number of DW images = 31 (one b=0).

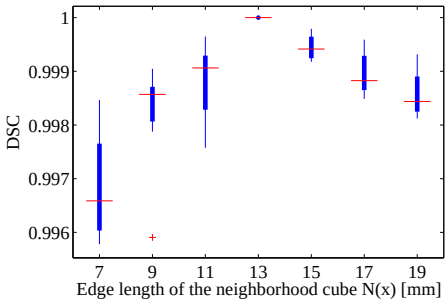

Figure 3.10: DSCs between segmentation results obtained when setting the edge length of the cube $\mathcal{N}(x)$ to 13 mm and segmentation results obtained when varying this edge length.

tion of the distance between tract and tumor when compared with streamline tractography.

In Fig. 3.14, we present the segmentation of the optic tract and the arcuate fasciculus of a healthy volunteer. Because the reconstruction of these fiber bundles via streamline- or deflection-based FT is often insufficiently accurate, we employ the global FT algorithm presented by Klein et al. [2012]. The binary segmentation mask associated with the tracked fibers is smoothed with a Gaussian kernel to simulate a "connectivity map". This map is then used as an input to the segmentation algorithm.

The segmentation algorithm was implemented on an Intel(R) Core(TM) i7 PC based on a single-threaded MeVisLab implementation. The most computationally intensive step of the algorithm is the initial computation of the connectivity map via variational noise. This takes approximately 30 minutes for each case. The main segmentation step together with the partial-volume correction step takes between one and two minutes. Therefore the proposed technique may offer a good compromise between the speed of streamline tractography (computational time of a few seconds) and the precision of global optimization algorithms (computational time of hours, as for example in Fillard et al. [2009], Reisert et al. [2010]). It should be possible to achieve a considerable increase in speed in both the computation of the tractogram (because many deterministic trackings with noisy data are independently repeated) and the main segmentation step (because the algorithm operates voxelwise) via parallelization. The time required by the user to determine the seed and exclude ROIs for the deterministic trackings varies considerably depending on the specific fiber bundle and the experience of the user. It should be noted, however, that no new skills need to be acquired by users who are already familiar with standard streamline tractography. The segmentation result may be presented together with the tracked fibers as an additional source of information.

3.5 Discussion and Conclusion

We presented a novel DTI segmentation algorithm that combines the information provided by connectivity maps with local fuzzy c-means tensor clustering in order to permit the extraction of neural fiber bundles. In our opinion, local tensor clustering provides a natural way of determining the border of a fiber bundle

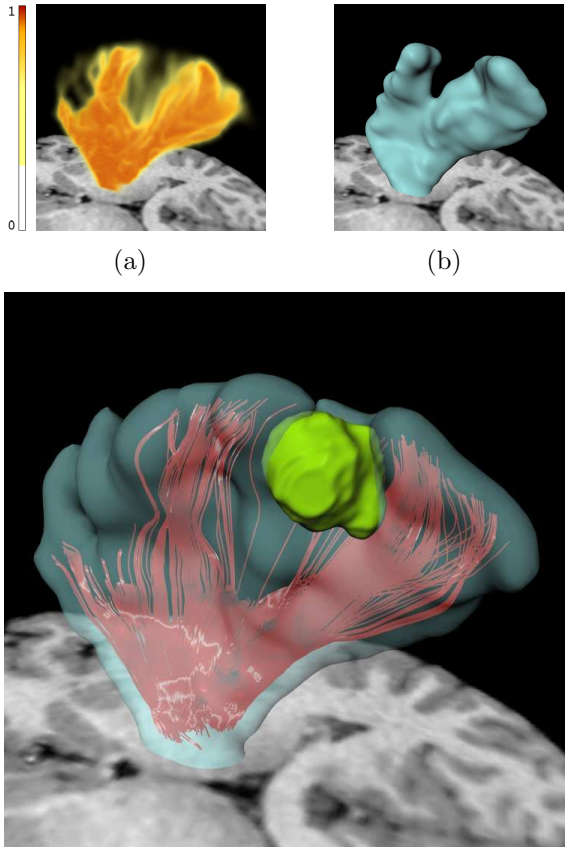

(a) (b)

(c)

Figure 3.11: (a) Tractogram of the right corticospinal tract of a patient with intracerebral metastases. It is difficult to determine an appropriate threshold to segment the tract. A slice of the T1 image is shown for anatomical reference. (b) Segmentation of the right corticospinal tract based solely on tensor clustering. Some areas of the tract are not captured. (c) Segmentation of the right corticospinal tract based on both the tractogram and tensor clustering. The red fibers are the result of deflection-based FT seeded within the internal capsule. The computed segmentation result is visualized as a semi-transparent hull around the tracked fibers. One of the metastases is shown in green. Whereas the FT fails to show that the tumor borders the corticospinal tract, this is made visible by the segmentation result in accordance with the tensor field data (see Fig. 3.13(a)). The parameters of the DTI acquisition sequence are as follows: resolution = $1.80 \times 1.80 \times 1.98$ mm^3, b value = 1000 s/mm^2, NEX = 2, TR/TE = 10700/80 ms, number of DW images = 62 (two b=0).

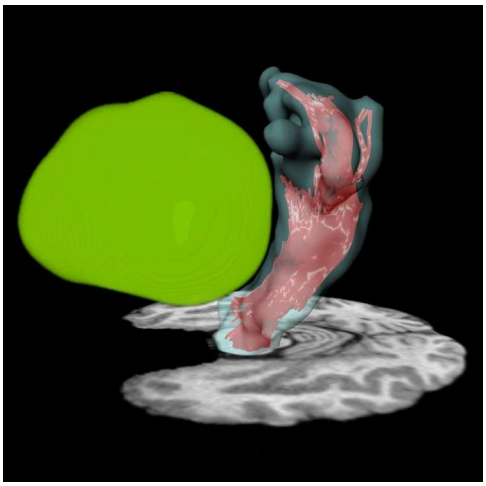

Figure 3.12: Segmentation of the right corticospinal tract of a patient with glioma. The red fibers are the result of deflection based FT seeded within the internal capsule. The computed segmentation result is visualized as a semi-transparent hull around the tracked fibers. The glioma is shown in green. The close distance between tumor and tract represented by the segmentation result is in accordance with the tensor field data (see Fig. 3.13(b)). The parameters of the DTI acquisition sequence are as follows: resolution = $1.80 \times 1.80 \times 1.98$ mm^3, b value = 1000 s/mm^2, NEX = 2, TR/TE = 10700/84 ms, number of DW images = 62 (two b=0).

whose general pathway is outlined by a connectivity map. To our knowledge, determining an optimal threshold parameter with which to extract fiber bundles from a connectivity map is a question that has not yet been fully answered. For this reason, we chose to employ non-parametric kernel density estimation to determine the connectivity values associated with the bundle. The optimal bandwidth was computed using the plug-in method presented by Raykar and Duraiswami [2005, 2006] and, in our experiments, quickly converged to values of approximately $\sigma = 0.1$. We have also experimented with using local, non-parametric PDF estimation on the manifold of symmetric matrices (similarly to Awate et al. [2007]) to perform local tensor clustering. Results were of similar quality but required the computation of an optimal bandwidth parameter at each voxel, greatly increasing the computational cost of the algorithm. Moreover, the computed optimal bandwidth parameters varied greatly among different voxels, so that it is not easy to find one bandwidth value which may be recommended for use over the whole image.

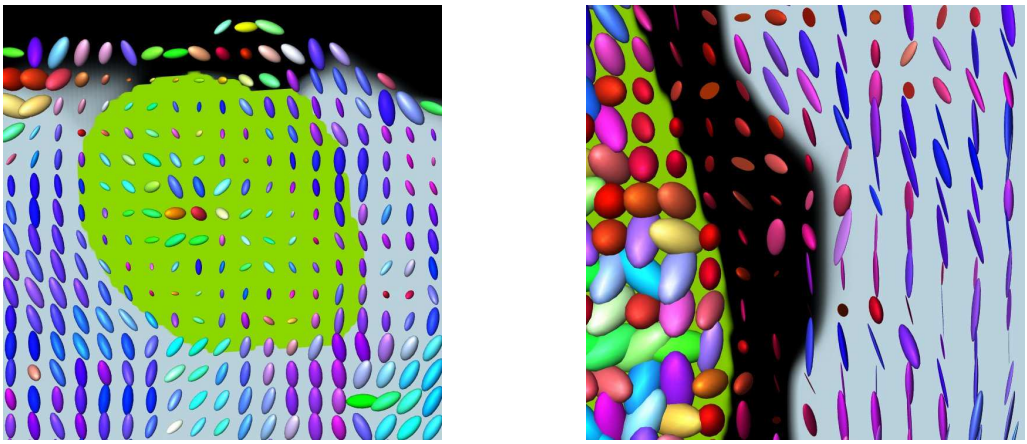

(a) (b)

Figure 3.13: (a) Sagittal slice detail of the case presented in Fig. 3.11. The metastasis segmentation is shown in green, and the corticospinal tract segmentation is shown in grey. The blue tensors (main diffusion direction along the z-axis) around the tumor indicate that the tract borders the tumor, which could not be detected via standard streamline tractography. (b) Sagittal slice detail of the case presented in Fig. 3.12. The red tensors (main diffusion direction along the x-axis) between the glioma and the segmented corticospinal tract indicate the presence of additional fiber bundles between tumor and tract, supporting the thesis that the glioma does not border the corticospinal tract.

The use of non-parametric PDF estimation makes the algorithm robust with respect to image noise, as demonstrated with our DTI phantom in Fig. 3.6. There is an apparent trend that DSCs increase when the cylinder radius becomes larger, which can be interpreted as using a higher and higher image resolution while keeping the radius of the bundle fixed. The algorithm also achieves good segmentation results with the two adjacent fiber bundles having an increasingly similar orientation. However, due to noise, tensors are increasingly misclassified, in particular those with partial-volume artifacts. The maximal distance between segmentation result and ground truth is below 2 mm when using more than 20 gradients (out of 30) to reconstruct the diffusion tensors, although other MR sequences optimized to reconstruct tensors with less than 30 gradients may lead to better results. There is a slight performance drop when the axis of the cylinder is not aligned with the z-axis. The most likely reason for this is the use of morphological regularization within our algorithm. This also leads to segmentation inaccuracies

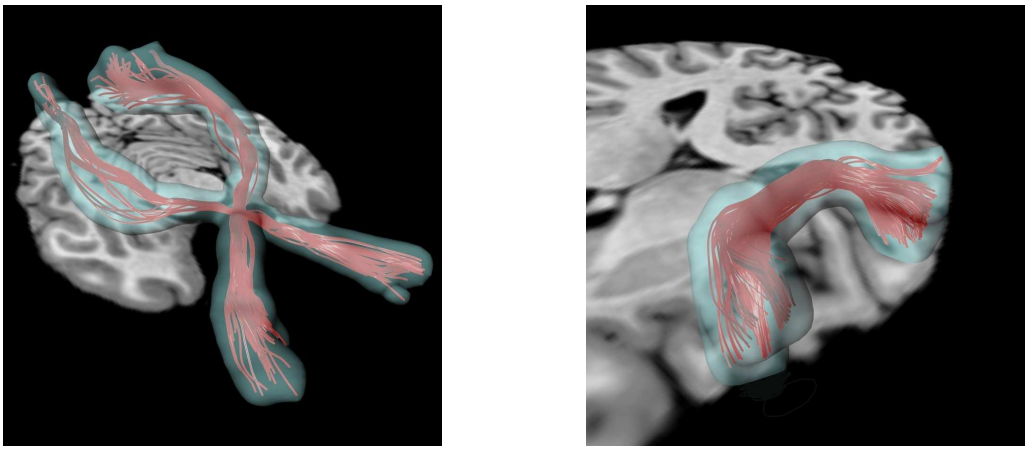

(a) (b)

Figure 3.14: Segmentation of the optic tract (a) and the arcuate fasciculus (b) of a healthy volunteer. The fibers are tracked by means of the global FT algorithm by Klein et al. [2012]. The computed segmentation result is visualized as a semi-transparent hull around the tracked fibers. The parameters of the DTI acquisition sequence are as follows: resolution = $1.80 \times 1.80 \times 1.98$ mm^3, b value = 1000 s/mm^2, NEX = 2, TR/TE = 12000/84 ms, number of DW images = 62 (two b=0).

at acute angles where fiber bundles cross, see Fig. 3.7(b). In the future, results may be improved with the use of a level-set based formulation and regularization. However, it is not immediately clear how a level-set formulation could be used without losing the fuzziness of the membership function m, an important aspect to compute c-means tensor clustering with high precision.

In Figs. 3.7 and 3.8 we illustrate the performance of our approach in the presence of fiber bundles crossing at different angles. In particular, Fig. 3.7(a) illustrates that a more accurate connectivity map is needed to resolve fibers crossing with a small angle of incidence (less or equal to 45°). If this angle is 70° or 90° the correct fiber path could be extracted. Additionally, Fig. 3.8 shows how the presented algorithm achieves superior segmentation results when compared to a pure tensor clustering or a pure connectivity map thresholding approach. As part of future work, we would like to analyze whether our method can be used to further improve tract extraction results produced by global fiber tracking techniques such as Fillard et al. [2009] or Reisert et al. [2010]. We may note, however, that although global approaches possibly offer a more precise reconstruction, the

current runtime of these approaches is still several hours, and therefore integration into the clinical routine is difficult. In a similar way, our algorithm could be used to correct for imprecision resulting from registering MR data to white matter parcellation atlases as described by Mori et al. [2008] or Zhang et al. [2009]. The registered volumes would need to be smoothed to simulate a "connectivity map".

Let us mention that the use of the presented software phantom is not restricted to DTI, but may also be used to fit multi-tensor or high angular resolution diffusion imaging (HARDI) data to the generated diffusion-weighted images. The extension of our segmentation algorithm to HARDI data should be straightforward. For example, the connectivity map may be computed as described by Descoteaux et al. [2009] and the distance between orientation distribution functions (ODFs) may be computed as illustrated by Descoteaux and Deriche [2009], i.e., by computing the Euclidean distance between the corresponding vectors of spherical harmonics coefficients.

In Fig. 3.9, we showed the reproducibility of segmentation results with several patient datasets. Compared to a similar study, when segmenting HARDI datasets presented by Descoteaux and Deriche [2009], our algorithm appears to more reliably segment the dominant diffusion paths starting from a seed ROI within the corticospinal tract. It is noticeable how lateral projections of the corticospinal tract are not captured by the algorithm. The problem may be addressed by using multiple seed ROIs, or by using different algorithms such as Jbabdi et al. [2007] or Sotiropoulos et al. [2010] to generate the connectivity map. In some subjects, parts of the anterior-posterior running superior longitudinal fasciculus are also reconstructed; this could be avoided via the use of additional exclude ROIs. It is important to stress that the quality of the segmentation result strongly depends on the quality of the underlying connectivity map.

Robustness with respect to the size of the local neighborhood is supported by the data presented in Fig. 3.10. Within a reasonable range, segmentation results present only small variations. Compared to Awate et al. [2007], the presented approach operates a truly local clustering and does not characterize each class by a set of tensors. Therefore, it performs well in capturing the variability of the data on the manifold of symmetric matrices. This is demonstrated by the many

segmentation examples computed on patient data and the direct analysis of the corresponding tensor field. Moreover, by using information from a connectivity map, our algorithm is able to capture groups of tensors that may be significantly different from the group of tensors used to initialize the segmentation. We also examined the efficiency of the algorithm and conclude that, although the computational cost is relatively high, the computation can be performed offline and requires no additional effort by the user when compared to standard streamline tractography. From a clinical perspective, we expect the algorithm to be particularly useful for glioma patients, because it could be used to precisely determine the distance between a specific tract and tumor even if edema or white matter infiltration occurs. A systematic evaluation of the algorithm on glioma patients will be part of future work.

We hope that this article will prompt further research into how information produced by connectivity maps and tensor clustering approaches can be integrated in a meaningful way to extract neural fiber bundles with a known maximal error.

Chapter 4

Atlas-Based Fiber Reconstruction from Diffusion Tensor MRI Data

This chapter of the thesis is based on the publication Barbieri et al. [2012b].

4.1 Abstract

Purpose: Develop a neural fiber reconstruction method based on diffusion tensor imaging which is not as sensitive to user-defined regions of interest as streamline tractography.
Methods: A simulated annealing approach is employed to find a non-rigid transformation to map a fiber bundle from a fiber atlas to another fiber bundle which minimizes a specific energy functional. The energy functional describes how well the transformed fiber bundle fits the patient's diffusion tensor data.
Results: The feasibility of the method is demonstrated on a diffusion tensor software phantom. We analyze the behavior of the algorithm with respect to image noise and number of iterations. First results on the datasets of patients are presented.
Conclusions: The described method maps fiber bundles based on diffusion tensor data and shows high robustness to image noise. Future developments of the

method should help simplify inter-subject comparisons of fiber bundles.

4.2 Introduction

Diffusion tensor imaging (see Basser et al. [1994b], Pierpaoli and Basser [1996]) is a magnetic resonance technique which measures the strength and direction of water molecule diffusion. Assuming that the main diffusion direction in an image voxel matches the average direction of the underlying fiber network, fiber tracking (FT) methods have been developed to reconstruct neural fiber bundles non-invasively and *in-vivo*. An overview of current tractography techniques can be found in Johansen-Berg and Behrens [2009]. Fiber tracking has increasingly gained acceptance as a pre- and intra-operative clinical tool used to determine, for example, positions of relevant neural tracts in relation to a tumor to be resected. In particular, streamline FT methods (Basser [1998], Mori et al. [1999]), which start from a given region of interest (ROI) and propagate streamlines along the main diffusion directions of the diffusion tensors, enjoy widespread clinical use. This is possibly due to their quick computation times and the deterministic outputs they produce. A drawback of this type of algorithm is that the tracking result can be very sensitive with respect to the location and size of the starting ROIs chosen by the user (Hattingen et al. [2009]). Once the tracking has been performed, additional ROIs are often needed to exclude false positive streamlines, resulting in extensive post-processing operations.

In recent years, several atlas-based fiber reconstruction methods have been proposed. They are generally less dependent on user defined ROIs than streamline FT. These atlas-based methods start by computing a group averaged diffusion tensor image (DTI) which is then segmented to generate a parcellation map. Lawes et al. [2008] determine anatomical labels of cortex regions, manually at first and then in a refined manner via streamline tractography. Tract reconstruction is achieved by mapping the anatomical labels onto a patient's DTI and determining all streamlines with specific start and end regions. In Mori et al. [2008], a white matter parcellation map (WMPM) is constructed by manually segmenting several tracts of interest based on the underlying color-coded orientation map. It is suggested that the WMPM can be registered to a patient's dataset

to either automatically determine the location of specific tracts or as a reference for manual ROI-based segmentation. In Yushkevich et al. [2008]; Zhang et al. [2009], streamline FT is employed on the averaged DTI, which is then registered onto the patient's DTI. For tract reconstruction, the registration transformation is applied to a binary mask derived from the tracked fibers.

In this work, we propose to start from a precomputed atlas of fiber bundles which are mapped onto the DTI data of the patient. In our opinion, focusing on mapping specific fiber bundles instead of a whole DTI should lead to computationally less expensive shape-consistent reconstructions. No post processing operations are needed once a fiber bundle has been "registered". Details about the suggested algorithm can be found in Section 4.3. Results of both synthetic and patient data are presented in Section 4.4. Current limitations and possible future improvements of the method are discussed in Section 4.5.

4.3 Methods

We now describe the proposed reconstruction approach. An overview of the algorithm and of how the individual steps are combined is presented in Algorithm 1.

4.3.1 Fiber Representation

In this article a "fiber bundle" F denotes a set of m fibers $\{f_j\}_{j=1,\dots,m}$. We represent a fiber f_j as a tuple of n_j points:

$$f_j = (P_{1_j}, P_{2_j}, P_{3_j}, \dots, P_{n_j}) \tag{4.1}$$

where P_{1_j} is the starting point of f_j and P_{n_j} its endpoint. Each fiber point is connected linearly to the next. Thus, we may associate a vector $\overrightarrow{v_{i_j}}$ to each fiber point P_{i_j} (but the endpoint), defined as

$$\vec{v_{i_j}} = P_{i+1_j} - P_{i_j} \text{ for } 1 \leq j \leq m, \text{ for } 1 \leq i < n_j\,. \tag{4.2}$$

Without loss of generality, we shall assume in the following that the distance between fiber points is constant. Whenever a transformation alters the distance

between points, fibers are linearly resampled to maintain the assumption's validity.

4.3.2 Fiber Atlas

Our fiber atlas consists of various tracked fiber bundles. The tracking was performed based on the DTI data (resolution = $1.80 \times 1.80 \times 1.98$ mm^3, b value = 1000 s/mm^2, TR/TE = 12000/84 ms, two repetitions with one b=0 image and 30 gradient directions each) of a single healthy volunteer using the global approach by Klein et al. [2012]. The tracked bundles include the arcuate fasciculus, the visual pathways, and fibers of the corticospinal tract originating from the hip, leg, hand, and face areas of the primary motor cortex (PMC).

4.3.3 Energy Functional

Consider a fiber bundle F from the fiber atlas and the diffusion tensor image $I : R^3 \rightarrow S^+(3, \mathbb{R})$, where $S^+(3, \mathbb{R})$ is the six-dimensional Riemannian manifold of 3×3 real symmetric positive-definite matrices. Our goal is to find a mapping Γ from a fiber bundle F to another fiber bundle $\Gamma(F)$ which minimizes a specific energy functional $E(\Gamma(F), I)$. In this work the mapping Γ preserves the number of tracked fibers but not necessarily their length (which, after resampling, corresponds to the number of points that define the individual fibers). The energy functional measures the match between the transformed fiber bundle and the main diffusion directions at the corresponding locations. It is defined as follows:

$$E(\Gamma(F), I) = \sum_{j=1}^{m} \frac{\sum_{i=1}^{n_j - 1} \left(- \log \left(\vec{v_{i_j}}^T I(P_{i_j}) \vec{v_{i_j}} \right) \right)}{n_j - 1} \tag{4.3}$$

where ^{T} indicates the transpose operation, n_j indicates the number of points which define the j-th fiber and $I(P_i)$ is determined via nearest-neighbor interpolation. The energy functional is normalized with respect to the total number of fiber points.

In regions where two fiber bundles cross, diffusion tensors are generally disc-

shaped. As no main diffusion direction is defined within this region, a minimization of the energy functional will not favor fibers running in a specific direction. Instead, the path of the mapped fiber bundle will be determined by the smoothness constraint imposed on the mapping Γ and by the main diffusion directions in regions adjacent to the fiber crossing. The same holds for a region infiltrated by a tumor and characterized by isotropic diffusion. However, the registration result is also influenced by the mean diffusivity in this region. If the mean diffusivity is high, a minimization of the energy functional will lead to fibers that go through the infiltrated region. If the mean diffusivity is low, fibers will bend around the tumor. Therefore, if the user is confident that fibers do not pass through a specific lesion (e.g., in the case of a metastasis), it may be useful to explicitly force fibers to bend around the lesion by weighting the corresponding diffusion tensors so that their mean diffusivity is decreased.

4.3.4 Simulated Annealing

To minimize the energy functional defined in Equation 4.3, we employ a strategy based on simulated annealing. Simulated annealing (Kirkpatrick et al. [1983]; Černý [1985]) is a probabilistic metaheuristic: it iteratively adds a random perturbation to a given initial state. The decision to move to the new state depends on whether this state corresponds to a lower energy level or not and on the value of an artificial temperature variable $\mathcal{T}$ which decreases with each iteration. When the temperature is high, the decision to move to the new state is almost random; when the temperature decreases, "downhill" moves are increasingly favored. The main advantage of simulating annealing compared to "greedy" algorithms is that it is relatively robust with respect to solutions being trapped in local minima.

Depending on the fiber bundle to be reconstructed, we choose the corresponding tract from the fiber atlas and manually register it onto the patient's diffusion tensor image. During the manual registration process, we allow for the bundle to be translated, scaled, and rotated. The result is used as the initial state of the simulated annealing approach.

4.3.4.1 Candidate Generation

Next, we illustrate how the current state is perturbed during the simulated annealing process. Similarly to the initial manual registration step, we apply a combination of translation, scaling, and rotation to the current fiber bundle. However, within the suggested approach, these operations do not necessarily act globally on the whole fiber bundle, but may also have a "local" effect on it, depending on a scale parameter σ_{scale}. The concatenation of "local" linear operations ultimately results in a non-rigid deformation of the original bundle from the fiber atlas. To apply one of the mentioned linear operations to the current fiber bundle, we start by randomly selecting (according to a uniform distribution) one fiber point, which we shall denote by P_{center_j} for a fixed j. This point corresponds to the location along the j-th fiber of the bundle, where the effect of the local transformation is the strongest. The transformation of the remaining points of the j-th fiber is computed depending on the points' distances to P_{center_j}. To compute a coherent transformation along the whole bundle, we determine the point which lies closest to P_{center_j} for each fiber. We thus obtain a center point for each fiber of the bundle and may assign a weight w_{i_j} to each fiber point. This weight determines the strength of the transformation at the point and is computed as follows:

$$w_{i_j} = \frac{\mathcal{G}(P_{i_j}, P_{\text{center}_j}, \sigma_{\text{scale}})}{\mathcal{G}(P_{\text{center}_j}, P_{\text{center}_j}, \sigma_{\text{scale}})} \text{ for } 1 \leq j \leq m, \text{ for } 1 \leq i \leq n_j \tag{4.4}$$

where $\mathcal{G}(\cdot, \mu, \sigma)$ denotes a Gaussian function with mean μ and standard deviation σ. The following sections detail how the single transformations are applied to the bundle.

Translation. The random translation magnitude $\vec{t}$ is sampled from the 3-D Gaussian distribution $\mathcal{N}(\cdot, \vec{0}, \sigma_{\text{translation}})$. The parameter $\sigma_{\text{translation}}$ reflects the expected magnitude. The translated points are determined according to

$$P'_{i_j} = P_{i_j} + w_{i_j} \cdot \vec{t} \tag{4.5}$$

Examples of global and local translations are displayed in Figs. 4.1(a) and 4.1(d).

Scaling. The random scaling magnitude $\vec{s}$ is sampled from the 3-D Gaussian

distribution $\mathcal{N}(\cdot, \vec{1}, \sigma_{\text{scaling}})$. The parameter σ_{scaling} reflects the expected magnitude. The scaled points are determined in two steps. First, the scaling is applied to the vectors $\vec{v}_{i_j}$:

$$\vec{v}'_{i_j} = w_{i_j} \cdot \vec{s} * \vec{v}_{i_j} \tag{4.6}$$

where $*$ indicates the component-wise vector product. Next, the new position of the fiber points is determined via

$$P'_{i_j} = \begin{cases} P_{\text{center}_j} - \sum_{i'_j=i_j}^{\text{center}_j - 1} \vec{v}'_{i'_j} & \text{if } i_j \leq \text{center}_j \\ P_{\text{center}_j} + \sum_{i'_j=i_j}^{\text{center}_j} \vec{v}'_{i'_j} & \text{else} \end{cases} \tag{4.7}$$

Examples of global and local scalings are displayed in Figs. 4.1(b) and 4.1(e).

Rotation. The random rotation angle $\vec{r}$ is sampled from the 3-D Gaussian distribution $\mathcal{N}(\cdot, \vec{0}, \sigma_{\text{rotation}})$. The parameter σ_{rotation} reflects the expected magnitude of the rotation angles. The components of $\vec{r}$ represent the angles of rotation around the x-,y-, and z-axes, we weight them by w_{i_j} and determine the corresponding rotation matrices R_x,R_y, and R_z at each fiber point. The rotated points are again determined in two steps. First, the rotation is applied to the vectors v_{i_j}:

$$\vec{v}'_{i_j} = R_x(w_{i_j} r_1)\, R_y(w_{i_j} r_2)\, R_z(w_{i_j} r_3)\, \vec{v}_{i_j} \tag{4.8}$$

Similar to the scaling transformation, the new positions of the fiber points are then determined according to Equation 4.7. Examples of global and local rotations are displayed in Figs. 4.1(c) and 4.1(f).

4.3.4.2 Cooling Schedule and Acceptance Probabilities

Denote the current iteration by *iter* and the maximum iteration number by $iter_{\max}$. The perturbed fiber bundle $\Gamma(F)$ corresponds to a new energy E_{new}. We keep track of the fiber bundle F_{best} corresponding to the overall lowest energy E_{best}. The current temperature $\mathcal{T}$ is computed as

$$\mathcal{T}(iter) = \exp\left(-10 \frac{iter}{iter_{\max}}\right). \tag{4.9}$$

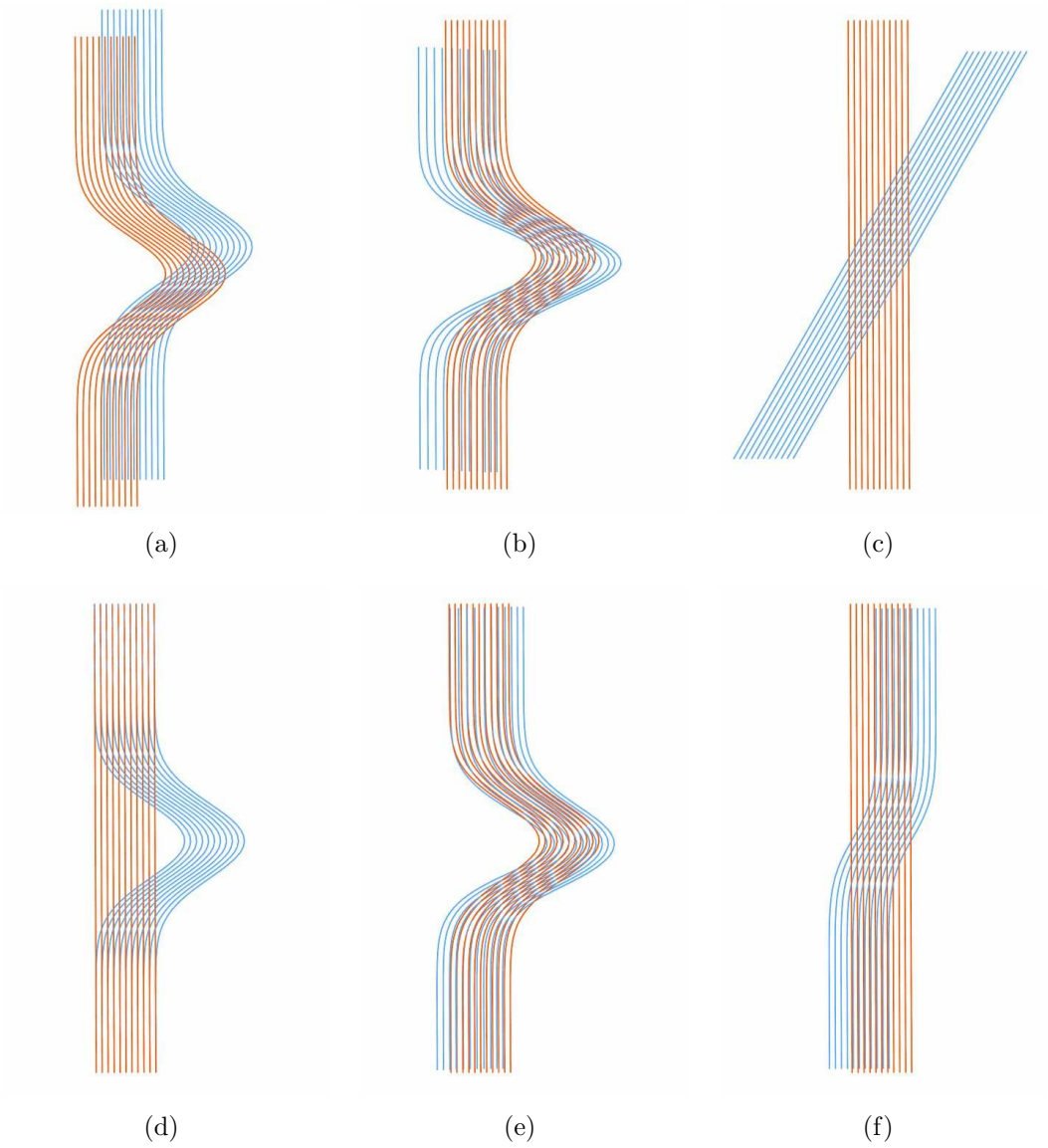

Figure 4.1: Various transformations applied to an original fiber bundle displayed in orange. The result of the transformation is displayed in light blue. The length of the straight orange bundle in Fig. (d) is 80 mm, and the spacing between fibers is 1 mm. The top row shows global transformations, while the bottom row shows local transformations with $\sigma_{\text{scale}} = 40$ mm. In detail: (a) Global translation using $\vec{t} = (4.5, 4.5, 0)$ mm. (b) Global scaling using $\vec{s} = (1.4, 0.9, 0)$. (c) Global rotation using $\vec{r} = (0, 0, -30)°$. (d) Local translation using $\vec{t} = (15, 0, 0)$ mm. (e) Local scaling using $\vec{s} = (1.4, 0.9, 0)$. The transformation is centered where the fibers bend to the right. (f) Local rotation using $\vec{r} = (0, 0, -30)°$.

The corresponding cooling schedule is illustrated in Fig. 4.2. The probability p

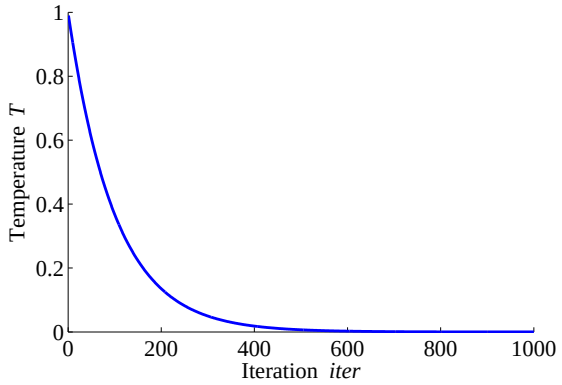

Figure 4.2: The employed cooling schedule computed according to Equation 4.9. In this example, $iter_{\max} = 1000$.

of moving to the new state is computed as

$$p(\mathcal{T}) = \exp\left(\frac{E_{\text{old}} - E_{\text{new}}}{\mathcal{T}}\right) . \tag{4.10}$$

If a random number r sampled from a uniform distribution over the interval $[0, 1]$ is smaller than p, the algorithm moves to the new state. Therefore, while the cooling process takes place, the likelihood of moving to a state which corresponds to a higher energy decreases. We always move to the new state if $E_{\text{new}} < E_{\text{old}}$. The simulated annealing process is repeated in a coarse-to-fine manner by using scale parameters of decreasing value $\sigma_{\text{scale big}}, \ldots, \sigma_{\text{scale small}}$.

4.3.5 Optional Transformation Restrictions

We mentioned that the initial state of the simulated annealing approach is given by a manual registration of the fiber bundle from the atlas onto the diffusion tensor image of the patient. Our confidence in the exactness of the manual registration result is likely to vary depending on the considered fiber tract and brain region. Where the manual registration result is believed to be correct, we may limit the effect of the transformation Γ on the current state F: the new state is given by F within user-defined ROIs, whereas we smoothly transition to $\Gamma(F)$ when moving away from these ROIs. For example, when reconstructing the

Algorithm 1 Algorithm for atlas- and DTI-based fiber reconstruction

Require: the relevant fiber bundle F from the fiber atlas
Require: maximum iteration number $iter_{\max}$
Require: scale parameters $[\sigma_{\text{scale big}}, \ldots, \sigma_{\text{scale small}}]$
Require: transformation magnitude parameters $\sigma_{\text{translation}}$, σ_{scaling}, σ_{rotation}
{**Algorithm Start**}
{*Initialization*}
perform manual affine registration of F onto I
$F_{\text{best}} \leftarrow F$
$E_{\text{old}} \leftarrow E(F, I)$
$E_{\text{best}} \leftarrow E(F, I)$
{*Reconstruction Step*}
for $\sigma_{\text{scale}} \in [\sigma_{\text{scale big}}, \ldots, \sigma_{\text{scale small}}]$ **do**
  for $iter = 1 \rightarrow iter_{\max}$ **do**
    select a transformation Γ between translation, scaling, and rotation
    compute $\Gamma(F)$ according to Section 4.3.4.1
    resample $\Gamma(F)$ with equidistant fiber points
    {*Compute corresponding energy*}
    $E_{\text{new}} \leftarrow E(\Gamma(F), I)$
    {*Decide whether to move to the new state*}
    select random r from uniform distribution over $[0, 1]$
    compute temperature $\mathcal{T}$ according to Eq. 4.9
    compute probability $p(\mathcal{T})$ according to Eq. 4.10
    if $r < p$ **then**
      $F \leftarrow \Gamma(F)$
      $E_{\text{old}} \leftarrow E_{\text{new}}$
      {*Check whether it is the best*}
      if $E_{\text{new}} < E_{\text{best}}$ **then**
        $F_{\text{best}} \leftarrow \Gamma(F)$
        $E_{\text{best}} \leftarrow E_{\text{new}}$
      end if
    end if
  end for
end for
return F_{best}
{**Algorithm End**}

corticospinal tract, we keep the manual registration result within the brainstem, or when reconstructing the visual pathways, we are generally able to locate the optic chiasm and therefore do not allow transformations in this region.

4.4 Results

We start by testing our algorithm on a DTI software phantom. The dataset is generated using control points and cubic spline interpolation as described by Barbieri et al. [2011b] and takes into account partial-volume artifacts between tensors. As suggested by Hahn et al. [2006], we simulate Rician distributed image noise by computing $|I_{\mathrm{DW}} + \tilde{N}(0, \sigma_{\mathrm{noise}})|$, where I_{DW} is the diffusion-weighted signal and $\tilde{N}(0, \sigma_{\mathrm{noise}})$ is a Gaussian-distributed complex variable with mean 0 and standard deviation σ_{noise}. Using standard fitting procedures, we compute the tensor-valued image based on the diffusion-weighted images. Table 4.1 reports the default parameters used to generate the DTI software phantom and to reconstruct the fiber bundle. Fig. 4.3 shows slices of the synthetic dataset in which the x-,y-, and z-components of the main diffusion direction have been mapped to red, green, and blue (RGB) color values, respectively. Figs. 4.3(a)-4.3(d) show various stages of the fiber reconstruction process. In Fig. 4.3(e), a second fiber bundle has been added to the synthetic dataset, resulting in a region of disc-shaped tensors where the fibers cross. Due to noise, the main diffusion direction in this region is basically random. The reconstruction result is very similar to the previous one-bundle example, indicating robustness of the algorithm with respect to fiber crossings. Fig. 4.3(f) shows a simulation of a tumor which is characterized by a low mean diffusivity and cuts into the synthetic fiber bundle.

In Fig. 4.4(a), we report the lowest energy values E_{best} determined when reconstructing the fiber bundle with different levels of image noise. The standard deviation of the noise varies between 0 and 5.5 by increments of 0.5 (corresponding SNR between $+\infty$ and approximately 13), and for each standard deviation value, the reconstruction is repeated 10 times. The initial energy is approximately 0.3 for all experiments. In Fig. 4.4(b), we similarly vary the number of iterations used to reconstruct the fiber bundle. These range from 25 to 300 by increments of 25.

Next, we consider the diffusion tensor images of two patients. These datasets are publicly available from IEEE Visualization Contest 2010. The parameters of the DTI acquisition sequence for the first patient are as follows: resolution = $1.80 \times 1.80 \times 1.98$ mm^3, b value = 1000 s/mm^2, NEX = 2, TR/TE = 10700/80 ms, two repetitions with one b=0 image and 30 gradient directions each. The same parameters are used for the second patient but with TE=84 ms. The first patient is affected by intra-cerebral metastases. Reconstructions of part of the right corticospinal tract, of the visual pathways, and of the left arcuate fasciculus are presented in Fig. 4.5. Fig. 4.6 supports the claim that the transformed corticospinal tract better matches the underlying tensor data. The second patient is affected by a glioma. In Fig. 4.7, the part of the corticospinal tract originating from the hip and leg area of the PCM has been reconstructed and is compared to a streamline tractography result seeded within the internal capsule.

	Default value
noise standard deviation	2.5 (SNR=28)
radius of the bundle	13 mm
number of gradients	30
voxel size	$1\times1\times1$ mm^3
b value	1000 s/mm^2
noise-free $b = 0$ intensity	70
maximum iteration number	300
transformation scales	$[640, 320, 160, 80, 40]$ mm

Table 4.1: Default parameters used to generate the DTI software phantom and to reconstruct the fiber bundle.

4.5 Discussion

We developed a method to map fiber bundles from a fiber atlas onto the DTI dataset of a patient. To the best of our knowledge, it is the first method to solve this specific problem. In the presented experiments, we start by performing a manual affine registration of the fiber bundles from the fiber atlas onto the DTI dataset of a patient. This step may be simplified in the future by employing

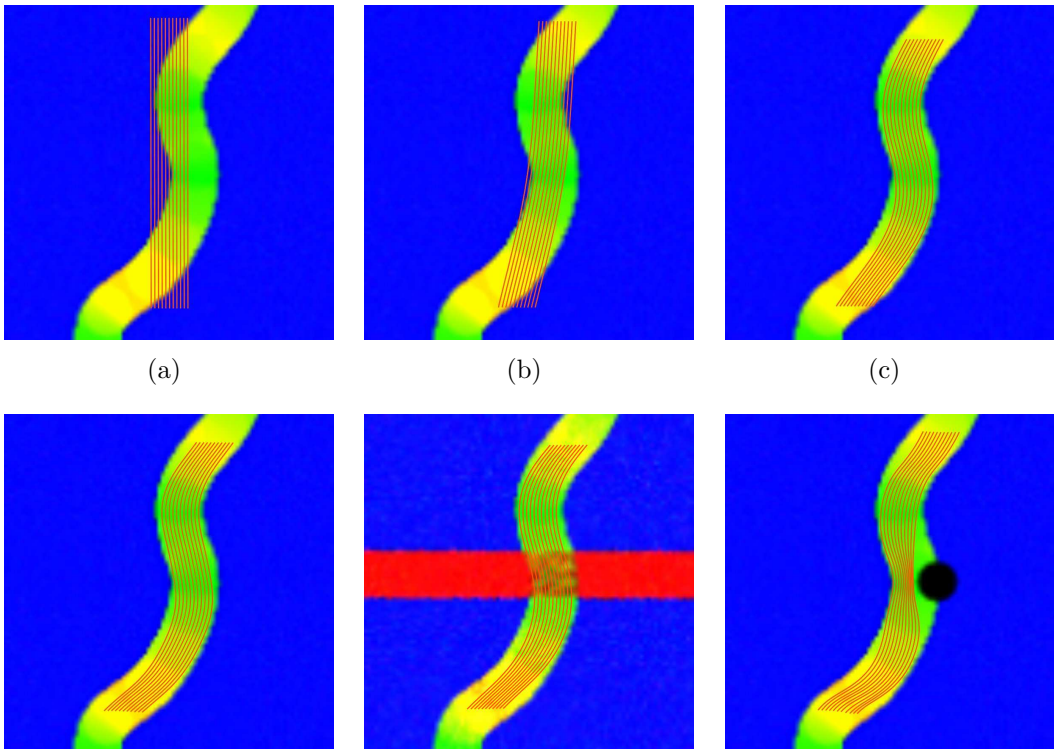

Figure 4.3: Reconstruction of a synthetic fiber bundle. The size of the image is $100 \times 100 \times 40$ mm^3. (a) shows the fiber bundle initialization and a color-coding of the main diffusion directions of the tensor field. (b), (c) and (d) show subsequent reconstruction results after setting $\sigma_{\text{scale}} = 640$ mm, $\sigma_{\text{scale}} = 320$ mm, and $\sigma_{\text{scale}} = 40$ mm, respectively. (e) shows the reconstruction result after a crossing fiber bundle has been added to the synthetic dataset. In (f), a tumor which cuts into the synthetic fiber bundle has been simulated.

automatic brain registration methods such as the one by Han and Park [2004]. Next, in Equation 4.3, we formulate an energy functional to be minimized via a simulated annealing procedure. The energy value corresponds to how well the transformed fiber bundle fits the underlying tensor data. Tensor values along the streamlines are so far determined by using nearest neighbor interpolation, although a future improvement could include linear or log-Euclidean (Arsigny et al. [2006]) interpolation of the tensor data. Our approach operates in a multi-scale manner: it starts by applying global linear transformations to the fiber bundle, followed by more and more local transformations. The possibility of choosing the

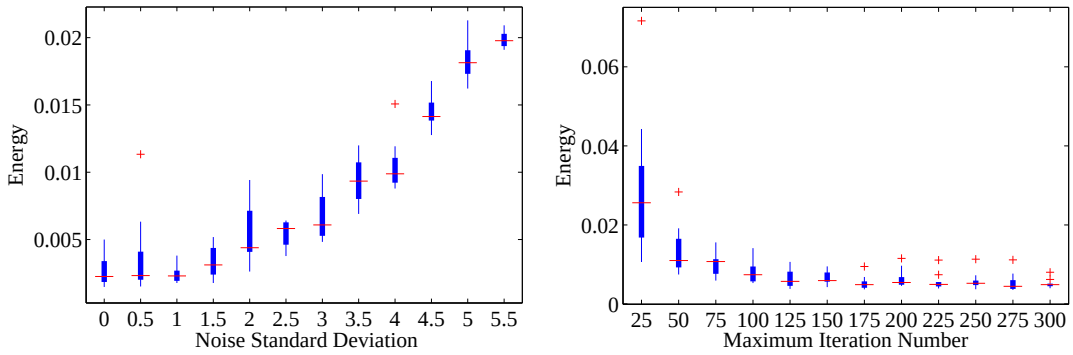

Figure 4.4: Values of the lowest energy value E_{best} versus the standard deviation of the noise corrupting the DTI software phantom (a) and versus the maximum iteration number (b). The initial energy is approximately 0.3 for all experiments. The default parameters used to generate the phantom are reported in Table 4.1.

various transformation scales allows an elastic "registration" without running into over-fitting problems. Currently we perform a fixed number of iterations for each spatial scale. For future improvement, the computation time may be reduced by advancing to the next spatial scale when the energy decrease between successive iterations is smaller than a predefined threshold. Also, the possibility of simulating multiple cooldowns (instead of only one) at each spatial scale may be investigated. The final (backward) transformation of the fiber bundle from the atlas to the patient is given by a concatenation of linear operations applied to the fiber points and the line segments connecting them. Therefore, the inverse (forward) transformation from the patient to the atlas can be readily obtained if we track the center, scale, and type of applied transformations. Some inaccuracies in the forward transformation may arise due to the resampling, which keeps the distance between fiber points constant.

Fig. 4.3 illustrates the ability of the algorithm to deal with regions of low anisotropy (from either a fiber crossing or an infiltrating tumor) or with a tumor region where diffusion is low. When dealing with a non-infiltrating tumor (such as a metastasis), better results may be obtained by weighting the diffusion tensors by their fractional anisotropy so that regions of low anisotropy are severely penalized by the energy functional. In Fig. 4.4 we analyze the performance of the suggested approach on synthetic data when varying the level of image noise

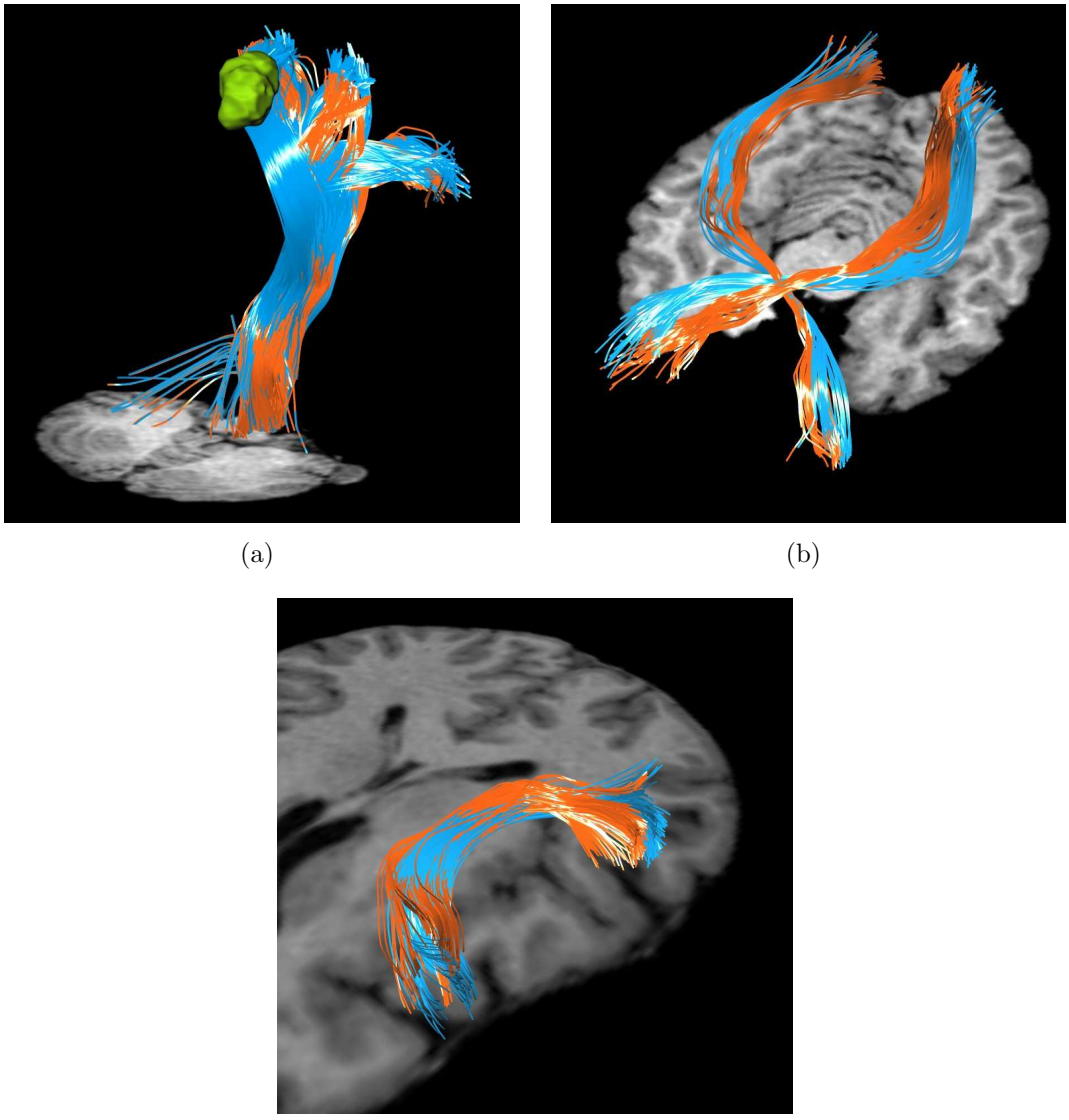

(a) (b)

(c)

Figure 4.5: Reconstructions of the corticospinal tract (a) (hip and leg, hand, and face areas of the PMC), of the visual pathways (b), and of the arcuate fasciculus (c) of a patient with intra-cerebral metastases. The original fiber bundles from the fiber atlas are displayed in orange, while the transformed bundles are displayed in light blue. One of the metastases is shown in green.

and the number of iterations. Because the energy functional is computed globally on the whole fiber bundle, as expected the algorithm performs well also in the presence of considerable image noise. Approximately 150 iterations appear

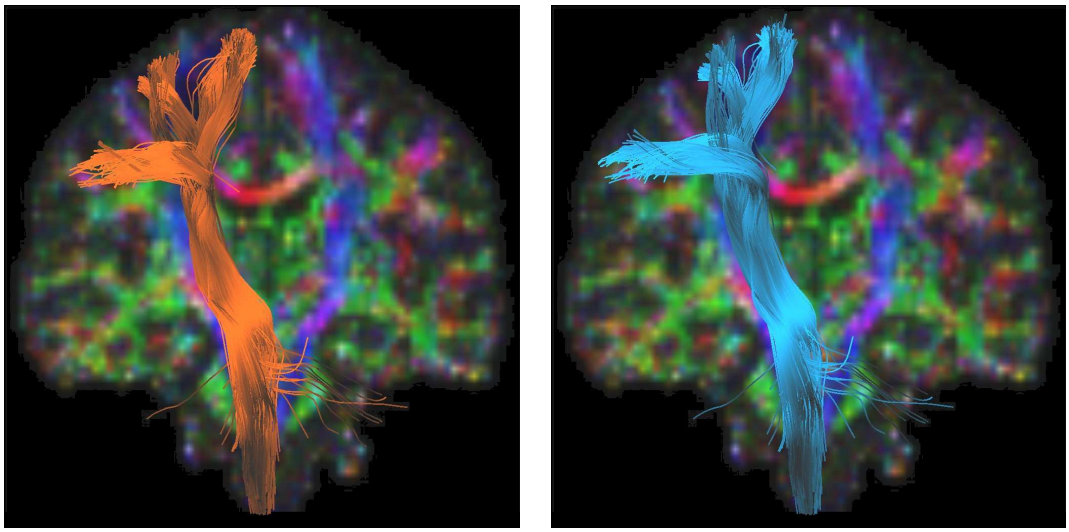

(a) (b)

Figure 4.6: The corticospinal fibers presented in Fig. 4.5(a) are displayed on top of the color-coded diffusion tensor image before (a) and after (b) transformation.

to be sufficient to reconstruct the fiber bundle on the given synthetic data. In Figs. 4.5 and 4.6, we present first reconstructions of the corticospinal tract, visual pathways, and arcuate fasciculus of a patient with intra-cerebral metastases. The visual pathways have been reconstructed simultaneously. If the user is interested in the simultaneous mapping of fiber bundles which vary considerably in size, it should be reasonable to weight the contributions to the energy functional according to the size of the bundles. Otherwise, large-scale transformations which provide a good fit for the larger bundles but not for the smaller bundles could be accepted. Compared to streamline tractography approaches such as Basser [1998] and Mori et al. [1999], the suggested approach does not require the user to define seed- or exclude-ROIs. However, we make use of ROIs to reduce the search space of possible transformations and reduce the risk of the simulated annealing approach terminating in a local minimum. Fig. 4.7 illustrates the reconstruction of a corticospinal tract considerably displaced by a glioma by means of our method. Visually the result is comparable to a reconstruction obtained by means of streamline FT seeded within the internal capsule.

The approach by Lawes et al. [2008] automatically determines the anatomical regions of the cortex to be used as start and end ROIs. This also leads their

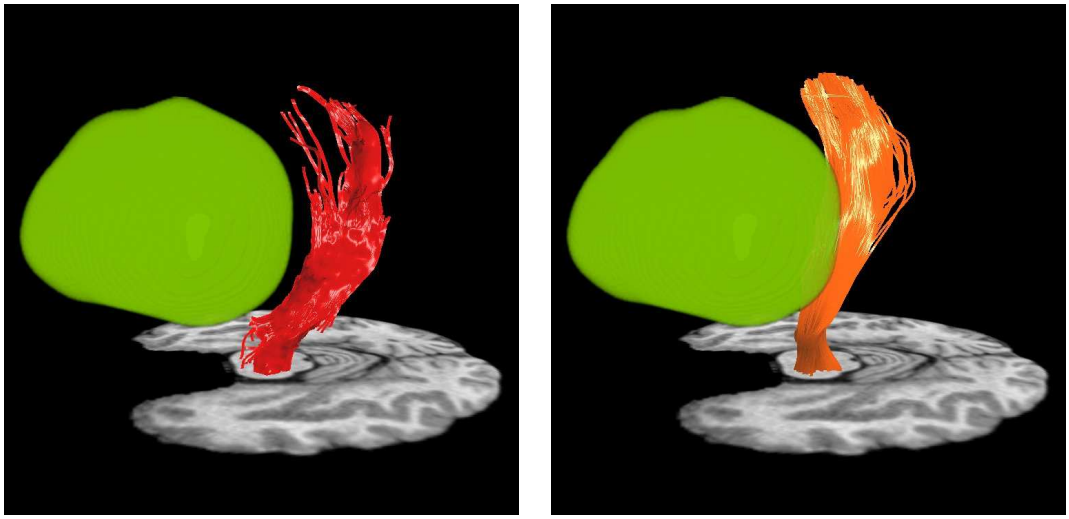

(a)

(b)

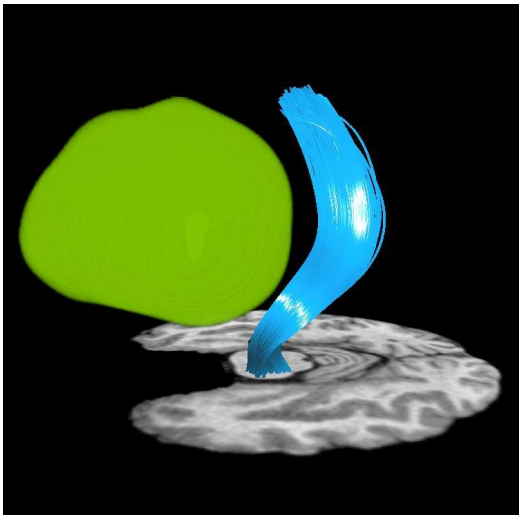

(c)

Figure 4.7: (a) Reconstruction of the dominant part of the right corticospinal tract of a patient with glioma by means of streamline FT seeded within the internal capsule. The glioma is shown in green. Reconstruction via the proposed method is illustrated in (b) and (c). The original fiber bundles from the fiber atlas are displayed in orange, while the transformed bundles are displayed in light blue.

algorithm to be sensitive to inter-subject variability, because boundaries between regions may not necessarily be in the same position in different individuals. By relying on streamline FT, additional ROIs may still be needed to resolve crossing

fibers or to eliminate fibers which continue into other pathways terminating into the same region. These operations are not needed with our algorithm. Mori et al. [2008] present a manually segmented white matter parcellation map which can be registered onto the DTI of a patient. Although very useful for anatomical orientation, the atlas can only provide a coarse fiber reconstruction, because often, only parts of fiber bundles could be delineated on the color-coded orientation map. In Yushkevich et al. [2008]; Zhang et al. [2009], a DTI atlas is registered onto the DTI of a patient together with the binary mask derived from tracked streamlines. This appears to be a viable alternative for tract reconstruction without the need of user defined ROIs, however, it is restricted to non-branching sheet-like structures that can be effectively modeled by medial representations and may not be adequate to reconstruct fiber bundles which are considerably displaced due to lesions. Comparing the computational expense, we expect our algorithm to be faster: while the reconstructions presented in this paper took approximately 30 minutes to compute using a single-threaded Matlab implementation, the elastic registration of DTIs can be computationally quite expensive (compare Barbieri et al. [2009]). Moreover, the effect of the transformation on the registered tensors poses a modeling challenge: while it is generally accepted that a rotation of the image leads to a rotation of the tensors (see Alexander et al. [2001]) it is not as clear what the effect of scaling or shearing the image should be. On the contrary, with our approach, we simply apply the transformation to the streamline defining points and interpolate them accordingly.

The employed fiber atlas is based on the data of a single subject. It would be interesting to create fiber atlases based on the tracked fiber bundles of multiple subjects, possibly grouped according to specific diseases. These atlases could consist either of averaged fiber bundles (the fiber bundle minimizing one of the distances between fiber bundles suggested by Jiao et al. [2010] could be determined) or of a map indicating the probability of a tract being in a specific location. With the latter option, a fiber tract could be reconstructed by considering its likelihood and the agreement of its trajectory with the diffusion data. The flexibility of the suggested approach could be increased by allowing the generation and the removal of streamlines. This would lead to a fiber tracking algorithm based on global optimization, related to the work by Fillard et al. [2011] and Reisert et al.

[2010], but without needing to generate fibers from a "soup of fragments", because prior knowledge about the expected shape of fibers can be incorporated. A preliminary step in this direction would probably consist in reformulating the problem in a continuous framework which starts from the definition of a streamline (a line whose tangent is always parallel to the vector field) and where the energy term considers both how well a streamline fits the underlying tensor data and how distant the streamline is from the atlas bundle. In the short term, if there is a considerable difference between the fiber bundles of the atlas and the patient, a landmark-based, thin-plate spline registration (Rohr [2001]) could be used to initialize the simulated annealing process. Future work will also focus on applying the proposed method to High Angular Resolution Diffusion Imaging (HARDI, see [Johansen-Berg and Behrens, 2009, Chapter 4] for an overview), where in each voxel the probability that a diffusing water molecule moves in a particular direction is given by a probability density function sampled on the sphere. The energy functional will need to be modified to consider this probability (in the direction of the different vectors defining the streamlines) instead of the current vector norm defined by the diffusion tensor.

In conclusion, our hope is that this work may serve as a proof of concept for fiber reconstruction methods which map fiber bundles based on diffusion tensor data and which are not as sensitive to ROI placement as standard streamline tractography and will simplify inter-subject comparisons.

Chapter 5

Simulating Tumor Growth and Visualizing Fiber Tracking Uncertainty

This chapter of the thesis is partly based on the publication Barbieri et al. [2011a].

5.1 Abstract

In this work, different approaches to determine fiber tracking uncertainties are compared to one another by color-coding the traced streamlines and by computing individual "confidence hulls". The considered visualization techniques may be used to make the user aware of local uncertainties in the fiber reconstruction process, to reflect the quality of the underlying diffusion tensor data, or to explore the sensitivity of the result with respect to different tracking parameters. We are particularly interested in the accuracy of fiber tracking in the vicinity of tissue infiltrated by a tumor. To analyze this scenario, we simulate the growth of glioblastomas multiforme, taking into account both the varying volume of the tumor and its mechanical interaction with the brain parenchyma. Since these tumors grow preferentially along white matter fiber bundles, a tumor-invaded diffusion tensor field is simulated at the different stages of tumor development.

5.2 Introduction

Diffusion Tensor Imaging (DTI) models the anisotropic diffusion of water molecules as a 0-mean normal distribution, whose covariance matrix is proportional to the second order diffusion tensor (Basser et al. [1994b], Neil et al. [1998], Pierpaoli and Basser [1996]). In white matter we assume that the eigenvector associated with the largest eigenvalue of the tensor, i.e. the main diffusion direction, matches the direction of the underlying fiber bundles. Fiber tracking (FT) algorithms make use of this property to trace streamlines across the diffusion tensor field (Basser [1998], Mori et al. [1999], Parker et al. [2002]). Since for patient data the true extent of fiber bundles is unknown, software or hardware phantoms represent an important tool to analyze and validate FT algorithms (Fieremans et al. [2008], Gössl et al. [2002], Lori et al. [2002]).

FT algorithms generally stop the tracing of a streamline when the fractional anisotropy of a crossed diffusion tensor is below a specified threshold parameter. The choice of this threshold parameter may have a considerable impact on the result of the fiber reconstruction algorithm (Brecheisen et al. [2009]). In this work we visualize the uncertainty related to the choice of the FA threshold parameter in the specific case when the fiber bundle of interest is near a tumor. To this end, we make use of the DTI data of a healthy volunteer on which we simulate the growth of a glioblastoma multiforme (GBM), the most common primary brain tumor in adults (Price et al. [2003]). We model white matter infiltration as well as the deformation of brain parenchyma and determine the effects on the underlying tensor field. We then present two additional possibilities for color-coding the streamlines, which convey information about uncertainties related to the diffusion tensor data and to the fiber tracking algorithm. More in detail, the considered techniques are based upon an analysis of the "uncertainty cones" of the main diffusion directions and upon the confidence measure proposed in Chapter 4, which combines connectivity and tensor clustering information. Additionally, we determine individual "confidence hulls" around the reconstructed bundles, which in a neurosurgical context may help to decide how aggressively a tumor shall be resected.

5.2.1 Related Work

Several approaches have been proposed to mathematically describe the growth of tumors, which may be subdivided according to the spatial scale they operate on. A first class of algorithms simulates tumor growth at the cellular level (cellular automata), whereas a second class of algorithms predicts the evolution of tumor density at a macroscopic scale, generally by making use of partial differential equations (PDEs). Although cellular automata approaches have been proposed for different tumors including GBMs (see Dionysiou et al. [2006], Kansal et al. [2000a], Kansal et al. [2000b], Kansal et al. [2000c]) since we are interested in the macroscopic effects that tumor growth has on diffusion tensor images and not in the specific spatial ordering of tumor cells, we choose to focus on PDE based methods.

Among PDE based methods Li et al. [2007] suggest a model that accounts for cell-proliferation and apoptosis. Cristini et al. [2008] simulate the growth, neo-vascularization and infiltration of malignant gliomas. Clatz et al. [2004] take into account both white matter infiltration and the mechanical deformation of the invaded structures. The patient's T1 and T2 images are registered to the BrainWeb atlas (BrainWeb) to take into account tissue properties and to a DTI atlas to take into account the preferential growth direction of GBMs along white matter fibers (Price et al. [2003]). The approach subdivides the gross tumor volumes (GTVs, see Kantor et al. [2001]) into GTV1, the non-infiltrating component associated with volume increase and tissue deformation, and GTV2, the diffusion component associated with fast expansion and infiltration but smaller mass-effect.

We are especially interested in the effect of tumor growth on FT accuracy. In Tournier et al. [2002], Barbieri et al. [2011b] it has been shown using software phantoms that FT algorithms may consistently underestimate the spatial extent of fiber bundles with an error in the order of 5 mm. In Kinoshita et al. [2005] electrical stimulation was used in tumor patients to demonstrated that FT algorithms do not determine the correct size of fiber bundles. A theoretical limit to the accuracy of fiber tracking for diffusion data with a given signal to noise ratio has been determined via power series by Anderson [2001]. However, to the

best of our knowledge, few authors have addressed the problem of visualizing the uncertainty associated with fiber tracking. Jones [2003] suggested a method to compute the 95% confidence intervals in which the main diffusion directions lie and visualizes them as "uncertainty cones". A corresponding pointwise coding of the color and width of streamtubes has been presented in Jones et al. [2005].

In this paper we present an alternative visualization approach which color-codes the tracked fibers based on the 95% confidence intervals, inspired by the visualization work by Brecheisen et al. [2009] where streamlines are color-coded based upon common stopping criteria such as tensor anisotropy and fiber curvature.

5.2.2 Contributions

The main contributions of this paper may be summarized as follows:

- We adapt the model by Clatz et al. [2004], which couples two PDEs that describe the increase in tumor volume and the deformation of brain tissue, to simulate tumor growth in DTI data
- We use patient specific DTI data and white and grey matter segmentations to improve the accuracy of the simulation
- We compare an FA-based color-coding of streamlines at different stages of tumor development
- We suggest alternative ways to visualize fiber tracking uncertainty based on the confidence intervals in which the main diffusion directions lie and based on a combined connectivity map and tensor clustering approach
- We compute "confidence hulls" around the reconstructed fiber bundles which may help to decide how aggressively a tumor shall be resected

5.3 Methods

Our method to simulate GBM growth is based on the work presented by Clatz et al. [2004], which we adapt to obtain two coupled PDEs that describe the

effects that tumor invasion in the brain parenchyma and mechanical deformation of brain tissue (mass effect) have on a patient's DTI data. Based on the T1 data of a healthy subject, we begin by segmenting the white and grey matter regions via a watershed-based algorithm (Hahn et al. [2006]). Manual rigid registration is then used to align the T1 image and the segmented regions to the DTI data of the subject (specifically to the b=0 image).

5.3.1 Tumor Growth Model

In order create the artificial tumor, we start by initializing the normalized tumor cell density function $c : \Omega \to [0, 1]$ where Ω is the image domain. This function may be used to compute the true cell density in a voxel via multiplication with the carrying capacity constant $C_{\max}$, estimated to be approximately $3.5 \cdot 10^4$ cells/mm^3 (Cruywagen et al. [1995], Tracqui et al. [1995]). Given the center of the tumor x_0, we initialize c by computing

$$c(x) = \frac{1}{1 + \|x - x_0\|^2} \tag{5.1}$$

where $\|\cdot\|$ is the euclidean norm.

While the tumor grows, the evolution of the density function c may be described via the sum of an anisotropic diffusion term which depends on the diffusivity of the underlying tissue and a cell proliferation term:

$$\frac{\partial c}{\partial t} = \underbrace{\operatorname{div}(D\,\nabla c)}_{\text{anisotropic diffusion}} + \underbrace{\rho c}_{\text{source term}} . \tag{5.2}$$

Here D is the diffusion tensor reconstructed at each voxel and ρ is a parameter which depends on the aggressiveness of the tumor. In our experiments we set $\rho = 0.77/\text{day}$, which leads to the simulation of a very quickly growing tumor.

Via a second PDE we model the mechanical deformation of brain tissue caused by tumor growth:

$$\operatorname{div}(\sigma) - \gamma\,\nabla c = 0 \tag{5.3}$$

where σ is the stress tensor and γ is a scaling factor for the pressure applied on the

tissue by the growing tumor. The deformation force acts in the direction opposite to the gradient of the tumor density function. The stress tensor σ depends on the local displacement $u : \Omega \to \mathbb{R}^3$ and on the tissue dependent Lamé parameters λ and μ. In the brain regions where we allow for tissue displacement, i.e. white and grey matter, we use $\lambda = 991.43$ Pa and $\mu = 247.86$ Pa, which may be normalized to $\lambda = 1.0$ Pa and $\mu = 0.25$ Pa. The coupling factor γ is set to 1.0. We do not explicitly compute σ but solve instead the elastostatic equation, i.e. we find u such that all forces acting on the brain tissue sum up to zero. Assuming the tissue to be locally isotropic (the deformation magnitude does not depend on the direction of the applied force) and homogeneous the equilibrium equations may be explicitly derived (Slaughter [2002]):

$$\begin{aligned} 0 &= (\lambda+\mu)(u_{1_{xx}} + u_{2_{xy}} + u_{3_{xz}}) + \mu(u_{1_{xx}} + u_{1_{yy}} + u_{1_{zz}}) - \gamma c_x \\ 0 &= (\lambda+\mu)(u_{1_{xy}} + u_{2_{yy}} + u_{3_{yz}}) + \mu(u_{2_{xx}} + u_{2_{yy}} + u_{2_{zz}}) - \gamma c_y \\ 0 &= (\lambda+\mu)(u_{1_{xz}} + u_{2_{yz}} + u_{3_{zz}}) + \mu(u_{3_{xx}} + u_{3_{yy}} + u_{3_{zz}}) - \gamma c_z \end{aligned} \tag{5.4}$$

which may also be expressed in vector notation as

$$0 = (\lambda+\mu)\nabla(\nabla \cdot u) + \mu\nabla^2 u - \gamma\nabla c\,. \tag{5.5}$$

After introducing an artificial time variable T, Eq. 5.5 may be solved as the steady state in time of

$$\frac{\partial u}{\partial T} = (\lambda+\mu)\nabla(\nabla \cdot u) + \mu\nabla^2 u - \gamma\nabla c\,. \tag{5.6}$$

5.3.2 PDE Coupling and Discretization

We thus need to solve the coupled PDEs 5.2 and 5.6 with c and u set to 0 at the boundary of white and grey matter. We do this by approximating each partial derivative via finite differences and by employing an explicit gradient descent algorithm. For example, the time derivative in Eq. 5.2 will be approximated via

$$\frac{c^{i+1} - c^i}{\Delta t} = \mathrm{div}(D\,\nabla c) + \rho c \tag{5.7}$$

where i indicates the iteration number and Δt is the time step (we use $\Delta t = 0.2$ days). This leads to the iterative scheme

$$c^{i+1} = c^i + \Delta t \cdot (\mathrm{div}(D\,\nabla c) + \rho c)\,. \tag{5.8}$$

Equation 5.6 is solved analogously. In order to couple the two PDEs after each update to the tumor cell density function c we iteratively solve Eq. 5.6 to find the resulting displacement field and apply it to the diffusion tensor image. While doing this, we need to not only shift the single diffusion tensors according to u but also to appropriately reorient the main diffusion directions. The local transformation at position x is given by J_{x+u}, the Jacobi matrix of $x+u(x)$. The new tensor D^{i+1} at position $x + u(x)$ is then computed via

$$D^{i+1}(x + u(x)) = J_{x+u}\; D^i(x)\; J_{x+u}^{-1}\,. \tag{5.9}$$

This way, both the rotation and shearing of tensors are taken into account. However, it is unclear whether a local shearing of the diffusion tensor image should lead to a shearing of the single diffusion tensors. As tensor shearing leads to fractional anisotropy values which appear unrealistically high in white matter, in the following experiments we restrict the tensor transformation to rotation. We approximate J_{x+u} by means of the orthonormal matrix Q obtained via its QR decomposition (Francis [1961], Francis [1962], Kublanovskaya [1961]) and J_{x+u}^{-1} via the transpose of Q.

In Fig. 5.1 we present an illustrative example of the need for tensor reorientation in 2D. Consider applying the displacement field

$$u(x) = \begin{pmatrix} x_1 \cos\theta - x_2 \sin\theta - x_1 \\ x_1 \sin\theta + x_2 \cos\theta - x_2 \end{pmatrix} \tag{5.10}$$

(which correspond to a global counterclockwise rotation by an angle θ) to the tensor schematized in Fig. 5.1(a). Simply shifting the center of the tensor leads

to the configuration depicted in Fig. 5.1(b). Finally, since

$$J_{x+u} = \begin{pmatrix} \cos\theta & -\sin\theta \\ \sin\theta & \cos\theta \end{pmatrix}, \tag{5.11}$$

we rotate D according to Eq. 5.9 and obtain the result displayed in Fig. 5.1(c).

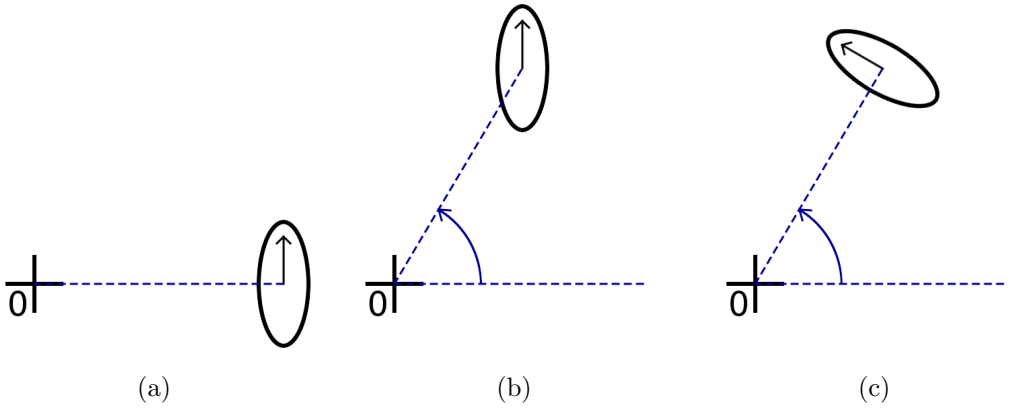

Figure 5.1: (a) Schematic initial tensor configuration. (b) Application of the displacement field to the tensor without reorientation of the main diffusion direction. (c) Reorientation of the tensor by means of the Jacobi matrix.

Once we have applied the displacement field to the diffusion tensors and reoriented them, many tensors will likely not be centered on the image grid and therefore we need to solve a scattered data interpolation problem (Amidror [2002], Crum et al. [2007]). For each voxel, we consider the set of displaced tensors $\{D_j\}$ with a distance d_j from the center x_o of the voxel which is smaller than a predefined radius R. Each of these tensors is then weighted according to an inverse square (Shepard) weighting function:

$$w(d_j; R) = \left(\frac{1}{d_j} - \frac{1}{R}\right)^2 \tag{5.12}$$

In our experiments R is initially chosen to be slightly smaller than the edge of a voxel but is arbitrarily increased if no displaced tensors are found. The interpolated tensor is computed via Log-Euclidean interpolation (Arsigny et al.

[2006]):

$$D(x_o) = \exp\left(\frac{\sum_j w(d_j; R)\log(D_j)}{\sum_j w(d_j; R)}\right) \tag{5.13}$$

where exp and log indicate the matrix exponential and logarithm, respectively. Finally, if the tumor cell density $c(x_o)$ at the voxel x_o is positive, we additionally interpolate $D(x_o)$ with an isotropic tensor which models the diffusivity inside the tumor. Based on measurements on patient data, we set the eigenvalues of the isotropic tensor equal to 0.001 mm^2/s. For the interpolation, the isotropic tensor is weighted by $c(x_o)$ whereas $D(x_o)$ is weighted by $1 - c(x_o)$.

5.3.3 Summary of the Tumor Growth Algorithm

In this section, we briefly summarize how we solve the PDEs which simultaneously describe the tumor invasion in the brain parenchyma and its mechanical deformation.

{**Algorithm Start**}
Initialize c according to Eq. 5.1
for $i = 1$: fixed number of iterations **do**
  Update c according to Eq. 5.2
  repeat
    Update u according to Eq. 5.6 via an explicit gradient descent algorithm
  until $\|u^{k+1} - u^k\| < \varepsilon$
  Apply the displacement field to the tensor data and reorient according to Eq. 5.9
  Interpolate the tensor data on the image grid according to Eq. 5.13
  Interpolate with an isotropic tensor in voxels where c is positive
end for
{**Algorithm End**}

To reduce numerical errors we may also keep track of the displacement fields computed for each c^i and apply their sum to the original tensor data instead of iteratively applying them to the tensor field.

5.3.4 Uncertainty Visualization by Color-Coding Streamlines

In order to visualize how tumor growth affects the parameter sensitivity of streamline tractography we start by simulating the growth of a tumor in proximity of the corticospinal tract based on the DTI data of a healthy subject. At each time-point we track the corticospinal tract using a seed region of interest (ROI) within the internal capsule and the modified DTI data. Additional ROIs are used to exclude clearly false-positive streamlines. Details about the employed deterministic fiber tracking algorithm can be found in Barbieri et al. [2011b]. We employ the visualization approach suggested by Brecheisen et al. [2009] who allow the streamline tracing to proceed in an uninhibited manner (without thresholds) and then map the anisotropy threshold profile onto the tracked streamlines. The mapping enforces the monotonicity of the values stored along the streamlines, a schematic representation of the process is presented in Fig. 5.2.

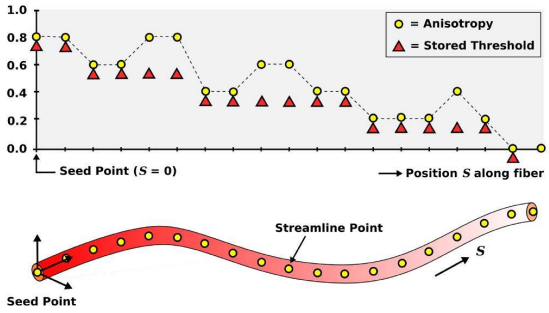

Figure 5.2: Example of anisotropy threshold profile mapped onto a streamline. Yellow dots represent the FA values of tensors pierced by the streamline while orange triangles represent the anisotropy threshold stored for each fiber point. The threshold value is always monotonically decreasing when moving away from the seed point. (*Source: Brecheisen et al. [2009]*).

In an analogous manner we map the 95% confidence intervals ("uncertainty cones") in which the main diffusion directions lie (Jones [2003]) onto the tracked streamlines. Let us briefly summarize the bootstrap method used to compute these confidence intervals. The required data consists of multiple acquisitions of diffusion weighted data with constant gradients and sequence parameters. At each voxel a large number (e.g. 1000) of bootstrap estimates of the main diffusion

direction ε_1^j are computed based on diffusion tensors fitted to diffusion weighted data coming from randomly chosen acquisitions for each gradient direction. A mean dyadic tensor $\langle \varepsilon_1^j \varepsilon_1^{jT} \rangle$ is computed as

$$\langle \varepsilon_1^j \varepsilon_1^{jT} \rangle = \left\langle \begin{pmatrix} (\varepsilon_{1x}^j)^2 & \varepsilon_{1x}^j \varepsilon_{1y}^j & \varepsilon_{1x}^j \varepsilon_{1z}^j \\ \varepsilon_{1x}^j \varepsilon_{1y}^j & (\varepsilon_{1y}^j)^2 & \varepsilon_{1y}^j \varepsilon_{1z}^j \\ \varepsilon_{1x}^j \varepsilon_{1z}^j & \varepsilon_{1y}^j \varepsilon_{1z}^j & (\varepsilon_{1z}^j)^2 \end{pmatrix} \right\rangle = \frac{1}{1000} \sum_{j=1}^{1000} \varepsilon_1^j \varepsilon_1^{jT} \tag{5.14}$$

where ε_{1i}^j is the i^{th} component of the j^{th} bootstrap estimate of the principal eigenvector. Next we compute the minimum angle subtended between each bootstrap estimate ε_1^j and the principal eigenvector $\bar{\Psi}_1$ of the average dyad $\langle \varepsilon_1^j \varepsilon_1^{jT} \rangle$:

$$\theta^j = \arccos(\varepsilon_1^j \cdot \bar{\Psi}_1) \ . \tag{5.15}$$

Since the angles are always positive their distribution is "one-tailed" and the 95% confidence interval can be computed by sorting the angles in ascending order and taking the value at the 950th position.

As a third visualization option we directly map (without enforcing monotonicity) the quantity

$$m(x) + \hat{\mu} \cdot f_{\text{CONNECTIVITY}}(x) + \hat{\omega} \cdot f_{\text{CLUSTERING}}(x) \tag{5.16}$$

onto the tracked streamlines. This quantity has been employed to accurately extract fiber bundles from DTI data in Barbieri et al. [2011b]. In brief $m(x)$ is a connectivity map, $f_{\text{CONNECTIVITY}}(x)$ and $f_{\text{CLUSTERING}}(x)$ correspond to confidence measures about the tensor at voxel x belonging to the tract of interest, based on the connectivity map and on a tensor clustering approach, respectively. We set the weights $\hat{\mu} = 0.3$ and $\hat{\omega} = 1$ as these values led to the best results in previous experiments.

5.3.5 Confidence Hulls

In order to determine a confidence hull around a reconstructed fiber bundle, we assume that the traced streamlines underestimate the true spatial extent of the

bundle. Further, we assume that the tensors within the fiber bundle (and the ones outside of it) are locally similar to one another. Therefore, if we consider a tensor A_1 pierced by a streamline and move towards the border of the fiber bundle it belongs to, generally we will first encounter one or more tensors $\{A_{2_i}\}_{i=1,\dots,N}$ belonging to the same bundle, followed by a partial volume tensor AB at the border of the bundle, and finally one or more tensors $\{B_i\}_{i=1,\dots,M}$ belonging to the neighboring bundle. For simplicity, we shall consider four representative tensors A_1, A_2, AB, and B. Given an appropriate distance d between tensors (as for example the Frobenius norm or the Log-Euclidean distance, see Arsigny et al. [2006]) we simulate 10^7 random tensor populations $\hat{A}$ and $\hat{B}$, with $A_1, A_2 \in \hat{A}$ and $B \in \hat{B}$. We then determine a threshold value over the tensor distances to A_1 which should be used to establish the correct size of the fiber bundle. More in detail, we set

- random eigenvectors and eigenvalues for tensor population $\hat{A}$ and for tensor population $\hat{B}$. The eigenvectors are uniformly distributed over the unit sphere while the eigenvalues are uniformly distributed over the interval $(0, 1)$. Successively, the eigenvalues of each population are normalized so that the largest eigenvalue is 1. This step is used to limit the possible differences between tensors. However, in our opinion, this does not particularly restrict the generality of our results, as the mean diffusivity of grey matter tensors is mostly uniform and large differences in mean diffusivity caused by tumor infiltration can be easily detected in a FA weighted map.

- a random fraction p of population $\hat{A}$ contributing to the partial volume tensor AB. p is uniformly distributed over the interval $(0, 1)$ and population $\hat{B}$ contributes $1 - p$ to the tensor.

- random noise corrupting the diffusion weighted signals used to fit the tensors, as described in Section 2.3.1.

We compute the tensor distances from A_1, A_2, AB, and B to A_1 and interpolate them via cubic Hermite splines. The threshold parameter is given by the value of the interpolated distance function at the fraction p of the spatial distance between tensors A_2 and AB. A schematic illustration of this process is given in Fig. 5.3.

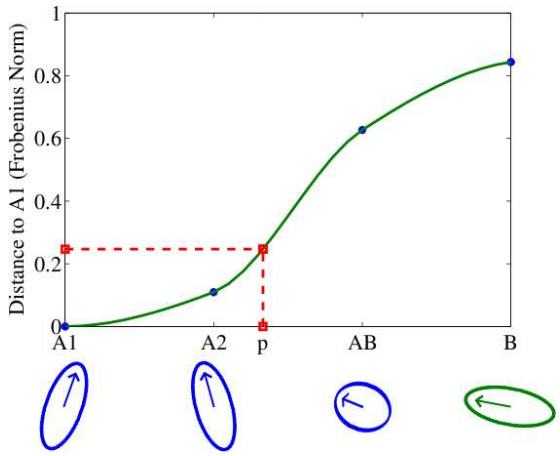

Figure 5.3: Example of tensor distances computed from tensors A_1, A_2, AB, and B to A_1 (blue dots). The interpolated distance function is displayed in green. Its value at the fraction p of the spatial distance between tensors A_2 and AB gives the threshold parameter used to determine the spatial extent of the fiber bundle (in this case it is equal to approximately 0.25).

Since a threshold parameter is computed for each pair of random tensor populations, we may approximate the distribution of all threshold parameters. Next, we determine the 33% and 66% quantiles of this distribution. The quantiles are computed for noise standard deviations varying between 0 and 10 with increments of 0.5 and for 6, 12, 15, 24, and 30 image gradients (these are the number of gradients currently used in the clinical setting).

Given the number of gradients used to acquire a diffusion weighted image and the standard deviation of the noise corrupting the image, the computed quantiles may be used to determine 33% and 66% confidence hulls around a tracked fiber bundle. To do this, we consider the image voxels pierced by tracked fibers and compute the minimum tensor distance of neighboring voxels to them. We then compute the Euclidean distance transform (EDT) to the pierced voxels and enforce that along its gradient (moving away from the fibers) the computed tensor distances are monotonically increasing. Finally the confidence hulls may be determined by using the computed quantiles as threshold parameters over the map of tensor distances.

5.4 Results

As discussed previously, we simulate an infiltrating tumor near the corticospinal tract of a healthy subject at the level of the corona radiata. The parameters of the DTI acquisition sequence are as follows: resolution = $1.80 \times 1.80 \times 1.98$ mm^3, b value = 1000 s/mm^2, NEX = 2, TR/TE = 12000/84 ms, two repetitions with one b=0 image and 30 gradient directions each. Fig. 5.4 displays the GBM volume between 0 and 10 iterations of the tumor-growth simulation algorithm.

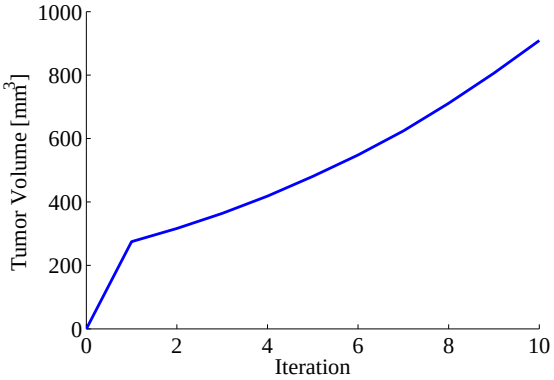

Figure 5.4: The volume of the GBM vs. the number of iterations of the tumor-growth simulation algorithm.

Figs. 5.5(a)-5.5(f) show details of the tensor fields in proximity of the simulated tumor after 0,1,3,5,7, and 9 iterations.

Figs. 5.6(a)-5.6(f) show the corresponding tracking results color-coded according to the FA threshold profiles. Fig. 5.7 shows a color-coding of the streamlines according to the 95% confidence intervals of the main diffusion directions. As an additional alternative in Fig. 5.8 we present a volume rendering of the confidence measure computed according to Eq. 5.16 and a corresponding color-coding of the traced streamlines.

Fig. 5.9 shows distributions of threshold values used to compute confidence hulls around tracked fibers, using the Frobenius norm as tensor distance and 30 gradient directions and noise standard deviation values between 0 and 10 as parameters. Corresponding plots of the 33% and 66% quantiles versus the noise standard deviation values are presented in Fig. 5.10(a) (using the Frobenius norm) and in Fig. 5.10(b) (using the log-Euclidean distance). We note that the

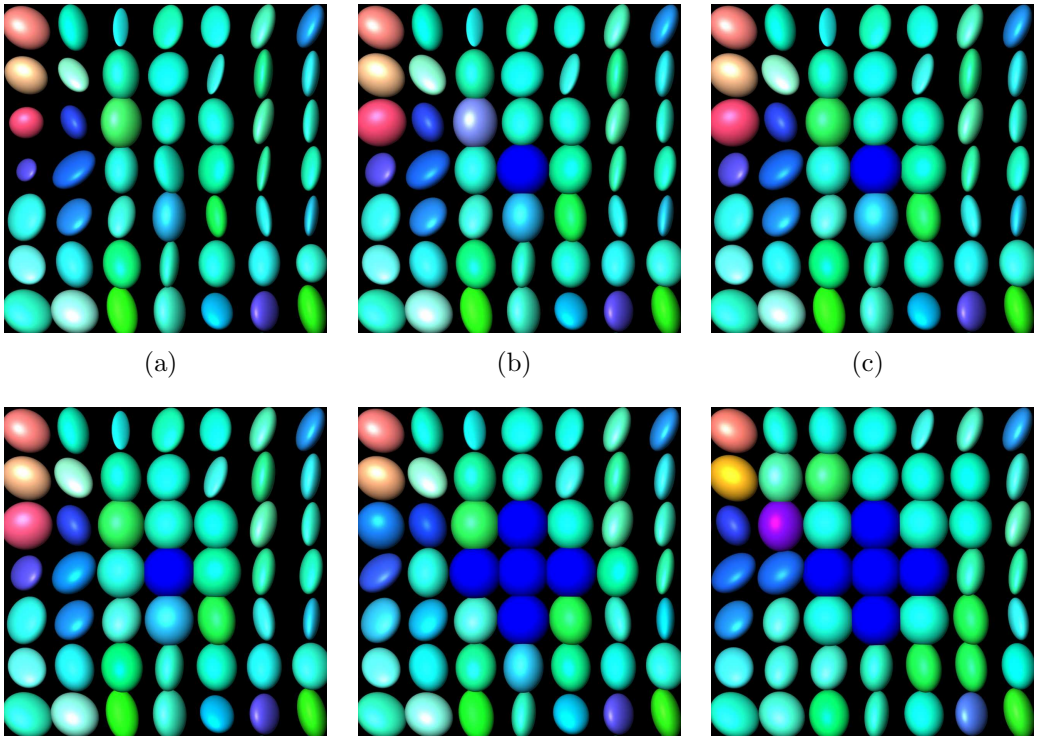

Figure 5.5: (a)-(f) show details of the tensor field in proximity of the simulated tumor after 0,1,3,5,7 and 9 iterations respectively.

relative distance between the 33% and the 66% quantiles increases much quicker in Fig. 5.10(a) than in Fig. 5.10(b). For this reason, in the following experiments we employ the Frobenius norm as the distance measure between tensors. Tables 5.1 and 5.2 (with the corresponding plots of Fig. 5.11) report the numerical values of the 33% and 66% quantiles versus the noise standard deviation values when using 6,12,15,24, or 30 gradient directions. The resulting confidence hulls computed based on the synthetic data of two crossing fiber bundles with varying image noise are presented in Fig. 5.12. In Fig. 5.13 we show the 33% and 66% confidence hulls around the corticospinal tract reconstructed based on the tumor simulation data. As mentioned above, the original diffusion weighted images were acquired using 30 gradient directions. After scaling the maximal signal intensity to 70, the noise standard deviation was determined to be approximately 3 using the double acquisition method described by Sijbers [1998]. Fig. 5.14 similarly shows the

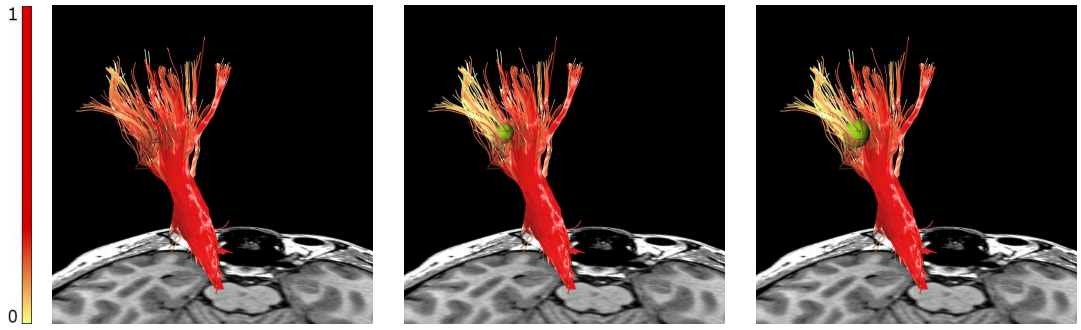

(a) (b) (c)

(d) (e) (f)

Figure 5.6: (a)-(f) FA threshold profiles mapped onto the reconstruction of the dominant part of the corticospinal tract. For the tracking we use a seed ROI located within the internal capsule. The bulk of the simulated GBM ($c > 0.2$) is shown in green. We display results after 0,1,3,5,7 and 9 iterations. A decrease in anisotropy in proximity of the tumor is noticeable as the tumor grows.

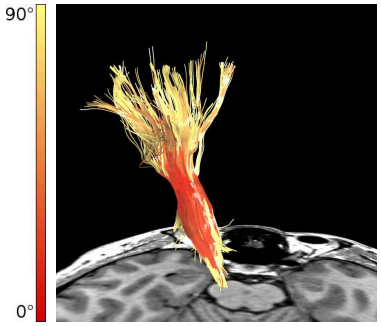

Figure 5.7: Angles corresponding to the 95% confidence intervals of the main diffusion directions ("uncertainty cones") mapped onto the reconstructed corticospinal tract.

33% and 66% confidence hulls around the corticospinal tract of a GBM patient (see Chapter 3 for details on the image acquisition sequence). In this case, the

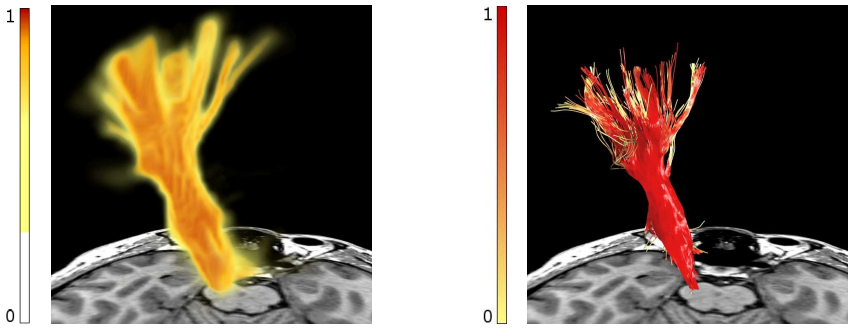

(a) (b)

Figure 5.8: The confidence measure computed according to Eq. 5.16 visualized as a volume rendering (a) and mapped onto the reconstructed corticospinal tract (b).

noise standard deviation was determined to be approximately 2.5. Because in Chapter 2 the accuracy of streamline tractography was determined to be in the order of 5 mm, in our experiments we only consider tensors with a distance of at most 10 mm from the tracked fibers.

5.5 Discussion and Conclusions

We simulated the growth of a GBM in the corona radiata starting from image data of a healthy volunteer. Compared to the approach presented by Clatz et al. [2004] we employ the subject's specific DTI data and segmentations of white and grey matter instead of registering to a common atlas, which should lead to a more accurate simulation. Moreover, we couple the PDEs that describe tumor growth and mass effect by iteratively updating the tumor invaded tensor field. Important parameters which shall be systematically varied in future work include the aggressiveness of the tumor, the specific fiber tract affected by the tumor and the position of the tumor with respect to the tract. In recent work by Hogea et al. [2007] the observation that proliferating tumor cells displace one another is integrated into the PDE that controls the evolution of the tumor cell density function c by means of an additional advection term. Although this contribution promises to increase the accuracy of simulated tumor growth, it also introduces additional parameters into the model which are possibly not easy to estimate from clinical images. Indeed an interesting aspect of tumor models which

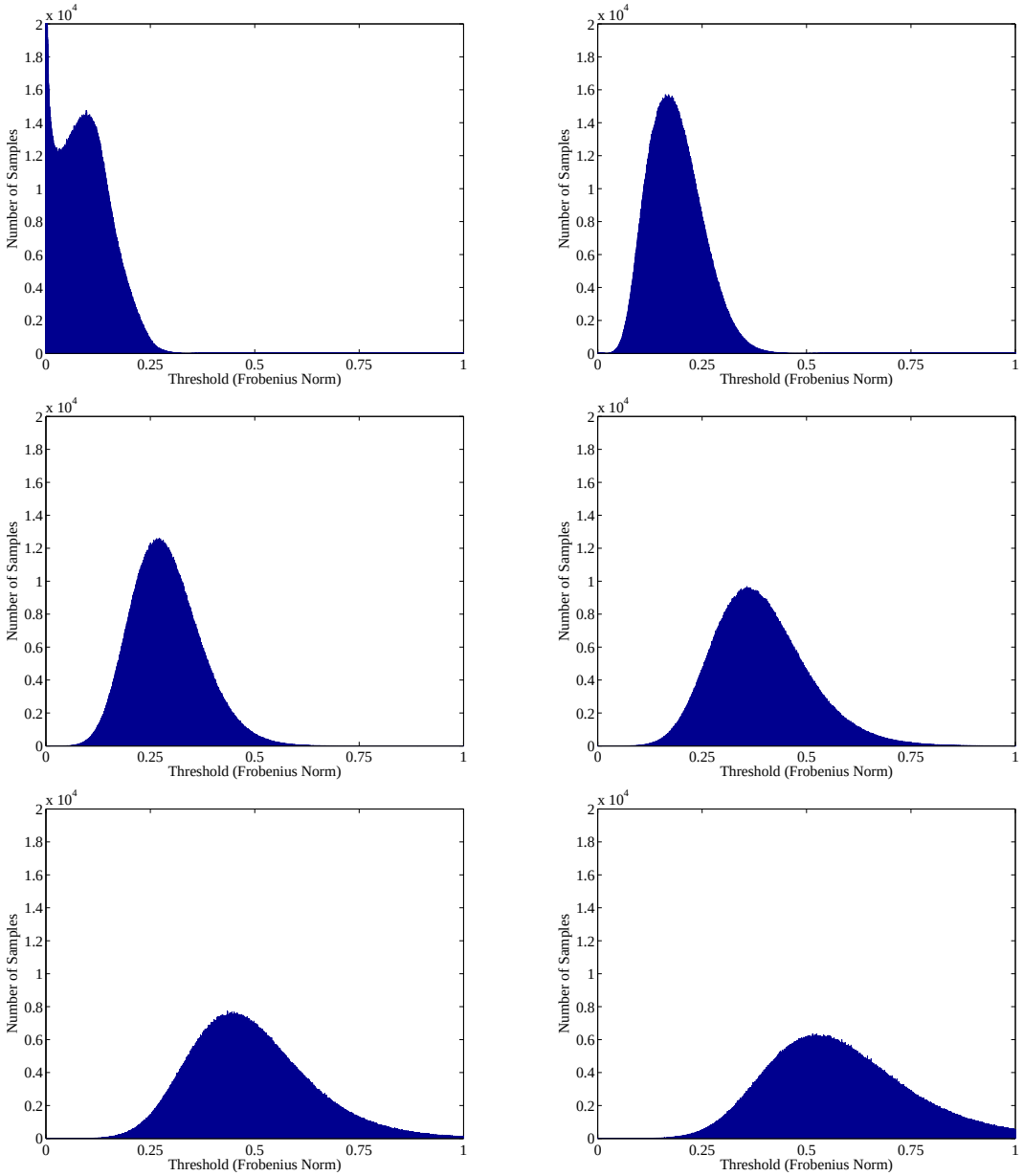

Figure 5.9: Distribution of threshold values for 30 gradient directions and noise standard deviation values of 0, 2, 4, 6, 8, and 10 (left to right, top to bottom).

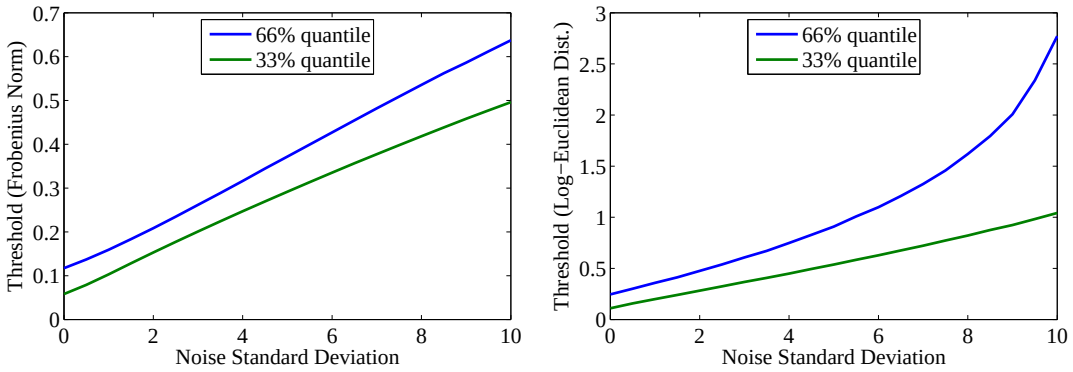

Figure 5.10: Plots of the 33% and 66% quantiles versus the noise standard deviation values when using 30 gradient directions. In (a) the Frobenius norm is used as tensor distance, while in (b) the log-Euclidean distance is used (notice that in this case the largest eigenvalue of the tensor populations was set to 0.001).

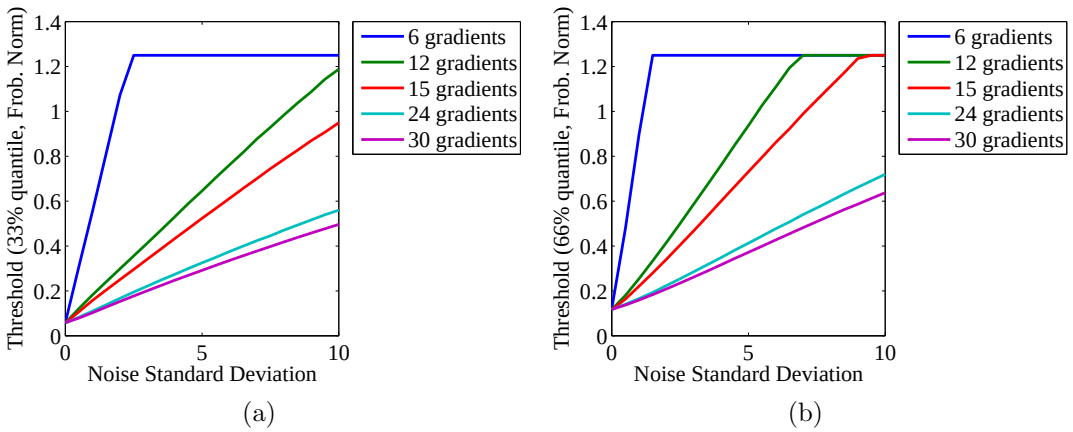

Figure 5.11: Plots of the 33% (a) and 66% (b) quantiles versus the noise standard deviation values when using 6,12,15,24, or 30 gradient directions. The maximum allowed quantile value was set to 1.25.

has not been considered in our work is how to adapt the model parameters to individual patients. The difficulty in this step arises mainly due to the sparsity of the available clinical images and because while the acquired images provide information about the contours of the tumor, tumor models generally require to estimate a tumor cell density function over the image domain. Interesting publications which attempt to address these issues include Swanson et al. [2008] and Konukoglu et al. [2010].

Noise SD	6 grad.	12 grad.	15 grad.	24 grad.	30 grad.
0.0	0.06	0.06	0.06	0.06	0.06
0.5	0.31	0.12	0.11	0.08	0.08
1.0	0.56	0.18	0.16	0.11	0.10
1.5	0.82	0.24	0.20	0.14	0.13
2.0	1.07	0.30	0.25	0.17	0.15
2.5	1.25	0.36	0.30	0.19	0.18
3.0	1.25	0.41	0.34	0.22	0.20
3.5	1.25	0.47	0.39	0.25	0.22
4.0	1.25	0.53	0.43	0.27	0.25
4.5	1.25	0.59	0.48	0.30	0.27
5.0	1.25	0.65	0.52	0.33	0.29
5.5	1.25	0.70	0.57	0.35	0.31
6.0	1.25	0.76	0.61	0.38	0.34
6.5	1.25	0.82	0.66	0.40	0.36
7.0	1.25	0.88	0.70	0.42	0.38
7.5	1.25	0.93	0.74	0.45	0.40
8.0	1.25	0.98	0.79	0.47	0.42
8.5	1.25	1.04	0.83	0.49	0.44
9.0	1.25	1.09	0.87	0.52	0.46
9.5	1.25	1.14	0.91	0.54	0.48
10.0	1.25	1.19	0.95	0.56	0.50

Table 5.1: Numerical values of the 33% quantiles versus the noise standard deviation values when using 6,12,15,24, or 30 gradient directions. The maximum allowed quantile value was set to 1.25.

We reconstruct the dominant part of the corticospinal tract via streamline tractography. Its path is adjacent to the simulated GBM and by mapping the FA threshold profiles onto the streamlines (as suggested by Brecheisen et al. [2009]) a decrease in tensor anisotropy near the tumor could be detected and visualized. This should be especially interesting for fibers going through regions of low tumor concentration which may not be considered as part of the tumor by a segmentation algorithm. For example in Fig. 5.6 the segmented tumor is given by voxels where the tumor cell concentration is above 20%, however the color-coded fibers indicate a decrease in anisotropy in a larger region. Therefore we think that the FA based color-mapping could be useful not only to explore the effect of different threshold parameters on the fiber tracking result but also

Noise SD	6 grad.	12 grad.	15 grad.	24 grad.	30 grad.
0.0	0.12	0.12	0.12	0.12	0.12
0.5	0.48	0.18	0.16	0.14	0.14
1.0	0.90	0.25	0.22	0.17	0.16
1.5	1.25	0.33	0.28	0.19	0.18
2.0	1.25	0.42	0.34	0.22	0.21
2.5	1.25	0.50	0.40	0.25	0.23
3.0	1.25	0.59	0.47	0.29	0.26
3.5	1.25	0.67	0.53	0.32	0.29
4.0	1.25	0.76	0.60	0.35	0.32
4.5	1.25	0.85	0.67	0.38	0.34
5.0	1.25	0.94	0.73	0.41	0.37
5.5	1.25	1.03	0.80	0.44	0.40
6.0	1.25	1.11	0.86	0.48	0.43
6.5	1.25	1.19	0.92	0.51	0.45
7.0	1.25	1.25	0.99	0.54	0.48
7.5	1.25	1.25	1.05	0.57	0.51
8.0	1.25	1.25	1.11	0.60	0.54
8.5	1.25	1.25	1.17	0.63	0.56
9.0	1.25	1.25	1.24	0.66	0.59
9.5	1.25	1.25	1.25	0.69	0.61
10.0	1.25	1.25	1.25	0.72	0.64

Table 5.2: Numerical values of the 66% quantiles versus the noise standard deviation values when using 6,12,15,24, or 30 gradient directions. The maximum allowed quantile value was set to 1.25.

to evaluate, when diffusion data acquired at different timepoints is available, the risk that fiber bundles of interest go through tumor-infiltrated regions.

We also propose alternative color-codings for the traced streamlines. In Fig. 5.7 the employed feature map is given by the 95% confidence intervals in which the main diffusion directions lie, computed according to the method suggested by Jones [2003]. Compared to tensor anisotropy the computed angles should represent a more informative indicator about the reliability of traced streamlines, since they account for image noise and scanner artifacts. Compared to the pointwise color-coding presented by Jones et al. [2005], enforcing the monotonicity of the values stored along the streamlines allows a prompt assessment of the uncertainty of the fiber reconstruction when moving away from the seed

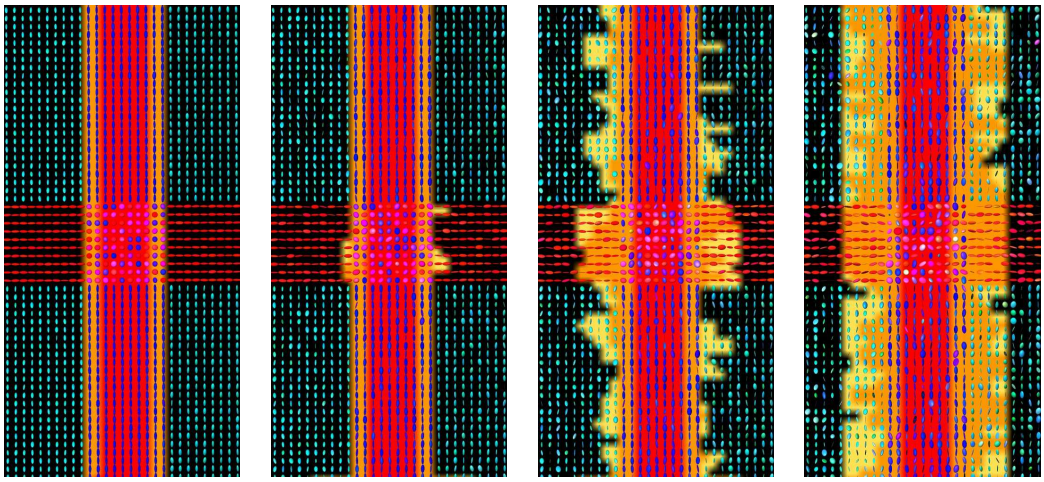

(a) (b) (c) (d)

Figure 5.12: On the simulated tensor field of two crossing fiber bundles we track the bundle running vertically. The voxels voxels pierced by the streamlines are color-coded in red, additional voxels within the 33% safety hull are color-coded in orange and additional voxels within the 66% safety hull are color-coded in yellow. The noise standard deviation value is 2.5 in (a), 5.0 in (b), 7.5 in (c), and 10.0 in (d). In this specific example, the tracked bundle lies completely within the 33% safety hull, however this is not always the case.

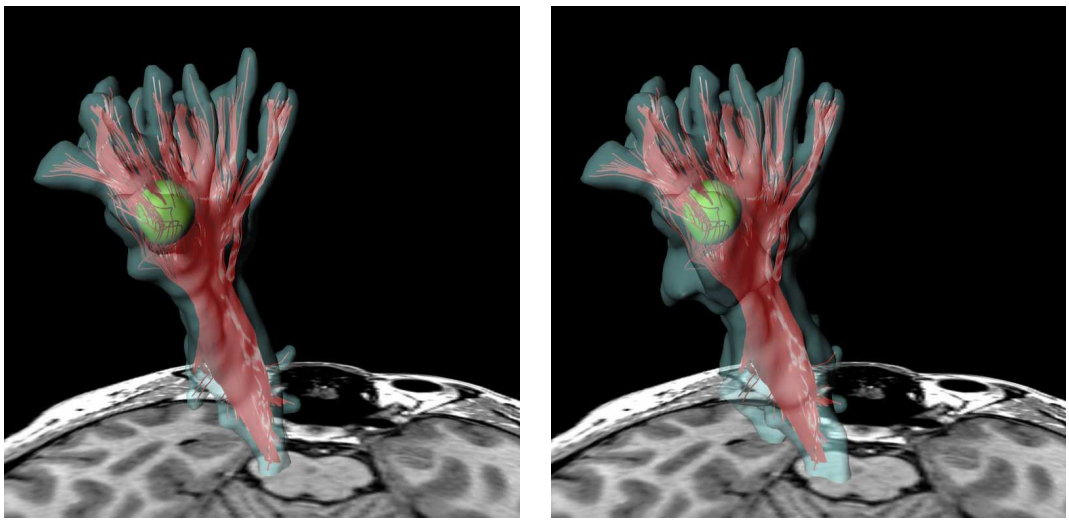

(a) (b)

Figure 5.13: Based on the diffusion tensor images with a simulated tumor we determine the 33% (a) and 66% (b) confidence hulls around the reconstructed corticospinal tract.

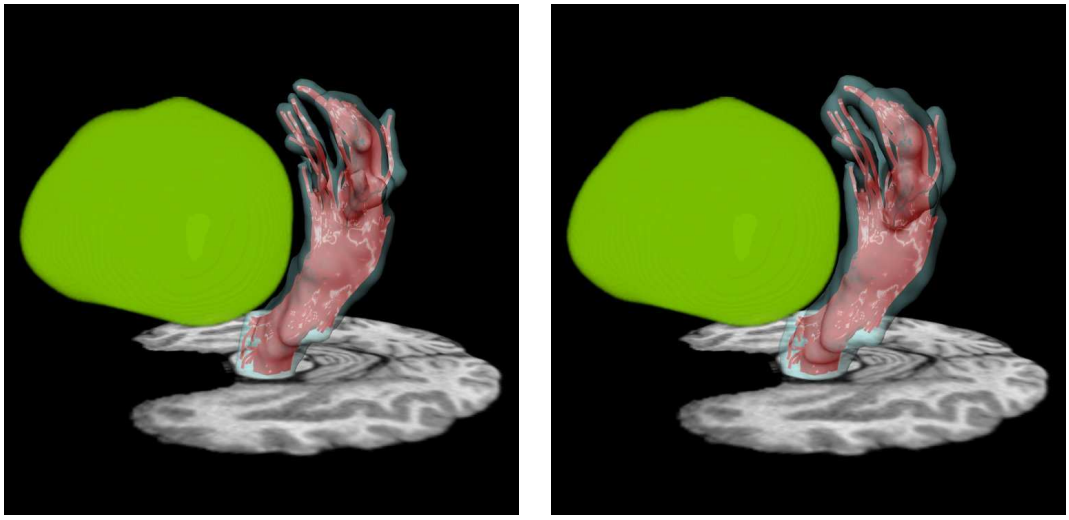

(a) (b)

Figure 5.14: We determine the 33% (a) and 66% (b) confidence hulls around the reconstructed corticospinal tract of a GBM patient. The glioma is shown in green.

ROI. In the presented example it appears as if most fibers in the corona radiata pass through voxels where the main diffusion direction is highly uncertain. A comparison with data acquired using different imaging parameters will be part of future work. In Fig. 5.8 the feature map used for the color-coding is given by a confidence measure which takes into account both connectivity measures and distances between tensors (Eq. 5.16). In our opinion this visualization approach presents valuable information about the degree of uncertainty of the traced fibers.

We suggest a method to compute patient-individual confidence hulls around a reconstructed fiber bundle. For a 33% or 66% confidence hull there is a probability of 0.33 or 0.66, respectively, that the hull does not underestimate the spatial extent of the fiber bundle of interest. Within the presented framework the size of a confidence hull is inversely proportional to the number of gradients and directly proportional to the noise standard deviation, as shown in Fig. 5.11. Future work could include the analysis of additional parameters such as b-value or image resolution. Additionally, our experiments made use of only one particular gradient scheme and it may be interesting to compare the gradient schemes used by the different MR-scanner vendors. Whereas the Frobenius norm between tensors is not expensive to compute, the employed iterative scheme used to enforce that the

computed tensor distances are monotonically increasing when moving away from the tracked fibers takes a few minutes. This cost of this step of the algorithm can likely be significantly sped up by casting rays outwards from the centerline of the fiber bundle, as described by Bauer et al. [2010b]. The experiments presented in Fig. 5.12 illustrate how the computed confidence hulls (and therefore the uncertainty about the spatial extent of the fiber bundle) get larger in regions where fibers cross. Similarly in Fig. 5.13 the computed confidence hulls get larger where corticospinal tract crosses the corpus callosum as well as in the proximity of the simulated GBM. In Fig. 5.14(b) we notice how the inferior portion of the 66% confidence hull borders the segmented GBM, while the tracked streamlines do not. This could indicate that in this area a more conservative resection is appropriate in order to avoid damage to the corticospinal tract, although a careful clinical validation is needed in order to validate such claim.

In the end, we hope that alternative color-codings of streamlines and confidence hulls may find their way into the clinical routine and offer clinicians additional clues about the uncertainty of tractography results in regions which may potentially contain fiber bundles that need to be preserved.

Chapter 6

Conclusions

We now summarize the novel ideas and main findings of this research work. For a more in-depth discussion and a comparison to related work by other authors we refer the reader to the discussion sections of the individual chapters. A section about possible future research concludes this work.

6.1 Summary

In **Chapter 2** we made use of diffusion tensor phantoms to analyze the error magnitude of streamline tractography. The first step was to define an error measure to quantify the accuracy of a fiber reconstruction result in the presence of a known ground truth. We proposed the "safety radius", an error measure which describes the distance between the border of the reconstructed bundle and the border of the modeled pathway. In our work the safety radius was employed to analyze a multitude of two-dimensional cross sections of the considered fiber bundle, however its definition may be extended to 3D by considering the three-dimensional Voronoi partition of the fiber bundle and thus allowing for a more informative measure of tracking accuracy. Based upon a phantom with a simple torus-shaped geometry, we determined that for bundles of up to 20 cm length and clinically relevant signal to noise ratios, a safety margin of 3 to 5 mm is appropriate. We found streamline tractography to be unreliable in regions where the fractional anisotropy of diffusion tensors is below 0.25, which is for example the case in regions where fibers cross. Interestingly, using a step size of approximately

the size of an edge voxel may lead to better reconstruction results compared to using much smaller step sizes. This is likely due to the fact that with a very small step size a noisy voxel along the fiber path, which presents a high error in the estimated main diffusion direction, is going to be pierced by most fibers; when a larger step size is chosen, this is not the case. We also noticed that streamlines tend to choose a few preferred paths near the center of the fiber bundle, it may therefore be interesting to enforce a minimal distance between computed streamlines.

Next, we proposed an atlas-based framework to generate diffusion tensor phantoms of neural fiber bundles. We used this framework to generate models of the corticospinal tract and of the arcuate fasciculus, with curvatures and thicknesses varying realistically along the paths of the fiber bundles, and simulated noise and partial-volume artifacts. Future work should investigate whether the framework can also be used to model branching or fanning fiber bundles such as the corona radiata or the corpus callosum, possibly by allowing the definition of multiple "centerlines" for each fiber bundle. We extended our accuracy analysis to these realistic phantoms and determined a safety margin of 4 mm to be appropriate for the corticospinal tract, while 6 mm should be used for the arcuate fasciculus due to its high curvature. We noticed a high sensitivity of our whole-brain reconstruction approach to the density of seed points and determined that placing seed points 1 mm apart offers a good trade-off between accuracy and computational cost. Future work could include repeating these experiments using more recent and accurate white matter atlases, such as the one proposed by Oishi et al. [2011]. We developed a fuzzy DTI segmentation algorithm which conveys the uncertainty about the accurate location of a fiber bundle's border to the user. The algorithm analyzes voxels in the neighborhood of tracked streamlines and takes into account both the main tensor diffusion directions and the associated covariance matrices, thus reflecting the signal to noise ratio of the image. An initial comparison with related segmentation algorithms indicates that taking into account the covariance matrices of the main diffusion directions may increase the accuracy of fiber bundle extraction.

In **Chapter 3** we further developed our ideas to increase the accuracy with which fiber bundles are extracted. We observed that probabilistic fiber-tracking

approaches are able to outline the general pathway of the bundle of interest. However, the computed connectivity values generally depend on the length and curvature of the fiber bundle, making the choice of a threshold parameter which results in a correct segmentation of the connectivity map difficult. Therefore, we proposed a combined probabilistic tractography and local tensor clustering approach, based on the notion that tensor clustering algorithms are able to exploit the local coherence between tensors of the same fiber bundle, which results in a relatively accurate border delineation. A post-processing step of the algorithm addresses voxel misclassification due to partial-volume artifacts. Our hybrid approach produces accurate results on both software phantom data (including crossing and adjacent fiber bundles) and on clinically relevant patient data. When developing this algorithm, we chose to make use of the log-Euclidean distance between tensors because it considers the full tensor information, it is invariant with respect to scaling and rotation, and it is isometric to the geodesic distance on the Riemannian manifold of symmetric positive definite matrices. However, it should be interesting to analyze the sensitivity of the results with respect to the use of different tensor distances, such as the easy to compute Frobenius norm, or the more intuitive combinations of differences in main diffusion directions and in mean diffusivities (compare Rodrigues et al. [2008], Peeters et al. [2009]). Similarly to the fuzzy region competition algorithm by Mory et al. [2007], our algorithm converges to a binary solution, however a formal proof of this property is still missing. The user interaction associated with the algorithm is comparable to the one of streamline tractography and the required computation time is less than half an hour, which should allow integration into clinical routine. Nevertheless, since the algorithm depends on two weighting parameters μ and ω, additional experiments besides the ones presented in Fig. 3.8 are needed to determine whether specific values for these parameters can be recommended for use in any scenario or if the user should compare bundle extraction results for a given set of parameters. In this case we should investigate how the segmentation result can be computed efficiently upon a change in parameters.

As mentioned earlier, the experiments in Chapter 2 confirmed that streamline fiber-tracking is very sensitive to the choice of user-defined seed ROIs. In **Chapter 4** we presented the novel idea of mapping a fiber bundle from a fiber

atlas onto the DTI dataset of a patient. This way, we are able to obtain a noise-robust, shape-consistent fiber bundle reconstruction which is not as sensitive to user-defined ROIs as streamline tractography. To implement this idea, we developed an algorithm based on a simulated annealing procedure which transforms the fiber bundle from the fiber-atlas so that it minimizes a specific energy functional. The energy functional reflects how well the fiber bundle fits the diffusion tensor data of the patient. The transformations applied to the fiber bundle consists in a concatenation of global and "local" linear transformations (translation, rotation, and scaling), which ultimately result in a non-rigid mapping. Possible ad-hoc definitions of local linear transformations of fiber bundles were presented in this chapter. We evaluated this proof-of-concept method on synthetic as well as on patient datasets, which included crossing fibers and fiber bundles considerably displaced or "cut" by lesions, and obtained promising results. However, the algorithm will need to be tested on numerous additional clinical datasets in order to determine the cases in which it is able to produce satisfying bundle reconstructions results. The quality of these results should be compared to the ones produced by recent atlas-based clustering methods, see for example O'Donnell and Westin [2007].

In **Chapter 5** we considered several alternatives to visualize fiber-tracking uncertainties by directly color-coding the computed streamlines. As a first example, we used the FA-based color-coding suggested by Brecheisen et al. [2009] to reflect the growth over time of a simulated glioblastoma multiforme. The expanding infiltrated volume leads to a decrease in tensor anisotropy, consequently to a higher error in the estimated main tensor diffusion directions and in the streamlines. In order to simulate the tumor, we developed a novel PDE-based method which models the effect of tumor growth and of the resulting tissue displacement on diffusion tensor data. Next, we color-coded the streamlines according to the angles corresponding to the 95% uncertainty cones of the main tensor diffusion directions. Because they account for image noise and scanner artifacts, the computed angles provide an interesting stopping criterion for streamline tractography which could be used instead of tensor fractional anisotropy. We also presented a color-coding based on the hybrid confidence measure introduced in Chapter 4, which combines connectivity and tensor clustering information and provides valuable

information about the uncertainty of traced fibers. As an additional alternative visualization, we determined hulls around the reconstructed fiber bundles which indicate several degrees of confidence about the hull not underestimating the true spatial extent of the bundle. The size of a "confidence hull" depends on the local similarity between tensors, on the number of gradients used to acquire the diffusion weighted images, and on the level of image noise. Thanks to the relative simplicity of the algorithm it should be possible to compute these confidence hulls based on any clinical DTI dataset, although in the future additional imaging parameters (such as b-value or resolution) may be taken into account when determining the size of the hulls.

6.2 Perspective

This thesis has focused on the processing of diffusion tensor images. The tensor model is currently the most widespread in the clinical setting, however it can describe only a single dominant fiber orientation in each voxel and is therefore known to inadequately describe the diffusion process in regions where fibers cross, kiss, fan, or merge (Alexander et al. [2002]). Tuch et al. [2002] suggested to overcome this problem by fitting multiple diffusion tensors to High Angular Resolution Diffusion Imaging (HARDI). However, this implies the ability to reliably estimate the number of fiber populations in each voxel and leads to unstable results when more than two populations are present (Tuch et al. [2002]). Additionally, HARDI acquisition protocols generally require the use of a high b-value to better discern among different fiber orientations, with the consequence of a reduced SNR and an increased challenge when modeling the data. Nonetheless, in recent years, a number of promising non-parametric models for HARDI have been suggested. They generally represent multiple fiber directions in a single voxel by means of a probability density function on the sphere, among them let us mention the *Orientation Distribution Function* (Tuch [2004], Michailovich and Yogesh [2010]), the *Fiber Orientation Density* (Tournier et al. [2004]), the *Persistent Angular Structure* (Alexander [2005]), and the *Diffusion Orientation Transform* (Ozarslan et al. [2006]). Such reconstructions may be used for fiber-

tracking (Perrin et al. [2005a], Campbell et al. [2005], Deriche and Descoteaux [2007]), or to directly segment HARDI data (Hagmann et al. [2006], Jonasson et al. [2007], Descoteaux and Deriche [2009]) and possibly obtain a more accurate spatial delineation of the fiber bundle borders. We would like to adapt the algorithms of this thesis so that they can process HARDI data. The framework proposed in Chapter 2 and later extended in Chapter 3 to generate diffusion tensor phantoms can be promptly used to generate high angular resolution diffusion images. It could be used to analyze the effect that the number of gradients, the resolution, the b-value, or the number of image acquisitions have on fiber-tracking accuracy. Particularly in regions containing multiple fiber populations the error of deterministic and probabilistic tractography on DTI data could be systematically compared to the one of fiber-tracking on HARDI data. This accuracy analysis should not be limited to software phantoms but could also include hardware phantoms of crossing fibers (see for example Bach et al. [2011]). Within Chapters 3 and 4 we presented algorithms for the segmentation of DTI and the registration of fiber bundles, in the respective concluding sections we discussed initial ideas about how these methods could be adapted to work with HARDI data. More effort will be needed to adapt the visualization techniques presented in Chapter 5, an initial step could be to color-code the reconstructed fibers based on the generalized fractional anisotropy (Tuch [2004]) of HARDI glyphs.

In its current form, the DTI segmentation algorithm from Chapter 3 employs streamline tractography to determine the likelihood of fiber bundles connecting a given region of interest to other image regions. However, particularly in regions of tumor infiltration or edema there is a decrease in tensor anisotropy, leading to unreliable streamline computations and connectivity maps. Therefore, it would be interesting to substitute streamline tracking with a global fiber-tracking technique. When reconstructing fiber bundles, global approaches achieve high robustness by taking into account the likelihood of the whole fiber path and by incorporating *a priori* anatomical knowledge. Current algorithms may be divided into graph-based and optimization-based. Graph-based approaches (Fout et al. [2005], Merhof et al. [2006]) create paths between voxels weighted according to the probability of water diffusing between them. The most likely paths that connect two user-defined regions of interest are then determined. Optimization-

based approaches (Kreher et al. [2008], Reisert et al. [2009], Reisert et al. [2010], Fillard et al. [2009]) generate, shift, rotate, and connect fiber segments in each voxel to generate fibers which minimize a specific energy functional. The energy functional describes the anatomical likelihood of the fibers and how well they fit the underlying diffusion data. If augmented with the ability of generating fibers, also the algorithm presented in Chapter 4, which maps fibers from an atlas onto the dataset of a patient, can be considered a global optimization-based approach. Global fiber-tracking could also be used to increase the robustness of the algorithm used to analyze the uncertainty around tracked fibers (see Section 2.5.2), especially in tumor infiltrated regions.

Although the presented algorithms have been successfully employed to process a few datasets of patients, we recognize the limits of our work with respect to the validation and evaluation of its clinical value. In order to address these shortcomings, in future projects we would like to acquire a large number of diffusion weighted images both of healthy volunteers as well as of patients. The MR-sequence parameters shall be systematically varied, however an artificial degradation of the image quality (for example the reduction of the number of gradients used to fit the diffusion model, or the reduction of image resolution) can be used to reduce the required scan time. The accuracy of fiber reconstructions based on the algorithms presented in this thesis could be validated via cortical or subcortical stimulation, similarly to previous studies on the accuracy of fiber-tracking carried out by Bello et al. [2008], Bozzao et al. [2010], and Maesawa et al. [2010]. To truly make our fiber reconstructions and uncertainty visualizations (see Chapter 5) available to the operating surgeon they will need to be integrated with the navigation system and the microscope in the operating room. The visualization of relevant contours and safety hulls should be adaptive, i.e. information should be displayed based upon the distance to risk structures such as blood vessels, fiber bundles, and functional areas. Finally, by comparing pre- and post-operative fiber bundle reconstructions and risk analyses with the operation outcome, it will be possible to quantify the benefit of the proposed methods to the patient.

Publications by

Sebastiano Barbieri

Barbieri, S., Bauer, M., Klein, J., Moltz, J., Nimsky, C., Hahn, H., 2012a. DTI segmentation via the combined analysis of connectivity maps and tensor distances. NeuroImage 60, 1025–1035.

Barbieri, S., Bauer, M., Klein, J., Nimsky, C., Hahn, H., 2010a. A variational, non-parametric approach to the fuzzy segmentation of diffusion tensor images, in: Proc. MICCAI 2010 Workshop on computational diffusion MRI, Beijing, China. pp. 134–145.

Barbieri, S., Bauer, M., Klein, J., Nimsky, C., Hahn, H., 2011a. Analyzing the accuracy of fiber tracking in infiltrated regions via tumor growth simulation, in: Proc. IEEE Visualization, Working with Uncertainty Workshop, Providence, Rhode Island, USA.

Barbieri, S., Bauer, M., Klein, J., Nimsky, C., Hahn, H., 2011b. Segmentation of fiber tracts based on an accuracy analysis on diffusion tensor software phantoms. NeuroImage 55, 532–544.

Barbieri, S., Klein, J., Bauer, M., Nimsky, C., Hahn, H., 2012b. Atlas-based fiber reconstruction from diffusion tensor MRI data. International Journal of Computer Assisted Radiology and Surgery (IJCARS) .

Barbieri, S., Klein, J., Nimsky, C., Hahn, H., 2010b. Assessing fiber tracking

accuracy via diffusion tensor software models, in: Proc. SPIE Medical Imaging, San Diego, California, USA. pp. 762326–1–762326–9.

Barbieri, S., Klein, J., Nimsky, C., Hahn, H., 2010c. Towards image-dependent safety hulls for fiber tracking, in: Proc. ISMRM, Stockholm, Sweden. p. 1672.

Barbieri, S., Welk, M., Weickert, J., 2008. Variational registration of tensor-valued images, in: Proc. CVPR Workshop Tensors in Image Processing and Computer Vision, pp. 1–6.

Barbieri, S., Welk, M., Weickert, J., 2009. A variational approach to the registration of tensor-valued images, in: Aja-Fernandez, S., de Luis-Garcia, R., Tao, D., Li, X. (Eds.), Tensors in Image Processing and Computer Vision. Springer, London, pp. 59–77.

Bauer, M., Barbieri, S., Klein, J., Egger, J., Kuhnt, D., Hahn, H., Freisleben, B., Nimsky, C., 2010a. Boundary estimation of fiber bundles derived from diffusion tensor images. International Journal of Computer Assisted Radiology and Surgery (IJCARS) 6, 1–11.

Bauer, M., Barbieri, S., Klein, J., Egger, J., Kuhnt, D., Hahn, H., Freisleben, B., Nimsky, C., 2010b. A ray-based approach for boundary estimation of fiber bundles derived from diffusion tensor imaging, in: Proceedings of Computer Assisted Radiology and Surgery (CARS 2010), Geneva, Switzerland.

Bauer, M., Egger, J., Barbieri, S., Klein, J., Kuhnt, D., Hahn, H., Freisleben, B., Nimsky, C., 2010c. Ray-based and graph-based methods for fiber bundle boundary estimation, in: Proceedings of the Biosignal 2010: International Biosignal Processing Conference, Berlin, Germany.

Bauer, M., Egger, J., Kuhnt, D., Barbieri, S., Freisleben, B., Nimsky, C., 2010d. Evaluation of several cost functions for min-cut-segmentation of fiber bundles in the human brain, in: 61st Annual Meeting of the German Society of Neurosurgery (DGNC) as part of the Neurowoche 2010, Mannheim, Germany.

Bauer, M., Egger, J., Kuhnt, D., Barbieri, S., Klein, J., Hahn, H., Freisleben, B., Nimsky, C., 2010e. Ein semi-automatischer graphbasierter ansatz zur

PUBLICATIONS BY SEBASTIANO BARBIERI

bestimmungen des randes von eloquenten faserverbindungen des menschlichen gehirns, in: Proceedings of the 44th DGBMT Annual Meeting, Rostock, Germany.

Bauer, M., Egger, J., O'Donnell, T., Barbieri, S., Klein, J., Freisleben, B., Hahn, H., Nimsky, C., 2010f. A fast and robust graph-based approach for boundary estimation of fiber bundles relying on fractional anisotropy maps, in: Proceedings of the 20th International Conference on Pattern Recognition (ICPR 2010), Istanbul, Turkey. pp. 4016–4019.

Beg, M., Ramana, P., Barbieri, S., Wang, L., 2012. Comparison of four shape features for detecting hippocampal shape changes in early Alzheimer's. Statistical Methods in Medical Research - Special Issue on NeuroImaging .

Klein, J., Barbieri, S., Stuke, H., Bauer, M., Egger, J., Nimsky, C., Hahn, H., 2010a. On the reliability of diffusion neuroimaging, in: Neuroimaging. Sciyo, pp. 1–24.

Klein, J., Grötsch, A., Betz, D., Barbieri, S., Friman, O., Stieltjes, B., Hildebrandt, H., Hahn, H., 2010b. Qualitative and quantitative analysis of probabilistic and deterministic fiber tracking, in: Proc. SPIE Medical Imaging, San Diego, California, USA. pp. 76232A–1–76232A–8.

Klein, J., Weiler, F., Barbieri, S., Hirsch, J., Geisler, B., Hahn, H., 2010c. NeuroQLab - an extendible software assistant for efficient and reproducible evaluation of neuroimaging data, in: Proc. European Congress on Radiology (ECR 2011), Vienna, Austria.

Klein, J., Weiler, F., Barbieri, S., Hirsch, J., Geisler, B., Hahn, H., 2010d. Novel features of NeuroQLab - a software assistant for evaluating neuroimaging data, in: Proc. European Congress on Radiology (ECR 2012), Vienna, Austria.

Moltz, J., Braunewell, S., Rühaak, J., Heckel, F., Barbieri, S., Tautz, L., Hahn, H., Peitgen, H.O., 2011. Analysis of variability in manual liver tumor delineation in CT scans, in: Proc. ISBI, Chicago, Illinois, USA. pp. 1974–1977.

References

Alexander, D., 2005. Maximum entropy spherical deconvolution for diffusion MRI. Inf. Process. Med. Imaging 19, 76–87.

Alexander, D., Barker, G., Arridge, S., 2002. Detection and modelling of non-Gaussian apparent diffusion coefficient profiles in human brain data. Magn. Res. Med. 48, 331–340.

Alexander, D., Pierpaoli, C., Basser, P., Gee, J., 2001. Spatial transformations of diffusion tensor magnetic resonance images. IEEE Trans. Med. Imaging 20, 1131–1139.

Amidror, I., 2002. Scattered data interpolation methods for electronic imaging systems: a survey. J. Elect. Imaging 11, 157–176.

Anderson, A., 2001. Theoretical analysis of the effects of noise on diffusion tensor imaging. Magn. Reson. Med. 46, 1174–1188.

Arsigny, V., Fillard, P., Pennec, X., Ayache, N., 2006. Log-Euclidean metrics for fast and simple calculus on diffusion tensors. Magn. Reson. Med. 56, 411–421.

Assaf, Y., Basser, P.J., 2005. Composite hindered and restricted model of diffusion (CHARMED) MR imaging of the human brain. Neuroimage 27, 48–58.

Assaf, Y., Freidlin, R.Z., Rohde, G.K., Basser, P.J., 2004. New modeling and experimental framework to characterize hindered and restricted water diffusion in brain white matter. Magn. Reson. Med. 52, 965–978.

Awate, S., Zhang, H., Gee, J., 2007. A fuzzy, nonparametric segmentation framework for DTI and MRI analysis: With applications to DTI-tract extraction. IEEE Trans. Med. Imaging 26, 1525–1536.

Bach, M., Stieltjes, B., Fritzsche, K., Semmler, W., Laun, F., 2011. A diffusion tensor resolution phantom, in: Proc. ISMRM, p. 6404.

Barbieri, S., Bauer, M., Klein, J., Moltz, J., Nimsky, C., Hahn, H., 2012a. DTI segmentation via the combined analysis of connectivity maps and tensor distances. NeuroImage 60, 1025–1035.

Barbieri, S., Bauer, M., Klein, J., Nimsky, C., Hahn, H., 2011a. Analyzing the accuracy of fiber tracking in infiltrated regions via tumor growth simulation, in: Proc. IEEE Visualization, Working with Uncertainty Workshop.

Barbieri, S., Bauer, M., Klein, J., Nimsky, C., Hahn, H., 2011b. Segmentation of fiber tracts based on an accuracy analysis on diffusion tensor software phantoms. NeuroImage 55, 532–544.

Barbieri, S., Klein, J., Bauer, M., Nimsky, C., Hahn, H., 2012b. Atlas-based fiber reconstruction from diffusion tensor MRI data. International Journal of Computer Assisted Radiology and Surgery (IJCARS) .

Barbieri, S., Welk, M., Weickert, J., 2009. A variational approach to the registration of tensor-valued images. Springer, London.

Basser, P., 1997. Quantifying errors in fiber-tract direction and diffusion tensor field maps resulting from MR noise, in: Proc. Int. Soc. Magn. Reson. Med.

Basser, P., 1998. Fiber-tractography via diffusion tensor MRI (DT-MRI), in: Proc. Int. Soc. Magn. Reson. Med.

Basser, P., Le Bihan, D., 1992. Fiber orientation mapping in an isotropic medium with NMR diffusion spectroscopy, in: Proc. ISMRM, p. 1221.

Basser, P., Mattiello, J., LeBihan, D., 1994a. Estimation of the effective self-diffusion tensor from the NMR spin echo. J. Magn. Reson. 103, 247–254.

Basser, P., Mattiello, J., LeBihan, D., 1994b. MR diffusion tensor spectroscopy and imaging. Biophys. J. 66, 259–267.

Basser, P., Pajevic, S., Pierpaoli, C., Duda, J., Aldroubi, A., 2000. In vivo fiber tractography using DT-MRI data. Magn. Reson. Med. 4, 625–632.

Bauer, M., Egger, J., O'Donnell, T., Freisleben, B., Barbieri, S., Klein, J., Hahn, H., Nimsky, C., 2010a. A fast and robust graph-based approach for boundary estimation of fiber bundles relying on fractional anisotropy maps, in: Proc. ICPR, pp. 4016–4019.

Bauer, M.H.A., Barbieri, S., Klein, J., Egger, J., Kuhnt, D., Hahn, H., Freisleben, B., Nimsky, C., 2010b. Boundary estimation of fiber bundles derived from diffusion tensor images. International Journal of Computer Assisted Radiology and Surgery (IJCARS) 6, 1–11.

Behrens, T., Jbabdi, S., 2009. Diffusion MRI. Academic Press, London, U.K.

Behrens, T., Woolrich, M., Jenkinson, M., Johansen-Berg, H., Nunes, R., Clare, S., Matthews, P., Brady, J., Smith, S., 2003. Characterization and propagation of uncertainty in diffusion-weighted MR images. Magn. Reson. Med. 50, 1077–1088.

Bello, L., Gambini, A., Castellano, A., Carrabba, G., Acerbi, F., Fava, E., Giussani, C., Cadioli, M., Blasi, V., Casarotti, A., Papagno, C., Gupta, A., Gaini, S., Scotti, G., Falini, A., 2008. Motor and language DTI fiber tracking combined with intraoperative subcortical mapping for surgical removal of gliomas. NeuroImage 39, 369–382.

Bezdek, J., 1981. Pattern Recognition with Fuzzy Objective Function Algorithms. Springer, Berlin, Germany.

Bhagat, Y.A., Beaulieu, C., 2004. Diffusion anisotropy in subcortical white matter and cortical gray matter: Changes with aging and the role of CSF-suppression. Magn. Reson. Imaging 20, 216–227.

Bozzao, A., Romano, A., Angelini, A., D'Andrea, G., Calabria, L., Coppola, V., Mastronardi, L., Fantozzi, L., Ferrante, L., 2010. Identification of the pyramidal tract by neuronavigation based on intraoperative magnetic resonance tractography: correlation with subcortical stimulation. Eur. Radiol. 20, 2475–2481.

BrainWeb, 2011. Project URL: `http://www.bic.mni.mcgill.ca/brainweb/`.

Brecheisen, R., Vilanova Bartroli, A., Platel, B., ter Haar Romenij, B., 2009. Parameter sensitivity visualization for DTI fiber tracking, in: Proc. IEEE Visualization and Computer Gr., pp. 1441–1448.

Campbell, J., Siddiqi, K., Rymar, V., Sadikot, A., Pike, G., 2005. Flow-based fiber tracking with diffusion tensor and Q-ball data: validation and comparison to principal diffusion direction techniques. NeuroImage 27, 725–736.

Carr, H., Purcell, E., 1954. Effects of diffusion on free precession in nuclear magnetic resonance experiments. Phys. Rev. 94, 630–638.

Catani, M., ffytche, D., 2005. The rises and falls of disconnection syndromes. Brain 128, 2224–2239.

Catani, M., Howard, R., Pajevic, S., Jones, D., 2002. Virtual in vivo interactive dissection of white matter fasciculi in the human brain. Neuroimage 17, 77–94.

Chang, L.C., Koay, C., Pierpaoli, C., Basser, P., 2007. Variance of estimated DTI-derived parameters via first-order perturbation methods. Magn. Reson. Med. 57, 141–149.

Chow, Y., Geman, S., Wu, L.D., 1983. Consistent cross-validated density estimation. Ann.Stat. 11, 25–38.

Clatz, O., Bondiau, P.Y., Delingette, H., Sermesant, M., Warfield, S., Malandain, G., Ayache, N., 2004. Brain Tumor Growth and Simulation. Technical Report 5187. INRIA.

Collins, A., Zijdenbos, A., Kollokian, V., Sled, J., Kabani, N., Holmes, C., Evans, A., 1998. Design and construction of a realistic digital brain phantom. IEEE Trans. Med. Imaging 17, 463–468.

Conturo, T., Lori, N., Cull, T., Akbudak, E., Snyder, A., Shimony, J., McKinstry, R., Burton, H., Raichle, M., 1999. Tracking neuronal fiber pathways in the living human brain, in: Proc. Natl. Acad. Sci., pp. 10422–10427.

Cristini, V., Frieboes, H., Li, X., Lowengrub, J., Macklin, P., Sanga, S., Wise, S., Zheng, X., 2008. Nonlinear modeling and simulation of tumor growth. Birkhauser, Boston.

Crum, W., Camara, O., Hawkes, D., 2007. Methods for inverting dense displacement fields: Evaluation in brain image registration, in: Proc. MICCAI, pp. 900–907.

Cruywagen, G., Woodward, D., Tracqui, P., Bartoo, G., Murray, J., Alvord, E., 1995. The modelling of diffusive tumors. J. Biol. Systems 3, 937–945.

Deriche, R., Descoteaux, M., 2007. Splitting tracking through crossing fibers: Multidirectional Q-ball tracking, in: Proc. ISBI, pp. 756–759.

Descoteaux, M., Deriche, R., 2009. High angular resolution diffusion MRI segmentation using region-based statistical surface evolution. J. Math. Imaging Vis. 33, 239–252.

Descoteaux, M., Deriche, R., Knoesche, T., Anwander, A., 2009. Deterministic and probabilistic tractography based on complex fiber orientation distributions. IEEE Trans. Med. Imaging 28, 269–286.

Deuflhard, P., 2004. Newton Methods for Nonlinear Problems. Affine Invariance and Adaptive Algorithms.. volume 35 of *Springer Series in Computational Mathematics*. Springer, Berlin, Germany.

Dionysiou, D., Stamatakos, G., Uzunoglu, N., Nikita, K., 2006. A computer simulation of in vivo tumor growth and response to radiotherapy: New algorithms and parametric results. Comp. in Biol. and Med. 36, 448–464.

Fick, A., 1855a. Concerns diffusion and concentration gradient. Ann. Phys. Lpz. 170, 59.

Fick, A., 1855b. Über diffusion. Ann. Phys. 94, 59.

Fieremans, E., De Deene, Y., Delputte, S., Ozdemir, M., D'Asseler, Y., Vlassenbroeck, J., Deblaere, K., Achten, E., Lemahieu, I., 2008. Simulation and experimental verification of the diffusion in an anisotropic fiber phantom. J. Magn. Reson. 190, 189–199.

Fillard, P., Descoteaux, M., Goh, A., Gouttard, S., Jeurissen, B., Malcolm, J., Ramirez-Manzanares, A., Reisert, M., Sakaie, K., Tensaouti, F., Yo, T., Mangin, J.F., Poupon, C., 2011. Quantitative evaluation of 10 tractography algorithms on a realistic diffusion MR phantom. Neuroimage 56, 220–234.

Fillard, P., Poupon, C., Mangin, J.F., 2009. A novel global tractography algorithm based on an adaptive spin glass model, in: Proc. MICCAI, pp. 927–934.

Fout, N., Huang, J., Ding, Z., 2005. Visualization of neuronal fiber connections from DT-MRI with global optimization, in: Proc. ACM symposium on Applied computing, pp. 1200–1206.

Francis, J., 1961. The QR transformation, I. The Computer J. 4, 265–271.

Francis, J., 1962. The QR transformation, II. The Comput. J. 4, 332–345.

Friman, O., Farneback, G., Westin, C.F., 2006. A Bayesian approach for stochastic white matter tractography. IEEE Trans. Med. Imaging 25, 965–978.

Gössl, C., Fahrmeir, L., Pütz, B., Auer, L., Auer, D., 2002. Fiber tracking from DTI using linear state space models: Detectability of the pyramidal tract. Neuroimage 16, 378–388.

Gudbjartsson, H., Patz, S., 1995. The Rician distribution of noisy MRI data. Magn. Reson. Med. 34, 910–914.

Von dem Hagen, E., Henkelman, R., 2002. Orientational diffusion reflects fiber structure within a voxel. Magn. Reson. Med. 48, 454–459.

Hagmann, P., Jonasson, L., Deffieux, T., Meuli, R., Thiran, J.P., Wedeen, V., 2006. Fibertract segmentation in position orientation space from high angular resolution diffusion MRI. NeuroImage 32, 665–675.

Hahn, E., 1950. Spin echoes. Phys. Rev. 80, 580–594.

Hahn, H., Klein, J., Nimsky, C., Rexilius, J., Peitgen, H.O., 2006. Uncertainty in diffusion tensor based fibre tracking. Acta Neurochir. Suppl. 98, 33–41.

Han, Y., Park, H., 2004. Automatic registration of brain magnetic resonance images based on Talairach reference system. Magn. Reson. Imaging 20, 572–580.

Hattingen, E., Rathert, J., Jurcoane, A., Weidauer, S., Szelényi, A., Ogrezeanu, G., Seifert, V., Zanella, F., Gasser, T., 2009. A standardised evaluation of pre-surgical imaging of the corticospinal tract: where to place the seed ROI? Neurosurg. Rev. 32, 445–456.

Henkelman, R., Stanisz, G., Kim, J., Bronskill, M., 1994. Anisotropy of NMR properties of tissues. Magn. Reson. Med. 32, 592–601.

Hext, G., 1963. The estimation of second-order tensors, with related tests and designs. Biometrika 50, 353–357.

Hogea, C., Davatzikos, C., Biros, G., 2007. Modeling glioma growth and mass effect in 3D MR images of the brain, in: Proc. MICCAI, pp. 642–650.

Holmes, C., Hoge, R., Collins, D., Woods, R., Toga, A., Evans, A., 1998. Enhancement of MR images using registration for signal averaging. J. Comput. Assist. Tomogr. 22, 324–333.

Huang, H., Zhang, J., van Zijl, P.C., Mori, S., 2004. Analysis of noise effects on DTI-based tractography using the brute-force and multi-ROI approach. Magn. Reson. Med. 52, 559–565.

ICBM DTI-81 Atlas, 2010. Project URL: `http://www.loni.ucla.edu/ICBM/Downloads/Downloads_DTI-81.shtml`.

IEEE Visualization Contest 2010, 2010. Image Data, Case 1: `http://viscontest.sdsc.edu/2010/`.

Iturria-Medina, Y., Sotero, R., Canales-Rodríguez, E., Alemán-G´omez, Y., Melie-García, L., 2008. Studying the human brain anatomical network via diffusion MRI and graph theory. Neuroimage 40, 1064–1076.

Jackowsky, M., Kao, C., Qiu, M., Constable, R., Staib, L., 2005. White matter tractography by anisotropic wavefront evolution and diffusion tensors imaging. Med. Image Anal. 9, 427–440.

Jbabdi, S., Bellec, P., Toro, R., Daunizeau, J., Pélégrini-Issac, M., Benali, H., 2008. Accurate anisotropic fast marching for diffusion-based geodesic tractography. Int. J. Biomed. Imaging 2008, 2:1–2:12.

Jbabdi, S., Woolrich, M., Andersson, J., Behrens, T., 2007. A Bayesian framework for global tractography. Neuroimage 37, 116–129.

Jezzard, P., Balaban, R., 1995. Correction for geometric distortion in echo planar images from B0 field variations. Magn. Reson. Med. 34, 65–73.

Jiao, F., Phillips, J., Stinstra, J., Krüger, J., Varma, R., Hsu, E., Korenberg, J., Johnson, C., 2010. Metrics for uncertainty analysis and visualization of diffusion tensor images. Lecture Notes in Computer Science 6326, 179–190.

Johansen-Berg, H., Behrens, T., 2009. Diffusion MRI. Academic Press, London, U.K.

Jonasson, L., Bresson, X., Thiran, J.P., Wedeen, V., Hagmann, P., 2007. Representing diffusion MRI in 5-D simplifies regularization and segmentation of white matter tracts. IEEE Trans. Med. Imaging 26, 1547–1554.

Jones, D., 2003. Determining and visualizing uncertainty in estimates of fiber orientation from diffusion tensor MRI. Magn. Reson. Med. 49, 7–12.

Jones, D., Basser, P., 2004. Squashing peanuts and smashing pumpkins: how noise distorts diffusion-weighted MR data. Magn. Reson. Med. 52, 979–993.

Jones, D., Cercignani, M., 2010. Twenty-five pitfalls in the analysis of diffusion MRI data. NMR Biomed. 23, 803–820.

Jones, D., Travis, A., Eden, G., Pierpaoli, C., Basser, P., 2005. PASTA: Pointwise assessment of streamline tractography attributes. Magn. Reson. Med. 53, 1462–1467.

Kansal, A., Torquato, S., Chiocca, E., T.S., D., 2000a. Emergence of a subpopulation in a computational model of tumor growth. J. Theor. Biol. 207, 431–441.

Kansal, A., Torquato, S., Harsh, G., Chiocca, E., T.S., D., 2000b. Cellular automaton of idealized brain tumor growth dynamics. Biosyst. 55, 119–127.

Kansal, A., Torquato, S., Harsh, G., Chiocca, E., T.S., D., 2000c. Simulated brain tumor growth dynamics using a three-dimensional cellular automaton. J. Theor. Biol. 203, 367–382.

Kantor, G., Loiseau, H., Vital, A., Mazeron, J., 2001. Gross tumor volume (GTV) and clinical target volume (CTV) in adult gliomas. Cancer Radiother. 5, 571–580.

Keles, G., Chang, E., Lamborn, K., Tihan, T., Chang, C.J., Chang, S., Berger, M., 2006. Volumetric extent of resection and residual contrast enhancement on initial surgery as predictors of outcome in adult patients with hemispheric anaplastic astrocytoma. J. Neurosurg. 105, 34–40.

Kinoshita, M., Yamada, K., Hashimoto, N., Kato, A., Izumoto, S., Baba, T., Maruno, M., Nishimura, T., Yoshimine, T., 2005. Fiber tracking does not accurately estimate size of fiber bundles in pathological conditions: Initial neurosurgical experience using neuronavigation and subcortical white matter stimulation. Neuroimage 25, 424–429.

Kirkpatrick, S., Gelatt, C.D., Vecchi, M.P., 1983. Optimization by simulated annealing. Science 220, 671–680.

Klein, J., Grötsch, A., Betz, D., Barbieri, S., Friman, O., Stieltjes, B., Hildebrandt, H., Hahn, H., 2010a. Qualitative and quantitative analysis of probabilistic and deterministic fiber tracking, in: Proc. SPIE Med. Imaging, pp. 76232A–1–76232A–8.

Klein, J., Köhler, B., Hahn, H., 2012. Efficient global fiber tracking on multidimensional diffusion direction maps, in: Proc. SPIE Med. Imaging, p. 83140M.

Klein, J., Scholl, M., Koehn, A., Hahn, H., 2010b. Real-time fiber selection using the Wii remote, in: Proc. SPIE, pp. 76250N–1–76250N–8.

Koay, C., Basser, P., 2006. Analytically exact correction scheme for signal extraction from noisy magnitude MR signals. J. Magn. Reson. 179, 477–482.

Koay, C., Chang, L.C., Carew, J., Pierpaoli, C., Basser, P., 2006. A unifying theoretical and algorithmic framework for least squares methods of estimation in diffusion tensor imaging. J. Magn. Reson. 182, 115–125.

Koay, C., Chang, L.C., Pierpaoli, C., Basser, P., 2007. Error propagation framework for diffusion tensor imaging via diffusion tensor representations. IEEE Trans. Med. Imaging 26, 1017–1034.

Koay, C., Nevo, U., Chang, L.C., Pierpaoli, C., Basser, P., 2008. The elliptical cone of uncertainty and its normalized measures in diffusion tensor imaging. IEEE Trans. Med. Imaging 27, 834–846.

Konukoglu, E., Clatz, O., Menze, B., Weber, M.A., Stieltjes, B., Mandonnet, E., Delingette, H., Ayache, N., 2010. Image guided personalization of reaction-diffusion type tumor growth models using modified anisotropic eikonal equations. IEEE Trans. Med. Imaging 29, 77–95.

Kreher, B., Mader, I., Kiselev, V., 2008. Gibbs tracking: a novel approach for the reconstruction of neuronal pathways. Magn. Reson. Med. 60, 953–963.

Kublanovskaya, V., 1961. On some algorithms for the solution of the complete eigenvalue problem. USSR Comp. Math. and Math. Phys. 1, 637–657.

Lawes, I., Barrick, T., Murugam, V., Spierings, N., Evans, D., Song, M., Clark, C., 2008. Atlas-based segmentation of white matter tracts of the human brain using diffusion tensor tractography and comparison with classical dissection. Neuroimage 39, 62–79.

Leemans, A., Sijbers, J., Verhoye, M., Van der Linden, A., Van Dyck, D., 2005. Mathematical framework for simulating diffusion tensor MR neural fiber bundles. Magn. Reson. Med. 53, 944–953.

Lenglet, C., Deriche, R., Faugeras, O., 2004a. Inferring white matter geometry from diffusion tensor MRI: application to connectivity mapping, in: Proceedings ECCV, pp. 127–140.

Lenglet, C., Rousson, M., Deriche, R., 2004b. Segmentation of 3D probability density fields by surface evolution: application to diffusion MRI, in: Proc. MICCAI, pp. 18–25.

Lenglet, C., Rousson, M., Deriche, R., Faugeras, O., Lehericy, S., Ugurbil, K., 2005. A Riemannian approach to diffusion tensor image segmentation, in: Proc. IPMI, pp. 591–602.

Li, X., Cristini, V., Nie, Q., Lowengrub, J., 2007. Nonlinear three-dimensional simulation of solid tumor growth. Discrete and Continuous Dynamical Systems - Series B 7, 581–604.

Lin, C., Wedeen, V., Chen, J., Yao, C., Tseng, W., 2003. Validation of diffusion spectrum magnetic resonance imaging with manganese-enhanced rat optic tracts and ex vivo phantoms. Neuroimage 19, 482–495.

Lori, N., Akbudak, E., Shimony, J., Cull, T., Snyder, A., Guillory, R., Conturo, T., 2002. Diffusion tensor fiber tracking of human brain connectivity: acquisition methods, reliability analysis and biological results. NMR Biomed. 15, 493–515.

Luenberger, D., 1984. Linear and nonlinear programming. Addison-Wesley, Reading, MA.

Maesawa, S., Fujii, M., Nakahara, N., Watanabe, T., Wakabayashi, T., Yoshida, J., 2010. Intraoperative tractography and motor evoked potential (MEP) monitoring in surgery for gliomas around the corticospinal tract. World. Neurosurg. 74, 153–161.

Merhof, D., Enders, F., Hastreiter, P., Ganslandt, O., Fahlbusch, R., Nimsky, C., Stamminger, M., 2006. Neuronal fiber connections based on A*-pathfinding, in: Proc. SPIE Med. Imaging, pp. 582–589.

MeVisLab, 2011. MeVisLab Software: `http://www.mevislab.de`.

Michailovich, O., Yogesh, R., 2010. On approximation of orientation distributions by means of spherical ridgelets. Trans. Img. Proc. 19, 461–477.

Mori, S., Crain, B., Chacko, V., Van Zijl, P., 1999. Three-dimensional tracking of axonal projections in the brain by magnetic resonance imaging. Ann. Neurol. 45, 265–269.

Mori, S., Oishi, K., Jiang, H., Jiang, L., Li, X., Akhter, K., Hua, K., Faria, A., Mahmood, A., Woods, R., Toga, A., Pike, G., Neto, P., Evans, A., Zhang, J., Huang, H., Miller, M., van Zijl, P., Mazziotta, J., 2008. Stereotaxic white matter atlas based on diffusion tensor imaging in an ICBM template. Neuroimage 40, 570–582.

Mory, B., Ardon, R., Thiran, J.P., 2007. Variational segmentation using fuzzy region competition and local non-parametric probability density functions, in: Proc. ICCV, pp. 1–8.

Moseley, M., Cohen, Y., Kucharcyk, J., Mintorovitch, J., Asgari, H., Wendland, M., Tsuruda, J., Norman, D., 1990a. Diffusion-weighted MR imaging of anisotropic water diffusion in cat central nervous system. Radiology 176, 439–445.

Moseley, M., Cohen, Y., Mintorovitch, J., Chileuitt, L., Shimizu, H., Kucharcyk, J., Wendland, M., Weinstein, P., 1990b. Early detection of regional cerebral ischemia in cats: comparison of diffusion and T2-weighted MRI and spectroscopy. Magn. Reson. Med. 14, 330–346.

Moseley, M., Kucharcyk, J., Asgari, H., Norman, D., 1991. Anisotropy in diffusion-weighted MRI. Magn. Reson. Med. 19, 321–326.

Mukherjee, P., Berman, J., Chung, S., Hess, C., Henry, R., 2008. Diffusion tensor MR imaging and fiber tractography: Theoretic underpinnings. Am. J. of Neuroradiology 29, 632–641.

Neil, J., Shiran, S., McKinstry, R., Schefft, G., Snyder, A., Almli, C., Akbudak, E., Aronovitz, J., Miller, J., Lee, B., Conturo, T., 1998. Normal brain in human newborns: apparent diffusion coefficient and diffusion anisotropy measured by using diffusion tensor MR imaging. Radiology 209, 57–66.

O'Donnell, L., Haker, S., Westin, C.F., 2002. New approaches to estimation of white matter connectivity in diffusion tensor MRI: Elliptic PDEs and geodesics in a tensor-warped space., in: Proc. MICCAI, pp. 459–466.

O'Donnell, L., Westin, C., 2007. Automatic tractography segmentation using a high-dimensional white matter atlas. IEEE Trans. Med. Imaging 26, 1562–1575.

Oishi, K., Faria, A., Mori, S., 2011. MRI Atlas of Human White Matter. Academic Press, London, U.K.

Ozarslan, E., Shepherd, T., Vemuri, B., Blackband, S., Mareci, T., 2006. Resolution of complex tissue microarchitecture using the diffusion orientation transform (DOT). NeuroImage 31, 1086–1103.

Pajevic, S., Aldroubi, A., Basser, P., 2002. A continuous tensor field approximation of discrete DT-MRI data for extracting microstructural and architectural features of tissue. J. Magn. Reson. 154, 85–100.

Pajevic, S., Pierpaoli, C., 1999. Color schemes to represent the orientation of anisotropic tissues from diffusion tensor data: application to white matter fiber tract mapping in the human brain. Magn. Reson. Med. 43, 526–540.

Parker, D., Gullberg, G., 1990. Signal-to-noise efficiency in magnetic resonance imaging. Med. Phys. 17, 250–257.

Parker, G., Haroon, H., Wheeler-Kingshott, C., 2003. A framework for a streamline-based probabilistic index of connectivity (PICO) using a structural interpretation of MRI diffusion measurement. Magn. Reson. Imaging 18, 242–254.

Parker, G., Wheeler-Kingshott, C., Barker, G., 2002. Estimating distributed anatomical connectivity using fast marching methods and diffusion tensor imaging. IEEE Trans. Med. Imaging 21, 505–512.

Partridge, S., Mukherjee, P., Henry, R., Miller, S., Berman, J., Jin, H., Lu, Y., Glenn, O., Ferriero, D., Barkovich, A., Vigneron, D., 2004. Diffusion tensor imaging: serial quantitation of white matter tract maturity in premature newborns. Neuroimage 22, 1302–1314.

Parzen, E., 1962. On estimation of a probability density function and mode. Ann. Math. Statist. 33, 1065–1076.

Peeters, T., Rodrigues, P., Vilanova, A., Haar Romenij, B.t., 2009. Analysis of distance/similarity measures for diffusion tensor imaging. Springer, Berlin, Germany.

Pennec, X., Fillard, P., Ayache, N., 2006. A Riemannian framework for tensor computing. Int. J. Comp. Vis. 66, 41–66.

Perrin, M., Poupon, C., Cointepas, Y., Rieul, B., Golestani, N., Pallier, C., Rivire, D., Constantinesco, A., Le Bihan, D., Mangin, J.F., 2005a. Fiber tracking in Q-ball fields using regularized particle trajectories, in: Proc. IPMI, pp. 52–63.

Perrin, M., Poupon, C., Rieul, B., Leroux, P., Constantinesco, A., Mangin, J., LeBihan, D., 2005b. Validation of q-ball imaging with a diffusion fibre-crossing phantom on a clinical scanner. Phil. Trans. R. Soc. B. - Biological Sciences 360, 881–891.

Pierpaoli, C., Basser, P., 1996. Toward a quantitative assessment of diffusion anisotropy. Magn. Reson. Med. 36, 893–906.

Pierpaoli, C., Jezzard, P., Basser, P., Barnett, A., Di Chiro, G., 1996. Diffusion tensor MR imaging of the human brain. Radiology 201, 637–648.

Pope, W., Sayre, J., Perlina, A., Villablanca, J., Mischel, P., Cloughesy, T., 2005. MR imaging correlates of survival in patients with high-grade gliomas. AJNR Am. J. Neuroradiol. 26, 2466–2474.

Poupon, C., Clark, C., Frouin, V., Regis, J., Bloch, I., Le Bihan, D., Mangin, J., 2000. Regularization of diffusion-based direction maps for the tracking of brain white matter fascicles. Neuroimage 12, 184–195.

Poupon, C., Mangin, J., Clark, C., Frouin, V., Regis, J., Le Bihan, D., Bloch, I., 2001. Towards inference of human brain connectivity from MR diffusion tensor data. Med. Image Anal. 5, 1–15.

Prados, E., Lenglet, C., Wotawa, N., Deriche, R., Faugeras, O., Soatto, S., 2006. Control theory and fast marching techniques for brain connectivity mapping, in: Proceedings CVPR, pp. 1076–1083.

Price, S., Burnet, N., Donovan, T., Green, H., Pena, A., Antoun, N., Pickard, J., Carpenter, T., Gillard, J., 2003. Diffusion tensor imaging of brain tumours at 3T: A potential tool for assessing white matter tract invasion? Clin. Radiol. 58, 455–462.

Raj, A., Hess, C., Mukherjee, P., 2011. Spatial HARDI: Improved visualization of complex white matter architecture with Bayesian spatial regularization. Neuroimage 54, 396–409.

Raykar, V.C., Duraiswami, R., 2005. Very fast optimal bandwidth selection for univariate kernel density estimation. Technical Report CS-TR-4774. Department of computer science, University of Maryland, Collegepark.

Raykar, V.C., Duraiswami, R., 2006. Fast optimal bandwidth selection for kernel density estimation, in: Proc. SIAM Int. Conf. on Data Mining, pp. 524–528.

Reber, P., Wong, E., Buxton, R., Frank, L., 1998. Correction of off resonance-related distortion in echo-planar imagin using EPI-based field maps. Magn. Reson. Med. 39, 328–330.

Reisert, M., Mader, I., Anastasopoulos, C., Weigel, M., Schnell, S., Kiselev, V., 2010. Global fiber reconstruction becomes practical. Neuroimage 54, 955–962.

Reisert, M., Mader, I., Kiselev, V., 2009. Global reconstruction of neuronal fibres, in: Proc. MICCAI, Diffusion Modelling Workshop.

Rodrigues, P., Vilanova, A., Twellmann, T., Haar Romenij, B.t., 2008. Adaptive distance learning scheme for diffusion tensor imaging using kernel target alignment, in: Proc. MICCAI Workshop on Computational Diffusion MRI, pp. 148–158.

Rohr, K., 2001. Landmark-Based Image Analysis. Kluwer Academic Press, Dordrecht, The Netherlands.

Rosenblatt, M., 1956. Remarks on some nonparametric estimates of a density function. Ann. Math. Statist. 27, 832–837.

Rosenfeld, A., J., P., 1966. Sequential operations in digital picture processing. J. of the ACM 13, 471–494.

Rousson, M., Lenglet, C., Deriche, R., 2004. Level set and region based surface propagation for diffusion tensor MRI segmentation, in: Proc. ECCV Workshops CVAMIA and MMBIA, pp. 123–134.

Russ, J., 1995. Image Processing Handbook. CRC Press, Boca Raton, FL. 2 edition.

Sanai, N., Berger, M., 2008. Glioma extent of resection and its impact on patient outcome. Neurosurgery 62, 753–764; discussion 264–266.

Schlüter, M., Konrad-Verse, O., Hahn, H., Stieltjes, B., Rexilius, J., Peitgen, H.O., 2005. White matter lesion phantom for diffusion tensor data and its application to the assessment of fiber tracking, in: Proc. SPIE Med. Imaging, pp. 835–844.

Sijbers, J., 1998. Signal and noise estimation from magnetic resonance images. Ph.D. thesis. Universiteit Antwerpen.

Slaughter, W., 2002. The linearized theory of elasticity. Birkhauser, Boston.

Sotiropoulos, S., Bai, L., Morgan, P., Constantinescu, C., Tench, C., 2010. Brain tractography using Q-ball imaging and graph theory: improved connectivities through fibre crossings via a model-based approach. Neuroimage 49, 2444–2456.

Stejskal, E., Tanner, J., 1965. Spin diffusion measurements: spin echoes in the presence of a time-dependent field gradient. J. Chem. Phys. 42, 288–292.

Stieltjes, B., Kaufmann, W., Van Zijl, P., Fredericksen, K., Pearlson, G., Solaiyappan, M., Mori, S., 2001. Diffusion tensor imaging and axonal tracking in the human brainstem. Neuroimage 14, 723–735.

Swanson, K., Rostomily, R., Alvord, E., 2008. A mathematical modelling tool for predicting survival of individual patients following resection of glioblastoma: a proof of principle. British J. of Cancer 98, 113–119.

Tanner, J., Stejskal, E., 1968. Restricted self-diffusion of protons in colloidal systems by the pulsed-gradient. J. Chem. Phys. 49, 1768–1777.

Tournier, J., Calamante, F., Gadian, D., Connelly, A., 2004. Direct estimation of the fiber orientation density function from diffusion-weighted MRI data using spherical deconvolution. NeuroImage 23, 1176–1185.

Tournier, J.D., Calamante, F., King, M., Gadian, D., Connelly, A., 2002. Limitations and requirements of diffusion tensor fiber tracking: an assessment using simulations. Magn. Reson. Med. 47, 701–708.

Tracqui, P., Cruywagen, G., Woodward, D., Bartoo, G., Murray, J., Alvord, E., 1995. The modelling of diffusive tumors. J. Biol. Systems 3, 937–945.

Tuch, D., 2004. Q-ball imaging. Magn. Reson. Med. 52, 1358–1372.

Tuch, D., Reese, T., Wiegell, M., Makris, N., Belliveau, J., Weeden, V., 2002. High angular resolution diffusion imaging reveals intravoxel white matter fiber heterogeneity. Magn. Reson. Med. 48, 577–582.

Černý, V., 1985. Thermodynamical approach to the traveling salesman problem: An efficient simulation algorithm. J. Optimization Theory and Appl. 45, 41–51.

Visser, E., Nijhuis, E., Buitelaar, J., Zwiers, M., 2011. Partition-based mass clustering of tractography streamlines. Neuroimage 54, 303–312.

Wang, H., Kearney, J., Atkinson, K., 2002. Curve and Surface Design. Nashboro Press, Brentwood, TN.

Wang, X., Grimson, W., Westin, C.F., 2011. Tractography segmentation using hierarchical Dirichlet processes mixture model. Neuroimage 54, 290–302.

Wang, Z., 2004. Diffusion tensor field restoration and segmentation. Ph.D. thesis. University of Florida.

Wang, Z., Vemuri, B., 2004a. An affine invariant tensor dissimilarity measure and its application to tensor-valued image segmentation, in: Proc. CVPR, pp. 228–233.

Wang, Z., Vemuri, B., 2004b. Tensor field segmentation using region based active contour model, in: Proc. ECCV, pp. 304–315.

Weinstein, D., Kindlmann, G., Lundberg, E., 1999. Tensorlines: Advection-diffusion based propagation through diffusion tensor fields, in: Proc. IEEE VIS, pp. 249–253.

Wiegell, M., Tuch, D., Larson, H., Wedeen, V., 2003. Automatic segmentation of thalamic nuclei from diffusion tensor magnetic resonance imaging. Neuroimage 19, 391–402.

Yanasak, N., Allison, J., 2006. Use of capillaries in the construction of an MRI phantom for the assessment of diffusion tensor imaging: demonstration of performance. Magn. Reson. Imaging 24, 1349–1361.

Yushkevich, P., Zhang, H., Simon, T., Gee, J., 2008. Structure-specific statistical mapping of white matter tracts. Neuroimage 41, 448–461.

Zhang, H., Awate, S., Das, S., Woo, J., Melhem, E., Gee, J., Yushkevich, P., 2009. A tract-specific framework for white matter morphometry combining macroscopic and microscopic tract features, in: Proc. MICCAI, pp. 141–149.

Zhukov, L., Museth, K., Breen, D., Whitaker, R., Barr, A., 2003. Level set segmentation and modeling of DT-MRI human brain data. J. Elect. Imaging 12, 125–133.

Ziyan, U., Tuch, D., Westin, C.F., 2006. Segmentation of thalamic nuclei from DTI using spectral clustering, in: Proc. MICCAI, pp. 807–814.

Zou, K., Warfield, S., Bharatha, A., Tempany, C., Kaus, M., Haker, S., Wells III, W., Jolesz, F., Kikinis, R., 2004. Statistical validation of image segmentation quality based on a spatial overlap index. Acad Radiol. 11, 178–189.